TOOLS FOR DEFORMABLE IMAGE REGISTRATION

by

Anton Edis Bowden

A dissertation submitted to the faculty of
The University of Utah
in partial fulfillment of the requirements for the degree of

Doctor of Philosophy

Department of Bioengineering

The University of Utah

December 2003

ABSTRACT

Medical imaging sensors can be used to noninvasively probe tissue morphology and monitor material deformations associated with growth, disease, or normal physiology. Deformable image registration provides a framework for extracting and quantifying this information. Image registration is, however, an inherently ill-posed inverse problem. The research in this dissertation investigates techniques to regularize image registration problems. Preprocessing, integral and post-processing tools were developed to complement existing image registration techniques. These tools included techniques for dynamic (sequential) spatial filtering, histogram-matching, sequential image tracking, rezoning, and other techniques that allow the solution of difficult practical registration problems. These tools have been incorporated into the continuum mechanics based deformable template registration method known as Warping. Warping was then used to solve a variety of typical registration problems, utilizing regularization tools when needed.

Additionally, two quantitative techniques for assessing image registration results have been developed and implemented. The singular value decomposition (SVD) topology tracking technique hierarchically assesses the match in topology between image data sets. The technique also provides a systematic method of tracking the evolving topology of the deformed template data during registration and comparing it with the topology of the target image data. In order to apply the

technique to volumetric image data, a three-dimensional (3D) extension of the SVD was formulated. The technique was applied to registration problems using both simulated and real image data. Results indicated that spikes in the inner product map of the template may correspond to potential difficulties in the registration.

The second technique utilized the variances of the registration potential energy to evaluate the relative influence of image data and registration method on image registration solutions. An image influence parameter was defined, which provided a regional measure of the relative influences of the image energy and registration method over the domain of the template model. The technique was applied to several representative image registration problems. Results indicated that choice of image registration method played a significant role in registration results in image regions of conflicting or inadequate image texture.

To my beloved wife, Jennifer, who made this possible

TABLE OF CONTENTS

LIST OF FIGURES

ACKNOWLEDGMENTS

I would like to express special appreciation to my advisor, Dr. Richard Rabbitt, for his continuous support and help throughout the course of my doctoral studies. His sound advice and constructive criticism have been essential to the quality of this work, and to its completion. He provided an ideal environment for my professional development by encouraging independence in my research and responsibility for my results. I would also like to thank my co-advisor, Dr. Jeffrey Weiss, for his valuable time in explaining the intricacies of nonlinear finite element analysis. His understanding of the inner-workings of NIKE3D has been critical to the success of this work.

I am indebted to the other members of my committee, Drs. Christopher Johnson, Robert Macleod, and Alexander Veress, for their valuable time and willing participation in this endeavor. I am also deeply indebted to my external reviewer, Dr. Bradley Maker for his encouragement and tutelage. My interaction with him has inspired my development as scientist and a programmer.

Finally, I wish to thank my wife Jennifer, and my children Samuel and Emma for their patience, love, and support through the last seven years. I could not have done this without them.

CHAPTER 1

INTRODUCTION

Motivation

Since the discovery of X-Rays, medical imaging has become a vital part of biological and medical research. As techniques for acquiring images improve, so does the amount of information that can be extracted from these images. The role of medical imaging continues to evolve far beyond simple inspection and visualization of biological structures. It has become a tool for disease diagnosis and tracking, surgical planning, evaluation of organ function, and a myriad of other uses.

In some cases, the best method for examining biological structure and function is through comparison of medical images with those taken from similar structures that have been more thoroughly characterized. Often, additional insights may be obtained through comparison of images of a biological structure in deformed stress states with images of the same structure in a reference configuration.

With recent advances in image acquisition techniques, medical imaging is now in a position to offer improved insights into biomechanics. Although many physical quantities may be measured directly using modern imaging techniques, extracting stress and strain fields from medical images remains a challenge. Recently, deformable image registration methods have emerged that use medical images in

combination with computational methods to determine nonlinear deformation fields (and in some cases the corresponding strain and stress fields). These methods are compatible with modern imaging modalities (e.g., CT, MR, PET, SPECT, optical microscopy), and allow accurate estimation of in vivo strain fields, without the need for exact material properties or invasive surgery.

The overall objectives of this research are to develop a set of practical techniques for regularizing and evaluating the efficacy of image registration problems, specifically applied to the deformable image registration method referred to herein as "Warping" [1-4]. The specific aims of the research are to: 1) develop and implement a suite of practical tools for regularizing image registration, 2) develop, implement, and evaluate quantitative techniques for evaluating the success of image registration, 3) demonstrate the efficacy of aims 1 and 2 using a series of simulated and actual image registration problems.

Summary of Chapters

Chapter 2 introduces the process of image registration, with specific emphasis on the methods for deformable image registration. The ill-posed nature of the image registration problem is described and discussed. A review of the literature on image registration is presented, including current registration techniques and regularization strategies, and related fields of research are identified. The relevance of the present work to current image registration techniques is established.

Chapter 3 details the development and implementation of several regularization tools created during the course of the present research. These tools are characterized as preprocessing, processing, or postprocessing tools. Preprocessing

tools address inconsistencies in medical image data due to the stochastic nature of image acquisition devices, as well as differences in acquisition techniques that can occur in intersubject registration. Processing tools are applied during the image registration process to avoid local minima solutions. Postprocessing tools facilitate accurate visualization and evaluation of the computed registration solution. Additionally, because image registration is often an iterative process, postprocessing tools often guide variation in registration parameters during iterations, as well as providing stopping criteria.

Chapter 4 addresses the practical aspects of image registration. A brief description of the mathematical basis of Warping, as well as some details of the implementation are presented. A collection of both simulated and real example problems demonstrate application of the techniques described in Chapter 3. A combination of simulated nonlinear forward problems and image registration problems are used to validate the Warping method for computing strain and stress fields. Warping is then used to compute strain and stress fields in a human spinal disc, human distal phalanx, and a mouse tectorial membrane. Since a large portion of medical image registration problems deal with mapping various study anatomies into alignment with a template anatomy, Warping is also used to examine intersubject registration of both macaque and mouse neuroanatomies. An additional application of the method is demonstrated through semiautomatic generation of a subject-specific hexahedral mesh for the human distal femur.

A paper detailing a new topology tracking technique for evaluating the success of medical image registration is presented in Chapter 5. The technique is based on

singular value decomposition (SVD) and provides an objective method to compare the topology of a deformed template image with that of a target image. A 3D extension of the standard singular value decomposition is posed and applied. The technique provides: 1) A hierarchical method to quantify image registration, 2) a method to assess topological mismatch between image datasets, and 3) a means to rank image registration solutions to distinguish local from global minima. Results demonstrate application of the technique using magnetic resonance images of the heart and human distal phalanx, as well as optical images of primate brain cryosections. Results indicate that the technique may also be useful for a priori identification of local minima.

In Chapter 6, a novel technique for assessing the interaction of image data and registration method in deformable image registration is presented. The technique utilizes the characteristics of the Hessian of the energy functional (cost function). An image influence parameter is defined that quantitates the regional variance in the influence of the image data over the domain of the template model. A variety of practical registration problems are evaluated using the technique. The value of the technique lies in its ability to indicate the reliance of the computed solution on the image data as compared to the constraint system.

Chapter 7 provides a cohesive discussion of the work from previous chapters. The overall significance of the present work is emphasized and the strengths and limitations of the work are presented. An outline of future work stemming from the current research is also presented.

The attached appendix details the derivation of the fundamental Warping equations in indicial form. Although the warping derivation has been previously published [2-4] in direct notation, the indicial notation equations are a valuable reference for those interested in the practical aspects of coding.

References

1. A.E. Bowden, R.D. Rabbitt, J.A. Weiss, and B.N. Maker, "Anatomical registration and segmentation by warping template finite element models," *Proc. SPIE*, vol. 3254, pp. 469-476, 1998.

2. J.A. Weiss, R.D. Rabbitt, and A.E. Bowden, "Incorporation of medical image data in finite element models to track strain in soft tissues," *SPIE Biomed. Optics Symp. BiOS98*, vol. 3254, pp. 477-484, 1998.

3. R.D. Rabbitt, J.A. Weiss, G.E. Christensen, and M.I. Miller, "Mapping of hyperelastic deformable templates," *Proc. SPIE*, vol. 252, pp. 252-265, 1995.

4. A.I. Veress, J.A. Weiss, R.J. Gillies, A.E. Bowden, J.-P. Galons, and R.D. Rabbitt, "Quantification of changes in mouse brain morphology using MRI and hyperelastic warping," *IEEE Trans. Medical Imaging*, to be published.

CHAPTER 2

BACKGROUND

Biomedical image registration plays an important role in a wide variety of medical applications, including image comparison [1]-[3], image fusion [4], segmentation [5]-[10], image-guided surgery [11], and strain field computation [12]-[16]. In its simplest form, it is the process of aligning anatomical features present in a template image data set (a.k.a. reference, textbook, atlas) with those present in a specific target (subject) image data set. While the premise is simple, implementation can be challenging. The problem is ill-posed in the sense of Hadamard [17], [18] because there is not a unique solution to the registration and some form of regularization must be used to constrain the manipulation [19]. Various constraints have been used towards this goal. Image registration methods are typically classified according to the technique used to limit the field of acceptable solutions.

Registration Techniques

There are numerous techniques for achieving image registration, e.g., [20]-[23]. Recent efforts follow three distinct lines: 1) Landmark or marker based identification techniques that align key points from a template image set with those in

a target image set [24], 2) Principal axis registration methods based on low-dimensional translation, rotation, and scaling operations [5], [25], and 3) Deformable image registration methods (deformable shape models) [26].

Landmark Based Registration

The use of fiducial markers or anatomical landmarks to achieve intersubject or multimodality registration has been well established [23], [27]-[31]. Distinct anatomical landmarks (or markers) are selected on both of the image datasets that are to be aligned. A transformation map between the images is obtained by interpolation between these key landmarks, which are constrained to align perfectly.

Landmark based registrations have a low computational cost and are currently favored in clinical situations where quick answers are desired. A drawback to these techniques is that they rely heavily on expert interaction to determine appropriate anatomical points to use as landmarks, as well as to define the location of those points. Additionally, because the technique relies upon interpolation between the chosen landmark points, the quality of the registration obtained is highly dependent upon the quantity and spacing of these landmarks.

Principal Axis Registration

Principal axis registration [5], [25], [32], [33] is often used for extremely quick registration of medical images. Binary versions of the 3D image data are created using a threshold algorithm. Principal axes of these binary template and target image datasets are computed using the eigenvectors of the inertia matrix [32], [5]. Volume centroids of the binary image datasets are computed in the standard manner.

Registration is obtained by translation and rotation of the template image dataset to align centroids and principal axes. The template image volume is then scaled to complete the registration.

Principal axis registration is extremely fast compared to other image registration techniques, and may be appropriate for applications where the template and target images are taken from the same anatomy using different imaging techniques. However, the technique is often inappropriately applied to segmentation or intersubject registration problems. Considering the enormous anatomical variability present in even the normal population, failure to address fundamental differences in structure between subjects during registration makes this method inadequate for all but the most global image comparisons. Some researchers have used Principal Axis registration as a preliminary step to remove global rigid body differences [34].

Deformable Image Registration

Deformable image registration is rapidly gaining preference for many image registration applications. In deformable image registrations, a geometrical model of the template image dataset is created and subsequently deformed to align with the target. The template is typically a static set of image data. The target can either come from a time sequence of image data taken of the template anatomy during deformation, or from entirely different subjects. The first case represents a strain-tracking problem common in experimental biomechanics, e.g., ventricular mechanics [35]-[39], plaque mechanics [40]-[51], knee mechanics [48], [51]-[61], and muscle mechanics [50], [62]-[68]. The second case represents a segmentation or registration

problem frequently encountered in medical imaging, e.g., tracking tumor growth [69], [70], brain mapping [24], [71]-[73], or anatomical metric tracking [74]-[76]. One goal is common: generate a transformation map (registration) between the reference image set (the template), and the target image set. This transformation map allows direct comparison of tissue geometrical structures as represented by the image sets. Registration can also provide 3D spatio-temporal strain field information based on inhomogeneities in the deforming tissue as interrogated by the imaging sensors.

When deformable image methods are rigorously applied, the template transformation is governed by principles of nonlinear differential geometry or continuum mechanics. Some methods focus on border information, such as the deformable contour models of Kass [66], [77]-[80]. Others have used full volumetric approaches subject to the laws of linear solid mechanics [81]-[86], fluid mechanics[87]-[89], nonlinear continuum mechanics [7], [12], [13], [16], [90], [91], or free-form deformation [92], [93]. Although deformable image methods are robust enough to solve most problems without user interaction, many of these techniques also allow stipulation of known correlation points (landmarks) in both the template and target image datasets.

The advantages of deformable image registration methods are due to their ability to automatically generate very high resolution (often voxel level) transformation maps between the template and target image datasets. A primary use of such techniques to date has been medical image segmentation and registration [7]-[10], [66], [94], [95]. The methods have also been applied to a wide range of problems including handwriting recognition [96], [97], vehicle classification [98],

facial feature recognition [99], [100], fish identification [30], military target identification [101], manufacturing [102], and nonlinear strain computation [12]-[16], [47].

Deformable image registration methods typically require significantly more computational effort than landmark or principal axes methods. Additionally, stopping criteria for these methods are often ad-hoc and there is the potential for generation of incomplete registrations (local minima solutions) due to premature termination of the registration process.

A significant portion of the present work has been devoted to techniques for quantifying the success of deformable image registration techniques. Previous efforts to quantify the success of these techniques have focused on global comparisons of the mapped image following registration with the target image. Examples include image subtraction [16], misfit calculation (a.k.a. sum of the squared differences) [103], histogram comparisons [104], wavelet transform comparisons [105], and mutual information [106]. A potential drawback of global measures is that they do not show the regions of the registered image where the registration scheme is highly dependent upon the registration constraints (rather than the image data). Additionally, global measures can be inconsistent with expert observer evaluations.

Related Fields of Research

The technology underlying deformable image registration has direct application to three major fields of research: pattern recognition, biomechanics, and medical imaging. To provide context for the present work, related contributions from each field are summarized briefly below.

Pattern Recognition

Significant effort has been devoted to establishing methods for recognizing distinct patterns present in image data. Applications to the medical field are abundant. For example, a radiologist might recognize that certain intensity patterns are indicative of a tumor, while other patterns represent a benign cyst. Numerous techniques have been proposed for attempting automated or semiautomated pattern recognition, such as nearest neighbor [107], clustering [108], neural networks [109], support vector machines [110], [111], and statistical techniques [112], [113], [63].

Many of the image registration methods currently in use can trace their roots to pattern recognition techniques. Indeed, image registration can be classified as a pattern recognition technique, and the literature is often intertwined. In many cases, new algorithms that simplify the pattern recognition process can also be applied to image registration.

Biomechanics

An important problem in biomechanics is the extraction of three-dimensional (3D) strain tensor fields from biological tissues undergoing deformation. Tissue deformation described by the strain field has been used to study function of the heart [114]-[116], joint dysfunction [117], and other physiologically relevant problems [118]-[121].

Previous attempts to estimate nonlinear strains in biological tissues and cells have typically employed fiducial markers [65], [122]-[129]. 3D strains can be estimated directly from changes in the distances between groups of markers making

up tetrahedral sets. Inhomogeneous strain fields and physical dimensions of the markers, however, can limit applicability of marker-based methods [36], [122], [123]. Some techniques attempt measurement of biological strain fields using direct imaging methods such as tagged MRI [115], intravascular ultrasound [43], [46], spatial modulation of magnetization (SPAMM) MR [39], or other methods [114], [130], [131]. These techniques allow direct, in vivo measurement of strain fields. However, each of these methods makes assumptions about homogeneity of the deformation field, similar to marker-based techniques. Additionally, image resolution is generally poor and extended image acquisition times are often required.

Many researchers currently use computational techniques such as finite element analysis (FEA) for predicting the strain and stress fields developed in biological tissue during deformation [41], [61], [68], [132]-[134]. These techniques have obvious advantages over invasive experimental methods, which would otherwise be required to obtain this information. The techniques are also able to deal with a tremendous variety of complex tissue geometries and nonlinear material properties [135]. A drawback to purely computational techniques is that material property data for biological tissues are often poorly characterized. Additionally, both material properties and geometry can vary widely between subjects, making generalized models inadequate in many instances. Verification of results is also challenging.

Some of the most successful techniques to date have used a combination of computational, experimental, and imaging methods to calculate stress and strain fields in biological tissue [37], [136], [137]. Subject-specific computational models are created directly from image data that correspond to the biological structures of

interest. Material property values are then measured experimentally directly from explanted tissue. Marker-based imaging methods are used to verify the computational results as far as possible. The most obvious disadvantage of these techniques is that they must generally be performed on cadavers because of the necessity of obtaining accurate material properties and applying markers to the tissue of interest.

Medical Imaging

Part of the usefulness of medical imaging sensors stems from their ability to interrogate the 3D structure of biological tissue. The process of medical imaging generally involves a measurement process, followed by an image reconstruction process. Stochastic noise and systematic errors in these processes propagate to the reconstructed image. The statistical properties of imaging sensors can influence the ability of both intrasubject and intersubject image registrations to achieve acceptable results [7], [13], [66]. Examples of stochastic sources of error related to imaging sensors include X-ray interaction effects and attenuation effects, magnification effects, and tomographic reconstruction approximations. Systematic errors can also influence registration methods. Examples of systematic sources of error [138] include calibration errors, differences in imaging scanner settings, differences in exposure time, and differences in tomographic reconstruction techniques.

Relation to Present Work

The continuum mechanics origins of the deformable image registration (Warping) method developed by Rabbitt and Weiss [16], [90] present several advantages over other registration techniques, albeit at a computational cost. The

registration obtained is a one-to-one (diffeomorphic) mapping of differential lines, areas and volumes from the target image set to the template. Thus all features associated with the template (labels, functional information, segmentation information, etc.) are easily transferred to the target. Relative volume results are readily available, providing a means to identify subject abnormalities and/or tracking tumor growth over time. Because of these features the method was used as a test bed for implementation and evaluation of the tools developed in the present work.

References

1. A.I. Veress, J.A. Weiss, R.J. Gillies, A.E. Bowden, J.-P. Galons, and R.D. Rabbitt, "Quantification of changes in mouse brain morphology using MRI and hyperelastic warping," *IEEE Trans. Med. Imaging*, to be published.

2. A.I. Veress, J.A. Weiss, G.J. Klein, and G.T. Gullberg, "Quantification of 3D left ventricular deformation using hyperelastic warping: Comparisons between MRI and PET imaging," in *Computers in Cardiology*, Memphis, TN, 2002.

3. J.A. Weiss, A.I. Veress, A.E. Bowden, R.D. Rabbitt, R.J. Gillies, J.-P. Galons, and J. Guo, "Local measurements of changes in shape and volume between serial volumetric medical images: Application to Niemann-Pick type C disease progression," *Center for High Performance Computing News, University of Utah*, vol. 12, no. 3, pp. 1-3, 2001.

4. R.G. Aykroyd and K.V. Mardia, "An MCMC approach to wavelet warping," *Image Fusion and Shape Variability Techniques*, pp. 129-140, 1996.

5. L.K. Arata, A.P. Dhawan, J.P. Broderick, M.F. Gaskil-Shipley, A.V. Levy, N.D. Volkow, A.P. Dhawan, and J. Mantil, "Three-dimensional anatomical model-based segmentation of MR brain images through principal axis registration," *IEEE Trans. Biomed. Engineering*, vol. 42, no. 11 (Nov), pp. 1069-1077, 1995.

6. B. Bhanu, S. Lee, and S. Das, "Adaptive image segmentation using genetic and hybrid search methods," *IEEE Trans. Aerospace Electronic Sys.*, vol. 31, no. 4, pp. 1268-1291, 1995.

7. A.E. Bowden, R.D. Rabbitt, J.A. Weiss, and B.N. Maker, "Anatomical registration and segmentation by warping template finite element models," *Proc. SPIE*, vol. 3254, pp. 469-476, 1998.

8. N.R. Pal and S.K. Pal, "Review on image segmentation techniques," *Pattern Recognition*, vol. 26, no. 9, pp. 1277-1294, 1993.

9. R.J. Qian and T.S. Huang, "Robust and accurate image segmentation using deformable templates in scale space," in *Int. Symp. Comp. Vis.,* Coral Gables, FL, pp. 206-211, 1995.

10. A.J. Yezzi, S. Kichenassami, A. Kumar, P. Olver, and A. Tannenbaum, "A geometric snake model for segmentation of medical imagery," *IEEE Trans. Med. Imaging*, vol. 16, no. 2, pp. 199-209, 1997.

11. S. Pieper, J. Rosen, and D. Zeltzer, "Interactive graphics for plastic surgery: A task-level analysis and implementation," *Proc. ACM Symp. Interactive 3D Graphics*, pp. 127-134, 1992.

12. A.E. Bowden, R.D. Rabbitt, J.A. Weiss, and B.N. Maker, "Use of medical image data to compute strain fields in a spinal disc," *Proc. ASME Bioeng. Conf.*, vol. BED-35, pp. 191-192, 1997.

13. A.E. Bowden, R.D. Rabbitt, and J.A. Weiss, "Stress and strain in the human distal phalanx under indentation," in *Proc. BMES/EMBS Conf.,* Atlanta, GA, 1999.

14. R.D. Rabbitt, A.E. Bowden, and J.A. Weiss, "Tracking nonlinear soft tissue strain using 3D medical image data and the finite element method," in *NIH Biomed Imaging Symp, "Visualizing the Future of Biology and Medicine" on the NIH campus*, June 25-26, 1999.

15. A.I. Veress, J.A. Weiss, G.T. Gullberg, G. Vince, and R.D. Rabbitt, "Validation for the determination of strain and displacement fields in coronary arteries imaged by intravascular ultrasound," *ASME BED Conference*, 2001.

16. J.A. Weiss, R.D. Rabbitt, and A.E. Bowden, "Incorporation of medical image data in finite element models to track strain in soft tissues," *SPIE Biomed. Optics Symp. BiOS98*, vol. 3254, pp. 477-484, 1998.

17. J. Hadamard, "Le probleme de cauchy et les equations aux derivees lineaires hyperboliques," *Hermann, Paris*, 1932.

18. J. Hadamard, "Sur les problemes aux derivees partielles et leur signification physique," *Bull. Univ. Princeton*, vol. 13, 1902.

19. L. Devroye, L. Gyorfi, and G. Lugosi, *A Probabilistic Theory of Pattern Recognition*, New York: Springer-Verlag, 1996.

20. C.A. Glasbey and K.V. Mardia, "A review of image-warping methods," *J. Appl. Stat.*, vol. 25, no. 2, pp. 155-172, 1998.

21. T. McInerney and D. Terzopoulos, "Deformable models in medical image analysis: A survey," *Med. Image Anal.*, vol. 1, no. 2, pp. 91-108, 1996.

22. G.E. Christensen and H.J. Johnson, "Consistent image registration," *IEEE Trans. Med. Imaging*, vol. 20, no. 7, pp. 568-582, 2001.

23. H.J. Johnson and G.E. Christensen, "Consistent landmark and intensity-based image registration," *IEEE Trans. Med. Imaging*, vol. 21, no. 5, pp. 450-461, 2002.

24. Y. Amit, "Graphical shape templates for automatic anatomy detection with applications to MRI brain scans," *IEEE Trans. Med. Imaging*, vol. 16, no. 1, pp. 28-40, 1997.

25. A.P. Dhawan, L.K. Arata, A.V. Levy, and J. Mantil, "Iterative principal axis registration method for analysis of MR-pet brain images," *IEEE Trans. Biomed. Engineering*, vol. 42, no. 11 (Nov), pp. 1069-1077, 1995.

26. A.K. Jain, Y. Zhong, and M.P. Dubuisson-Jolly, "Deformable template models: A review," *Signal Processing*, vol. 71, no. 2, pp. 109-129, 1998.

27. F.L. Bookstein, *Morphometric Tools for Landmark Data*, New York: Cambridge University Press, 1991.

28. X. Pennec, N. Ayache, and J.P. Thirion, "Landmark-based registration using features identified through differential geometry," in *Handbook of Medical Imaging*, I. Bankman, Ed., Academic Press, 2000, p. 499-513.

29. K. Rohr, "Landmark-based image analysis: Using geometric and intensity models," in *Computational Imaging and Vision*, Kluwer Academic Publishers, 2001, vol. 21.

30. C.A. Glasbey, G.W. Horgan, G.J. Gibson, and D. Hitchcock, "Fish shape analysis using landmarks," *Biometrical J.*, vol. 37, pp. 481-495, 1995.

31. C.A. Pelizzari, G.T.Y. Chen, D.R. Spelbring, R.R. Weichselbaum, and C.T. Chen, "Accurate three-dimensional registration of CT, PET and MR images of the brain," *J. Comp. Assist. Tomography*, vol. 13, pp. 20-6, 1988.

32. N.M. Alpert, J.F. Bradshaw, D. Kennedy, and J.A. Coreia, "The principal axis transformation - a method for image registration," *J. Nuclear Medicine*, vol. 31, pp. 1717-22, 1990.

33. J.C. Simo, R.L. Taylor, T.J. Schaewe, and M.I. Miller, "Quasi-incompressible finite elasticity in principal stretches: Continuum basis and numerical algorithms," *Comp. Meth. Appl. Mech. Engineering*, vol. 85, pp. 273-310, 1991.

34. M. Bro-Nielsen and C. Gramkow, "Fast fluid registration of medical images," *Visualization Biomed. Comput.*, vol. 1131, pp. 267-276, 1996.

35. A.R. Hashima, A.A. Young, A.D. McCulloch, and L.K. Waldman, "Nonhomogeneous analysis of epicardial strain distributions during acute myocardial ischemia in the dog," *J. Biomech.*, vol. 26, pp. 19-35, 1993.

36. L.K. Waldman, Y.C. Fung, and J.W. Covell, "Transmural myocardial deformation in the canine left ventricle: Normal in vivo three-dimensional finite strains," *Circ. Res.*, vol. 57, pp. 152-163, 1985.

37. N.L. Gotteiner, G. Han, K.B. Chandran, M.J. Vonesh, M. Bresticker, R. Greene, J. Oba, B.J. Kane, A. Joob, and D.D. McPherson, "In vivo assessment of nonlinear myocardial deformation using finite element analysis and three-dimensional echocardiographic reconstruction," *Am. J. Card. Imaging,* vol. 9(3), pp. 185-94, 1995.

38. A.A. Amini and J.S. Duncan, "Bending and stretching models for LV wall motion analysis from curves and surfaces," *Image Vision Comput.*, vol. 10, no. 6, pp. 418-430, 1992.

39. J. Park, D. Metaxas, and L. Axel, "Analysis of left ventricular wall motion based on volumetric deformable models and MRI-spamm," *Med. Image Anal.*, vol. 1, no. 1, pp. 53-72, 1996.

40. N. Labropoulos, M. Ashraf Mansour, S.S. Kang, D.S. Oh, J. Buckman, and W.H. Baker, "Viscoelastic properties of normal and atherosclerotic carotid arteries," *Eur. J. Vasc. Endovasc. Surg.*, vol. 19, no. 3, pp. 221-5, 2000.

41. V. Gourisankaran and M.G. Sharma, "The finite element analysis of stresses in atherosclerotic arteries during balloon angioplasty," *Crit. Rev. Biomed. Eng.*, vol. 28, no. 1-2, pp. 47-51, 2000.

42. M. Wozniak, A. Fausto, C.P. Carron, D.M. Meyer, and K.A. Hruska, "Mechanically strained cells of the osteoblast lineage organize their extracellular matrix through unique sites of alphavbeta3-integrin expression," *J. Bone Miner. Res.*, vol. 15, no. 9, pp. 1731-45, 2000.

43. C.L. de Korte, G. Pasterkamp, A.F. van der Steen, H.A. Woutman, and N. Bom, "Characterization of plaque components with intravascular ultrasound elastography in human femoral and coronary arteries in vitro," *Circulation*, vol. 102, no. 6, pp. 617-23, 2000.

44. C.L. de Korte, A.F. van der Steen, E.I. Cepedes, G. Pasterkamp, S.G. Carlier, F. Mastik, A.H. Schoneveld, P.W. Serruys, and N. Bom, "Characterization of plaque components and vulnerability with intravascular ultrasound elastography," *Phys. Med. Biol.*, vol. 45, no. 6, pp. 1465-75, 2000.

45. C.L. de Korte, H.A. Woutman, A.F. van der Steen, G. Pasterkamp, and E.I. Cespedes, "Vascular tissue characterisation with IVUS elastography," *Ultrasonics*, vol. 38, no. 1-8, pp. 387-90, 2000.

46. N. Bom, C.L. de Korte, J.J. Wentzel, R. Krams, S.G. Carlier, A.W. van der Steen, C.J. Slager, and J.R. Roelandt, "Quantification of plaque volume, shear stress on the endothelium, and mechanical properties of the arterial wall with intravascular ultrasound imaging," *Z. Kardiol.*, vol. 89, no. Suppl. 2, pp. 105-11, 2000.

47. A.I. Veress, D.G. Vince, P.M. Anderson, J.F. Cornhill, E.E. Herderick, J.D. Klingensmith, B.D. Kuban, N.L. Greenberg, and J.D. Thomas, "Vascular mechanics of the coronary artery," *Z. Kardiol.*, vol. 89, no. Suppl. 2, pp. 92-100, 2000.

48. M. Lee and W. Hyman, "Modeling of failure mode in knee ligaments depending on the strain rate," *BMC Musculoskeletal Disord.*, vol. 3, no. 1, pp. 3, 2002.

49. B. Fragniere and F. Chevalley, "Strain gauge measurements on a one-side external fixation: A prospective series of 11 tibial shaft fractures," *Rev. Chir. Orthop. Reparatrice Appar. Mot.*, vol. 87, no. 7, pp. 669-76, 2001.

50. N. Cicak, H. Klobucar, and D. Maric, "Overuse injury syndromes in the shoulder area," *Arh. Hig. Rada. Toksikol.*, vol. 52, no. 4, pp. 393-402, 2001.

51. L.C. Almekinders, J.H. Vellema, and P.S. Weinhold, "Strain patterns in the patellar tendon and the implications for patellar tendinopathy," *Knee Surg. Sports Traumatol. Arthrosc.*, vol. 10, no. 1, pp. 2-5, 2002.

52. L. Blankevoort, R. Huiskes, and A. de Lange, "The envelope of passive knee joint motion," *J. Biomech.*, vol. 21(9), pp. 705-720, 1988.

53. R. Crowninshield, M.H. Pope, and R.J. Johnson, "An analytical model of the knee," *J. Biomech.*, vol. 9, pp. 397-405, 1976.

54. D.E. Dupuy, R.M. Spillane, M.S. Rosol, D.I. Rosenthal, W.E. Palmer, D.W. Burke, and A.E. Rosenberg, "Quantification of articular cartilage in the knee with three-dimensional MR imaging," *Acad. Radiol.*, vol. 3(11), pp. 919-24, 1996.

55. J.R. Essinger, P.F. Leyvraz, J.H. Heegaard, and D.D. Robertson, "A mathematical model for the evaluation of the behavior during flexion of condylar-type knee prostheses," *J. Biomech.,* vol. 22, pp. 11-12, 1989.

56. J. Heegaard, P.F. Leyvraz, A.V. Kampen, L. Rakotomanana, P.J. Rubin, and L. Blankevoort, "Influence of soft structures on patellar three-dimensional tracking," *Clin. Orthop.,* vol. 219, pp. 235-243, 1994.

57. T.J.A. Mommersteeg, L. Blankenvoort, and R. Huiskes, "A global verirication of knee ligament models," *Proc. 41st Annual Orthopaedic Res. Soc.,* vol. 20(1), pp. 294, 1995.

58. T.J. Mommersteeg, L. Blankevoort, R. Huiskes, J.G. Kooloos, and J.M. Kauer, "Characterization of the mechanical behavior of human knee ligaments: A numerical-experimental approach," *J. Biomech.*, vol. 29(2), pp. 151-60, 1996.

59. T. Persson, "A marker-free method for tracking human lower limb segments based on model matching " *Int. J. Biomed. Comput.,* vol. 41(2), pp. 87-97, 1996.

60. J.A. Weiss, J.A. Painter, and E.P. France, "Finite element mesh generation of the knee and its soft tissues from CT data," in *Proc. 2nd World Congress Biomech.*, 1995, Amsterdam, The Netherlands, pp. 149.

61. J. Wismans, F. Veldpaus, J. Janssen, A. Huson, and P. Struben, "A three-dimensional mathematical model of the knee-joint," *J. Biomech.*, vol. 13, pp. 677-685, 1980.

62. T.M. Best, J.H. McElhaney, W.E. Garrett Jr., and B.S. Myers, "Axial strain measurements in skeletal muscle at various strain rates," *J. Biomech. Engineering*, vol. 117(3), pp. 262-5, 1995.

63. C.C. van Donkelaar, M.R. Drost, H. van Mameren, C.F. Tuinenburg, J.D. Janssen, and A. Huson, "Three-dimensional reconstruction of the rat triceps surae muscle and finite element mesh generation of the gastrocnemius medialis muscle," *Eur. J. Morphol.*, vol. 34(1), pp. 31-7, 1996.

64. D.G. Disler, M.S. Cohen, D.E. Krebs, and S.H. Roy, "Dynamic evaluation of exercising leg muscle in healthy subjects with echo planar MR imaging: Work

rate and total work determine rate of T2 change," *JMRI*, vol. 6, pp. 588-593, 1995.

65. J.W. Holmes, Y. Takayama, I. LeGrice, and J.W. Covell, "Depressed regional deformation near anterior papillary muscle," *Am. J. Physiol.,* vol. 269(1 Pt 2), pp. H262-70, 1995.

66. A. Klemencic, S. Kovacic, and F. Pernus, "Automated segmentation of muscle fiber images using active contour models," *Cytometry*, vol. 32, pp. 317-326, 1998.

67. K.A. Barbee, E.J. Macarak, and L.E. Thibault, "Strain measurements in cultured vascular smooth muscle cells subjected to mechanical deformation," *Ann. Biomed. Engineering*, vol. 22(1), pp. 14-22, 1994.

68. W.M. Vannah and D.S. Childress, "Indentor tests and finite element modeling of bulk mucular tissue in vivo," *J. Rehabilitation Res. Develop.,* vol. 33 no. 3, pp. 239-252, 1996.

69. S.M. Haney, P.M. Thompson, T.F. Cloughesy, J.R. Alger, and A.W. Toga, "Tracking tumor growth rates in patients with malignant gliomas: A test of two algorithms," *Am. J. Neuroradiology*, vol. 22, no. 1, pp. 73-82, 2001.

70. G.K. Wong, S. Haney, P.M. Thompson, J.R. Alger, T.F. Cloughesy, and A.W. Toga, "Mapping dynamic patterns of tumor growth in patients with glioblastoma multiforme," in *Proc. Society for Neuroscience*, 1999, Miami, FL.

71. N.C. Andreason, R. Rajarethinam, A.S. Cizadlo, V.W. Swayze II, L.A. Flashman, D.S. O'Leary, J.C. Ehrhardt, and W.T.C. Yuh, "Automatic atlas-based volume estimation of human brain regions from MR images," *J. Comp. Assist. Tomography*, vol. 20, no. 1, pp. 98-106, 1996.

72. M. Joliot and B.M. Mazoyer, "Three-dimensional segmentation and interpolation of magnetic resonance brain images," *IEEE Trans. Med. Imaging,* vol. 12, no. 2, pp. 269-277, 1993.

73. C. Davatzikos, "Spatial normalization of 3D brain images using deformable models," *J. Comp. Assist. Tomography*, vol. 20, no. 4, pp. 656-665, 1996.

74. D.J. Wescott and P.H. Moore-Jansen, "Metric variation in the human occipital bone: Forensic anthropological applications," *J. Forensic Sci.*, vol. 46, no. 5, pp. 1159-63, 2001.

75. R.L. Jantz, "Cranial change in Americans: 1850-1975," *J. Forensic Sci.*, vol. 46, no. 4, pp. 784-7, 2001.

76. M. Reite, P. Teale, D.C. Rojas, D. Arciniegas, and J. Sheeder, "Bipolar disorder: Anomalous brain asymmetry associated with psychosis," *Am. J. Psychiatry*, vol. 156, no. 8, pp. 1159-63, 1999.

77. M. Kass, A. Witkin, and D. Terzopoulus, "Snakes: Active contour models," *Int. J. Comp. Vision,* vol. 1, pp. 321-331, 1988.

78. L.D. Cohen, "On active contour models and balloons," *Comp. Vision. Graphics Image Proc.: Image Understanding,* vol. 53(2), pp. 211-218, 1991.

79. L. Cohen and R. Kimmel, "Global minimum for active contour models: A minimal path approach," *Int. J. Comp. Vision,* vol. 24, no. 1, pp. 57-78, 1997.

80. A.A. Amini, R.W. Curwen, A.K. Klein, T.K. Egglin, J. Pollack, F. Lee, and J.C. Gore, "Physics based snakes, kalman snakes, and snake grids for feature localization and tracking in medical images," *Comput. Imaging Vis.*, vol. 3, pp. 363-364, 1995.

81. R. Bajcsy and S. Kovacic, "Multiresolution elastic matching," *Comp. Vis. Graphics Image Proc.*, vol. 46, pp. 1-21, 1989.

82. R. Bajcsy, R. Lieberson, and M. Reivich, "A computerized system for the elastic matching of deformed radiographic images to idealized atlas images," *J. Comp. Assist. Tomography*, vol. 7, no. 4, pp. 618-625, 1983.

83. J. Gee, M. Reivich, and R. Bajcsy, "Elastically deforming 3d atlas to match anatomical brain images," *J. Comp. Assist. Tomography*, vol. 17, no. 2, pp. 225-236, 1993.

84. M. Moshfeghi, "Elastic matching of multimodality medical images," *CVGIP: Graphical Models and Image Processing*, vol. 53, pp. 271-282, 1991.

85. M. Moshfeghi, "Three-dimensional elastic matching of volumes," *IEEE Trans. Image Proc.*, vol. 3, no. 128-138, 1994.

86. T. McInerney and D. Terzopoulos, "A finite element model for 3D shape reconstruction and nonrigid motion tracking," *IEEE* vol. 2, pp. 518-533, 1993.

87. G.E. Christensen, R.D. Rabbitt, and M.I. Miller, "3D brain mapping using a deformable neuroanatomy," *Physics Med. Biol.* vol. 39, pp. 609-618, 1994.

88. G.E. Christensen, R.D. Rabbitt, and M.I. Miller, "Deformable templates using large deformation kinematics," *IEEE Trans. Image Proc.*, vol. 5, no. 10, pp. 1435-1447, 1996.

89. P.A. Freeborough and N.C. Fox, "Modeling brain deformations in alzheimer's disease by fluid registration of serial MR images," *J. Comp. Assist. Tomography*, vol. 22, pp. 838-843, 1998.

90. R.D. Rabbitt, J.A. Weiss, G.E. Christensen, and M.I. Miller, "Mapping of hyperelastic deformable templates," *Proc. SPIE*, vol. 252, pp. 252-265, 1995.

91. A.E. Bowden, R.D. Rabbitt, and J.A. Weiss, "Warping template finite element models into alignment with subject specific image data," *BED*, vol. 39, pp. 289-290, 1998.

92. D. Rueckert, L.I. Sonoda, C. Hayes, D.L.G. Hill, M.O. Leach, and D.J. Hawkes, "Nonrigid registration using free-form deformations: Application to breast MR images," *IEEE Trans. Med. Imaging*, vol. 18, no. 8, pp. 712-721, 1999.

93. E. Bardinet, L.D. Cohen, and N. Ayache, "Superquadrics and free-form deformations: A global model to fit and track 3D medical data," *Lect. Notes Comp. Science*, vol. 905, pp. 319-326, 1995.

94. D. Kucera and R.W. Martin, "Segmentation of sequences of echocardiographic images using a simplified 3D active contour model with region-based external forces," *Comput. Med. Imaging Graph.* vol. 21, no. 1, pp. 1-21, 1997.

95. A. Sebbahi, A. Herment, and A. de Cesare, "Multimodality cardiovascular image segmentation using a deformable contour model," *Comput. Med. Imaging Graph.*, vol. 21, no. 2, pp. 79-89, 1997.

96. A. del Bimbo, S. Santini, and J. Sanz, "OCR from poor quality images by deformation of elastic templates," *Proc. Int. Conf. Pattern Recognition*, vol. 2, pp. 433-435, 1994.

97. E. Lecolinet and L. Likforman-Sulem, "Handwriting analysis: Segmentation and recognition," *IEEE Colloq. Proc. Eur. Wkshp. Handwriting Anal. Recog.: A European Perspective*, vol. 123, pp. 17/1-17/8, 1994.

98. M.-P. Dubuisson, S. Lakshmanan, and A.K. Jain, "Vehicle segmentation using deformable templates," in *Int. Symp. Comp. Vision,* Coral Gables, FL, 1995, pp. 581-586.

99. K. Lam and H. Yan, "Facial feature location and extraction for computerized human face recognition," *Natl. Conf. Pub. Inst. Eng. Aust.,* vol. 1(94/9), pp. 167-171, 1994.

100. K. Lam and H. Yan, "Locating and extracting the eye in human face images," *Pattern Recognition,* vol. 29, pp. 771-779, 1996.

101. N. Sang, T. Zhang, and J. Peng, "Efficient moving target identification method," *Proc. IEEE Intl. Conf. Intelligent Processing Systems (ICIPS)*, vol. 2, pp. 1437-1441, 1998.

102. C. Gueudre, J. Moysan, and G. Corneloup, "Geometric characterization of a circumferential seam by automatic segmentation of digitized radioscopic images," *NDT & E International,* vol. 30, no. 5, pp. 279-285, 1997.

103. C.A. Pelizzari, A.C. Evans, P. Neelin, C.-T. Chen, and S. Marrett, "Comparison of two methods for 3D registration of pet and MRI images," *Annual Conf. Engineering Med. Biology*, vol. 13, pp. 221-223, 1991.

104. H. Neemuchwala, A. Hero, and P. Carson, "Feature coincidence trees for registration of ultrasound breast images," *IEEE Int. Conf. Image Process.*, vol. 3, pp. 10-13, 2001.

105. I.D. Dinov and D.W.L. Sumners, "Applications of frequency dependent wavelet shrinkage to analyzing quality of image registration," *SIAM J. Appl. Math.*, vol. 62, no. 2, pp. 367-384, 2001.

106. P. Viola and W.M. Wells III, "Alignment by maximization of mutual information," *Int. J. Comp. Vision*, vol. 24, no. 2, pp. 137-154, 1997.

107. T.M. Cover and P.E. Hart, "Nearest neighbor pattern classification," *IEEE Trans. Inform. Theory*, vol. IT-13, no. 1, pp. 21-27, 1967.

108. B.S. Everitt, *Cluster Analysis*, 3rd ed., London: Edward Arnold, 1993.

109. B.D. Ripley, *Pattern Recognition and Neural Networks*, Cambridge University Press, 1996.

110. C. Cortes and V. Vapnik, "Support vector networks," *Machine Learning*, vol. 20, 1995.

111. R. Collobert and S. Bengio, "SVMtorch: Support vector machines for large-scale regression problems," *J. Machine Learning Res.*, vol. 1, pp. 143-160, 2001.

112. A.K. Jain, R.P.W. Duin, and J. Mao, "Statistical pattern recognition: A review," *IEEE Trans. Pattern Anal. Mach. Intel.*, vol. 22, no. 1, pp. 4-37, 1999.

113. J.C. Gee and P.D. Peralta, "Continuum models for bayesian image matching," in *Maximum Entropy and Bayesian Methods*, K.M. Hanson and R.N. Silver, Eds. Kluwer Academic Publishers: Dordrecht, 1996, p. 109-116.

114. G.R. Gaudette, J. Todaro, I.B. Krukenkamp, and F.P. Chiang, "Computer aided speckle interferometry: A technique for measuring deformation of the surface of the heart," *Ann. Biomed. Eng.*, vol. 29, no. 9, pp. 775-80, 2001.

115. C.C. Moore, E.R. McVeigh, and E.A. Zerhouni, "Noninvasive measurement of three-dimensional myocardial deformation with tagged magnetic resonance imaging during graded local ischemia," *J. Cardiovasc. Magn. Reson.*, vol. 1, no. 3, pp. 207-22, 1999.

116. X. Papademetris, A.J. Sinusas, D.P. Dione, and J.S. Duncan, "Estimation of 3d left ventricular deformation from echocardiography," *Med. Image Anal.*, vol. 5, no. 1, pp. 17-28, 2001.

117. D.E. Harrison, D.D. Harrison, T.J. Janik, J.E. William, R. Cailliet, and M. Normand, "Comparison of axial and flexural stresses in lordosis and three buckled configurations of the cervical spine," *Clin. Biomech.*, vol. 16, no. 4, pp. 276-84, 2001.

118. Y. Zhu, P. Chaturvedi, and M.F. Insana, "Strain imaging with a deformable mesh," *Ultrasonic Imaging*, vol. 21, no. 2, pp. 127-46, 1999.

119. T.S. Gross, J.L. Edwards, K.J. McLeod, and C.T. Rubin, "Strain gradients correlate with sites of periosteal bone formation," *J. Bone Miner. Res.*, vol. 12, no. 6, pp. 982-8, 1997.

120. C. Pierre-Jerome, S.I. Bekkelund, G. Husby, S.I. Mellgren, M. Osteaux, and R. Nordstrom, "MRI of anatomical variants of the wrist in women," *Surg. Radiol. Anat.*, vol. 18, no. 1, pp. 37-41, 1996.

121. T.G. Reese, R.M. Weisskoff, R.N. Smith, B.R. Rosen, R.E. Dinsmore, and V.J. Wedeen, "Imaging myocardial fiber architecture in vivo with magnetic resonance," *Magn. Reson. Med.*, vol. 34, no. 6, pp. 786-91, 1995.

122. S.I. Simon and G.W. Schmid-Schonbein, "Cytoplasmic strains and strain rates in motile polymorphonuclear leukocytes," *Biophysical J.*, vol. 58, pp. 319-332, 1990.

123. A.D. McCulloch, B.H. Smaill, and P.J. Hunter, "Regional left ventricular epicardial deformation in the passive dog heart," *Circ. Res.,* vol. 64, pp. 721-733, 1989.

124. W.P. Smutz, M. Drexler, L.J. Berglund, E. Growney, and K.N. An, "Accuracy of a video strain measurement system," *J. Biomech.,* vol. 29(6), pp. 813-7, 1996.

125. Z. Jia and S.P. Shah, "Two-dimensional electronic-speckle-pattern interferometry and concrete-fracture processes," *Exp. Mech.*, vol. 34, no. 3, pp. 262-70, 1994.

126. E.H. Jordan, S.C.U. Ochi, D. Pease, and J.I. Budnick, "Microradiographic strain measurement using markers," *Exp. Mech.,* vol. 34(2), pp. 155-165, 1994.

127. J.O. Hjortdal and P.K. Jensen, "In vitro measurement of corneal strain thickness and curvature using digital image processing," *Acta Ophthalmol. Scand.,* vol. 73(1), pp. 5-11, 1995.

128. D.J. Wissuchek, T.J. Mackin, M. DeGraef, G.E. Lucas, and A.G. Evans, "Simple method for measuring surface strains around cracks," *Exp. Mech.,* vol. 36(2), pp. 173-9, 1996.

129. H. van Bavel, M.R. Drost, J.D.L. Wielders, J.M. Huyghe, A. Huson, and J.D. Janssen, "Strain distribution on rat medial gastrocnemius (MG) during passive stretch," *J. Biomech.*, vol. 29(8), pp. 1069-74, 1996.

130. D.J. Dingley, "Advances in strain measurement using electron-backscatter diffraction in the scanning electron microscope," *Proc. Annual Meet. Microsc. Soc. Am.*, pp. 602-603, 1994.

131. W. Steinchen, L.X. Yang, and G. Kupfer, "Digital shearography for determining the 2d - straintensor," *Proc. 3rd Biennial Joint Conf. Eng. Sys. Design Anal. ESDA,* vol. 76, no. 4, pp. 35-41, 1996.

132. J.A. Weiss, D.A. Schauer, and J.C. Gardiner, "Modeling contact in biological joints using penalty and augmented lagrangian methods," *Proc. ASME Winter Annual Meeting*, vol. BED-33, pp. 347-348, 1996.

133. J.A. Weiss, J.C. Gardiner, and K.M. Quapp, "Material models for the study of soft tissue mechanics," in *Proc. Int. Conf. on Pelvic and Lower Extremity Injuries,* pp. 249-261, 1995.

134. Y.K. Kang, H.C. Park, Y. Youm, I.K. Lee, M.H. Ahn, and J.C. Ihn, "Three dimensional shape reconstruction and finite element analysis of femur before and after the cementless type of total hip replacement," *J. Biomed. Eng.,* vol. 15(6), pp. 497-504, 1993.

135. B.N. Maker, R.M. Ferencz, and J.O. Hallquist, "NIKE3D a nonlinear implicit three-dimensional finite element code for solid and structural mechanics," *UC - Lawrence Livermore National Laboratory Report*, UCRL-MA-105268 rev 1, 1995.

136. J.C. Gardiner and J.A. Weiss, "Effects of flexion angle and valgus rotation on stresses in the human medial collateral ligament," *Proc. ASME Bioeng. Conf.,* vol. BED-35, pp. 27-28, 1997.

137. N. Maurel, A. Diop, J. Grimberg, and S. Elise, "In vitro biomechanical analysis of glenoids before and after implantation of prosthetic components," *J. Biomech.*, vol. 35, no. 8, pp. 1071-80, 2002.

138. P.P. Dendy and H. B, *Physics for diagnostic radiology*, 2nd ed., London: Institute of Physics, 1999.

CHAPTER 3

REGULARIZATION TOOLS FOR DEFORMABLE TEMPLATE BASED IMAGE REGISTRATION METHODS

Introduction

In 1902 Jacques Hadamard classified mathematical problems as either "well-posed" or "ill-posed." He defined a "well-posed" problem as one with an existing, unique and well-conditioned solution [1], [2]. Hadamard believed that all naturally occurring problems fell into this category and were considered to be solvable. A problem that did not meet these criteria was considered "ill-posed," and unsolvable.

Contrary to Hadamard's belief, ill-posed problems of practical interest arise naturally in many areas of science and engineering. Many biomedical image registration problems do not have a unique solution, and fall into this category. In order to solve these problems, the solution space must be restricted using some form of applied constraints or optimization criteria (a.k.a. image similarity measure). As was discussed in Chapter 2 of the present work, image registration techniques are defined by their applied constraint system. In many cases, however, restricting the solution space still does not guarantee a unique solution. The problem is most common in deformable template based registration methods, where the problem solution is guided by optimization of a potential function. Local similarities in image

data (regions of the template and target images that are similar in intensity, gradient, border information, etc.) can confound global registration of the image data. Mathematically these similarities appear as local minima in the potential function that is being optimized. In theory, the higher the dimension of the transformation, the more local minima present in the potential function [3].

During registration, the template image is deformed to align with the target image field. The magnitude of the registration force is based on both the difference in absolute pixel intensities between these fields and on gradient information (see Appendix). In the ideal case, the target represents a "perfect" transformation of the template and registration progresses until the template image is perfectly aligned with the target (and the registration forces are brought into balance with the internal energy of the deformation).

Real image data, however, present a greater challenge. No perfect transformation exists. Thus, the registration consists of balancing conflicting image information (due to imaging artifacts or variability between subjects) and internal energy generated during deformation. Locations on the template and target images containing similar intensity and gradient information will attract each other, whether or not the deformation represents a correct registration. Thus, local image information can interfere with global registration. This represents a local minima in the combined energy functional used for registration and is common to most deformable template registration techniques [4-6].

In this chapter, several techniques for regularization of image registration problems are presented. The techniques were developed and applied to a deformable

template based image registration algorithm, which was implemented into the nonlinear, implicit FE code, NIKE3D [7-9]. The code was designed to align a template model (consisting of both a material representation of the image space and the template image data) with target image data. The target image space was assumed to be a transformed version of the template image field. The mathematical problem was to search through all admissible deformed configurations of the template for the one that minimized the difference between the transformed template and target data, while simultaneously minimizing the strain energy of the deformation. Mathematical details of the implementation are given in Appendix.

Details of the development and implementation of a series of regularization tools are given below. Practical application of these tools to a variety of both simulated and real problems is presented in Chapter 4 of this dissertation. The regularization tools detailed in this chapter are characterized as preprocessing, integral, or postprocessing tools.

Regularization Tools: Preprocessing

Preprocessing tools address inconsistencies in medical image data due to the stochastic nature of image acquisition devices, as well as differences in acquisition techniques, which can occur in intersubject registration. These tools are primarily concerned with adjusting for overall differences in image intensity and contrast between the template and target images.

Histogram Stretching

In many medical imaging modalities, signal intensity decays non-uniformly over time, not only resulting in a general decrease in image intensity, but also affecting the composition of the intensity histogram. Additionally, in the case of inter-subject registrations, template and target images have often been acquired with different hardware or imaging parameters (e.g., in X-Ray CT the peak voltage, current, and exposure time may be different). Because of these factors, the image histograms of the template and target may be significantly different and can result in incorrect image registration. One way to partially accommodate such difficulties is to match the centroids of template and target image intensity histograms. A simplified version of the technique used by Dale-Jones and Tjahjadi [10] is utilized in the present work.

First the area centroids and extreme values of the intensity histograms of both the template and target image datasets are computed. For an arbitrary image histogram with singularly spaced discrete intensity values i ranging from I_{min} to I_{max} and frequency of occurrence $v(i)$, the area centroids of the histogram may be computed using

$$\bar{i} = \frac{\sum_{i=I_{\min}}^{I_{\max}} i \cdot v(i)}{\sum_{i=I_{\min}}^{I_{\max}} v(i)} \qquad \bar{v} = \frac{\sum_{i=I_{\min}}^{I_{\max}} [v(i)]^2}{\sum_{i=I_{\min}}^{I_{\max}} v(i)}. \tag{3.1}$$

For an arbitrary image A with intensity values $A(n)$, containing N voxels the histogram area centroids may be computed more directly as:

$$\overline{i^{(A)}} = \frac{N}{I_{\max} - I_{\min}} \qquad \overline{v^{(A)}} = \frac{\sum_{n=1}^{N} A(n)}{N}. \tag{3.2}$$

Following calculation of these values for both the template, (*T*) and target, (*s*) image datasets, the target voxel intensity values *s(n)* are scaled in order to match the target histogram intensity centroid ($\overline{i^{(s)}}$) with that of the template ($\overline{i^{(T)}}$):

$$\begin{aligned} s^*(n) &= \left(s(n) - I_{\min}^{(s)}\right)\frac{\overline{i^{(T)}} - I_{\min}^{(T)}}{\overline{i^{(s)}} - I_{\min}^{(s)}} + I_{\min}^{(T)} \qquad for\ s(n) < \overline{i^{(s)}} \\ s^*(n) &= \left(s(n) - \overline{i^{(s)}}\right)\frac{I_{\max}^{(T)} - \overline{i^{(T)}}}{I_{\max}^{(T)} - \overline{i^{(s)}}} + \overline{i^{(T)}} \qquad for\ s(n) \geq \overline{i^{(s)}} \end{aligned}. \tag{3.3}$$

The frequency centroid of intensity histogram ($\overline{v^{(s*)}}$) of the adjusted target (s^*) is then computed and scaled to match that of the template image intensity histogram.

$$s^{**}(n) = s^*(n)\frac{\overline{v^{(T)}}}{\overline{v^{(s*)}}}. \tag{3.4}$$

Results obtained using this technique were reported by Bowden [5], [11].

Singular Value Replacement

Improvements in correspondence between the histogram of the target data with the template image can also be accomplished by replacing the singular values of the target image with those of the deformed template image. The technique is based on the Singular Value Decomposition (SVD) [12-14]. The premise is that any real *x*-by-*y* matrix ***A*** can be decomposed such that

$$\boldsymbol{A} = \boldsymbol{U}\boldsymbol{\Sigma}\boldsymbol{V}^{\mathrm{T}}. \tag{3.5}$$

Here, $\boldsymbol{U}$ and $\boldsymbol{V}$ are orthonormal matrices whose columns contain the singular *vectors* of the decomposition, and the diagonal matrix, $\boldsymbol{\Sigma} = diag(\sigma_1,\ldots,\sigma_r)$, $r = min(x,y)$ with $\sigma_1 \geq \ldots \geq \sigma_r \geq 0$, contains the singular *values* of the decomposition. For clarity, a particular singular value is referenced as σ_i. SVD has found wide application in image compression and for evaluating the "noise level" of a matrix system or image based on the singular values [15].

The original matrix $\boldsymbol{A}$ is easily retrieved following decomposition by multiplication of the component matrices. An interesting observation is that the $\boldsymbol{U}$ and $\boldsymbol{V}$ matrices represent positional data, essentially a topological mapping of intensity information contained in the $\boldsymbol{\Sigma}$ matrix to the $\boldsymbol{A}$ matrix. This observation is the basis of the singular value topology tracking technique discussed in Chapter 5 of this dissertation.

Since a fundamental assumption of all deformable template based image registration methods is that the target image is a transformed version of the template, containing the same elements as the template, but at different spatial locations within the image data, it follows that $\boldsymbol{\Sigma}^{(T)} = \boldsymbol{\Sigma}^{(s)}$. Real variability between sensors and subjects will of course influence the actual values of $\boldsymbol{\Sigma}^{(T)}$ and $\boldsymbol{\Sigma}^{(s)}$, but by enforcing this constraint, we can improve the correspondence between the histogram of the target image with that of the Template image. In 2D,

$$\boldsymbol{s}^{*} = \sum_{n=1}^{N} \boldsymbol{u}_n \left({}^{(T)}\sigma_n \boldsymbol{I}_n \right) \boldsymbol{v}_n^{\boldsymbol{T}}, \tag{3.6}$$

where the lower case singular vectors ($\boldsymbol{u}_n$, $\boldsymbol{v}_n$) correspond to individual (column) vectors of the target $\boldsymbol{s}$, but the singular values ${}^{(T)}\sigma_n$ are those of the deformed template. This operation has the effect of changing the overall intensity of each target mode to match the corresponding mode in the deforming template without changing the topology or spatial distribution within the mode. $\boldsymbol{I}_n$ refers to a depleted identity matrix containing zeroes in all matrix locations, except the main diagonal entry in the nth position.

To apply SVD to 3D image data it is necessary to extend the concepts beyond the classical 2D matrix framework. There are several ways in which this could be done. In the present work the matrix containing the image intensity data $\boldsymbol{A}$ was arranged in a 3D rectangular format and decomposed separately for each image slice k (k=1…K),

$$\boldsymbol{A}^{(k)} = \boldsymbol{U}^{(k)}\boldsymbol{\Sigma}^{(k)}\boldsymbol{V}^{(k)^T} \tag{3.7}$$

to obtain a stacked set of 2D SVDs. The singular values from the stacked slices were then assembled as columns of a new matrix $\tilde{\boldsymbol{A}}$:

$$\tilde{\boldsymbol{A}} = \left[\boldsymbol{\Sigma}^{(1)} \quad \boldsymbol{\Sigma}^{(1)} \quad \ldots \quad \boldsymbol{\Sigma}^{(1)}\right] \tag{3.8}$$

This matrix, containing slice-by-slice singular values, was then subjected to a second SVD:

$$\tilde{\boldsymbol{A}} = \tilde{\boldsymbol{U}}\tilde{\boldsymbol{\Sigma}}\tilde{\boldsymbol{V}}^T \tag{3.9}$$

The n[th] 3D singular mode ($\tilde{\boldsymbol{A}}_n$) was obtained by applying Eqs. 3.7 - 3.9 to the n[th] singular value. For the k[th] slice this provides

$$\boldsymbol{A}_n^{(k)} = \boldsymbol{U}^{(k)}\boldsymbol{\Sigma}_n^{(k)}\boldsymbol{V}^{(k)^T} . \tag{3.10}$$

The matrix $\boldsymbol{\Sigma}_n^{(k)}$ was constructed in 3D for the k[th] slice of the n[th] singular mode using

$$\boldsymbol{\Sigma}_n^{(k)} = \left(\tilde{\boldsymbol{U}}\,\tilde{\boldsymbol{\Sigma}}_n\tilde{\boldsymbol{V}}^T\right)_k^T \boldsymbol{I} \ , \tag{3.11}$$

where $\tilde{\boldsymbol{\Sigma}}_n$ was obtained by zeroing all elements in $\tilde{\boldsymbol{\Sigma}}$ with the exception of $\tilde{\sigma}_n$, the subscript k denotes the k[th] column, and $\boldsymbol{I}$ is the identity matrix. Note that this reduces to the 2D case described above if all slices are identical. Although this approach is not the only possible 3D decomposition, it preserves the hierarchical property and has well-defined inner-products. Eqs. 3.7 - 3.11 will be referred to herein as 3D SVD.

Using these equations, a 3D singular value replacement may be defined as:

$$\tilde{\boldsymbol{s}}^* = \sum_{n=1}^{N} \tilde{\boldsymbol{u}}_n \left({}^{(T)}\tilde{\sigma}_n \boldsymbol{I}_n \right) \tilde{\boldsymbol{v}}_n^{\boldsymbol{T}} \tag{3.12}$$

Results obtained using this technique were reported by Bowden [5].

Regularization Tools: Integral

Integral tools are applied during the image registration process to avoid local minima solutions. In general, two types of local minima solutions are likely to occur during the Warping process. Euphemistically, they could be referred to as the “train

wreck" and the "shoving match." As part of the present work, tools have been developed to deal with each type.

The train wreck occurs when several portions of the template and target images contain similar intensity and gradient values. This situation is common in many biological problems, but it is especially common in neuroanatomical registrations. The analogy to a train wreck follows: Two trains are traveling along the same track, both carrying similar cargo, but bound for different destinations. Unfortunately, the first train mistakenly stops at the first city, leaving the second train unable to reach its destination (since the first train is already there), but unable to travel to the second city (because there is only one track). Similarly, sometimes during image registration, local template image information must pass through regions of similar intensity in the target in order to reach the appropriate destination. If the correspondence between template and target is high enough, the registration process can get "stuck", making further progress in the registration impossible, because of the penalty imposed on deviating from the current template configuration. Figure 3.1 shows an example of train wreck local minima that occurred during registration of macaque brain cryosections (macaque cryosection data provided by D.C. Van Essen of Washington University). The arrows indicate the particular areas of the images that cause the problem.

The second type of local minima that commonly occurs during registration is the shoving match. The shoving match is more often encountered during nonphysical registration problems, such as intersubject registration. The analogy hearkens to a

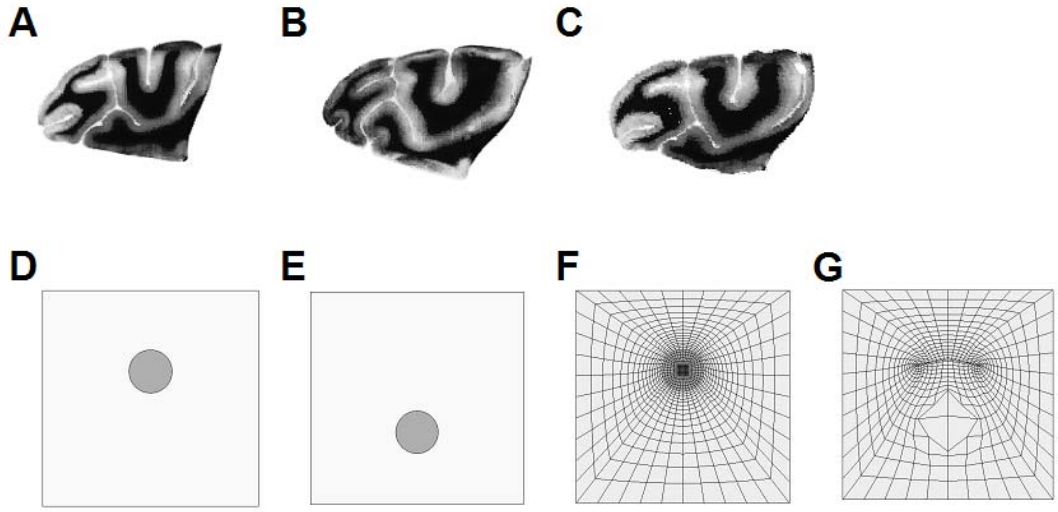

Figure 3.1. Examples of typical local minima solutions. Panels A and B show the template and target images from a macaque neuroanatomical registration. Panel C shows the "train wreck" local minima solution. Note that many of the sulcal regions have similar image intensity/gradient. These regions can interfere with global registration. Panels D and E show the template and target images, which resulted in a "shoving match" type local minima solution. The dark occlusions do not overlap, and surrounding areas of the images lack sufficient gradient and image texture to drive deformation. Panel F shows the discretized template model before deformation. Panel G shows discretized template in a local minima solution. The FE mesh cannot deform further without element inversion.

schoolyard quarrel where the two combatants face off, neither willing to move. The first combatant pushes the other, lightly at first, the other responds in kind. Push turns to shove until both are shoving the other as hard as they can. Similarly, sometimes image information would dictate continued deformation of the template model, however material constraints placed on the deformation (most commonly related to the bulk modulus in Warping problems), penalize that mode of deformation. As the penalty parameter is increased (see equation A.6 in the appendix), the associated Warping force increases. Incremental deformation of the FE mesh simply increases the material resistance to further deformation (often because surrounding elements have already become locked into place), until finally an element is inverted, causing

premature termination of the solution process. Figure 3.1 also shows an example of a "shoving match" type problem that cannot be solved without regularization. A dense occlusion in a soft billet was subjected to gravity loading such that following deformation the occlusions did not overlap. The regions of the images corresponding to the billet lack sufficient texture to drive deformation. Panel F shows the discretized template model before deformation. Panel G shows discretized template in a local minima solution. The FE mesh cannot deform further without element inversion. Without regularization, the Warping algorithm attempted to expand the region surrounding the target inclusion, while simultaneously shrinking the region surrounding the template inclusion.

Dynamic Spatial Filtering (FFT & SVD)

One way to regularize the registration problem and potentially overcome "train wreck" (and some "shoving match") type of local minima is to spatially filter the template and target image data during the registration process. Smaller image features are obscured in favor of more dominant ones. The registration can then proceed to smoothly align these dominant, global features and lock them into place. The filtering is gradually removed, allowing registration of higher frequency detail, until the registration is complete.

One method of spatially filtering 3D image data is by convolution of the image with a filtering kernel $k(\boldsymbol{X})$:

$$t^*(\boldsymbol{X}) = t(\boldsymbol{X}) * k(\boldsymbol{X}) = \int_{\beta} t(\boldsymbol{X}) k(\boldsymbol{X} - \boldsymbol{Z}) d\boldsymbol{Z} \tag{3.13}$$

where $t(\boldsymbol{X})$ and $t^*(\boldsymbol{X})$ are the original image data and the filtered data respectively, $\boldsymbol{X}$ is a vector containing the material coordinates and $\boldsymbol{Z}$ is the frequency representation of $\boldsymbol{X}$. Since convolution in the spatial domain is equivalent to multiplication in the frequency domain, an efficient way to accomplish this calculation is through the use of the discrete Fourier transform.

$$T^*(\boldsymbol{Z}) = \Im\{t^*(\boldsymbol{X})\} = T(\boldsymbol{Z})K(\boldsymbol{Z}) \tag{3.14}$$

Once the data are in Fourier space, a simple multiplication is applied and then the transform is inverted to obtain the convolved image in the spatial domain.

$$t^*(\boldsymbol{X}) = \Im^{-1}\{T(\boldsymbol{Z})K(\boldsymbol{Z})\} \tag{3.15}$$

Because of the highly optimized algorithms developed for applying Fourier transforms [16], this method is significantly faster than computing the convolution in normal image space. Changes in the filter are applied by changing the convolution function k. Different filter kernels have been successfully used, including a Gaussian kernel and a simple Heaviside function. The technique has been used extensively in the Musculoskeletal Research Labs at the University of Utah [4], [5], [17-19]. An example of using dynamic Gaussian spatial filtering during registration of macaque cryosection images is given in Figure 3.2.

As part of the present work, we have developed and applied another dynamic spatial filtering technique based on SVD. The technique exploits the hierarchical nature of the decomposition, in that the most significant image information is

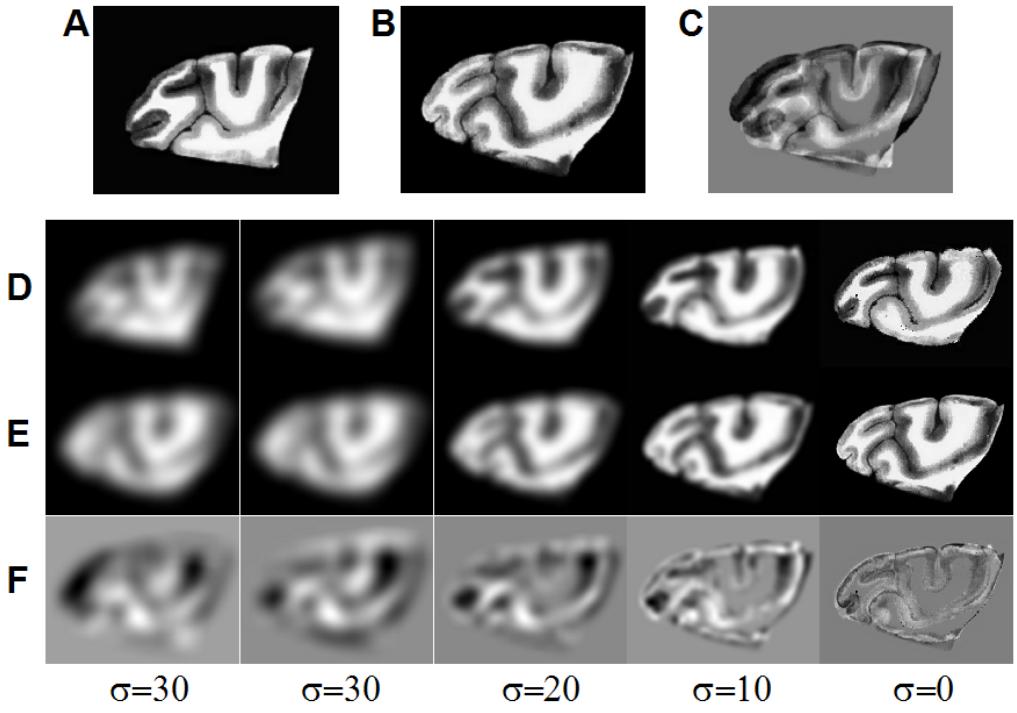

Figure 3.2. Dynamic Gaussian spatial filtering. Panels A, B, and C show the Template, Target, and initial subtraction (Template-Target) images, respectively. During the solution process, the Template and Target images are convolved with Gaussian kernel functions. Initially large variance values for the kernel are used, then progressively smaller values as registration nears completion. Rows D, E, and F show the filtered versions of the Template, Target, and subtraction images at incremental points in solution time.

contained in the first singular values/vectors. To utilize the technique, both the template and target images are decomposed using the SVD (Eq. 3.5, 3.9). The images are then reconstructed with a truncated version of $\boldsymbol{\Sigma}$:

$$\boldsymbol{A}^{*} = \sum_{n=1}^{m} \boldsymbol{u}_n \left(\sigma_n \boldsymbol{I}_n\right) \boldsymbol{v}_n^{T} \tag{3.16}$$

where $m < N$ and $\boldsymbol{u}_n$, σ_n, and $\boldsymbol{v}_n$ are all from SVD of the corresponding template or target image. When only the few largest singular values are used for reconstructing

the regularized images, the images are reduced to their most basic components and local details are obscured. Following registration of these regularized images, new versions of the template and target images are generated with progressively more singular values. The process continues until all of the singular values are included ($m \rightarrow N$), and the complete images are registered. The 3D version is applied similarly as:

$$\tilde{\boldsymbol{A}}^{*} = \sum_{n=1}^{m} \tilde{\boldsymbol{u}}_n \left(\tilde{\sigma}_n \boldsymbol{I}_n \right) \tilde{\boldsymbol{v}}_n^{T} \tag{3.17}$$

In this manner, the most significant singular values from the most significant slices are registered first, and then progressively more image detail is added during the registration process.

The evolution of the macaque cryosection registration problem using the progressive SVD filter is shown in Figure 3.3. The technique may be used in conjunction with the Singular Value Replacement technique described previously. Although computation of the SVD algorithm is somewhat time-consuming, it need only be performed once for each image set. Reconstruction of the image data at each change in the number of included singular values *m*, is a simple matrix multiplication process. This is in contrast to other spatial filter algorithms, which generally involve major computational effort at each change in filter dimension. For example, the convolution of an image with a Gaussian filter of 5 voxels cannot be directly obtained from knowledge of the convolution result with a Gaussian filter of 3 voxels without performing another convolution operation. Thus the SVD algorithm is often more efficient than these techniques.

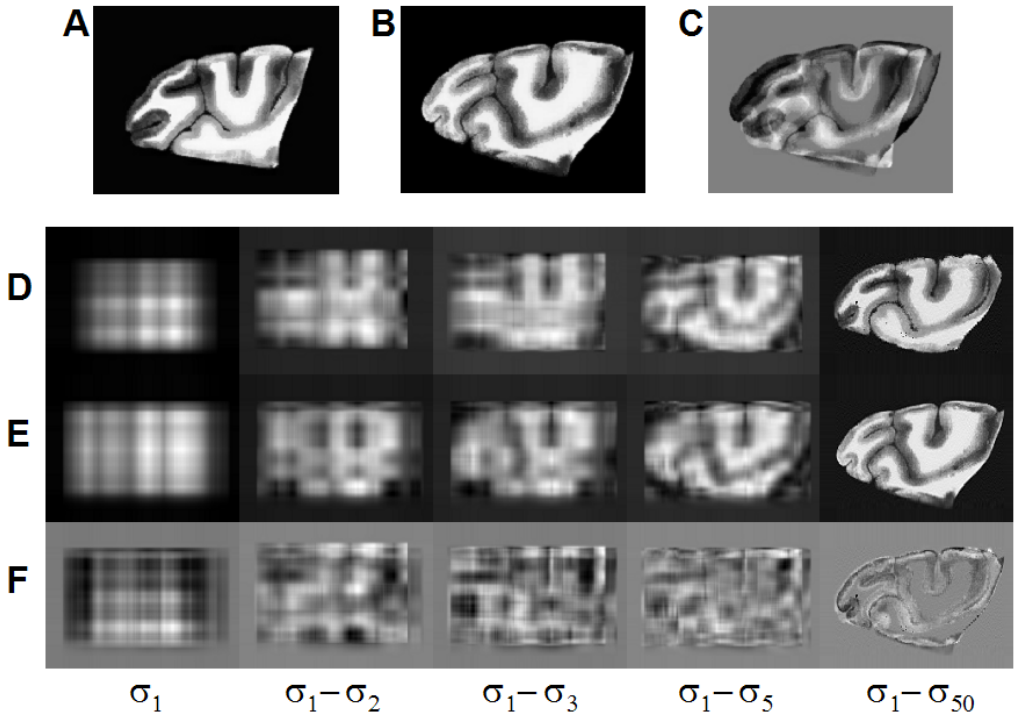

Figure 3.3. Dynamic SVD spatial filtering. Panels A, B, and C show the Template, Target, and initial subtraction (Template-Target) images, respectively. The Template and Target images are decomposed using the SVD. During the solution process, the images are reconstructing using progressively more singular values. Rows D, E, and F show the filtered versions of the Template, Target, and subtraction images at incremental points in solution time.

The potential advantage of using an SVD filter over a Gaussian filter is that registration progresses naturally through the principal modes of the image data. Practically, the technique is susceptible to local minima during the intermediate steps (for example, reference panels B-F of Figure 3.2).

FE Rezoning

During large deformation registration problems, FE discretization levels can be insufficient to track kinematics of very complicated displacement patterns. Rezoning

allowed for larger nodal displacements and more complicated element deformation fields by periodically restoring the finite element mesh to its undeformed state during computation. At this point, material stresses were reset to zero, and template image intensity and nodal displacements were interpolated from the nodes of the deformed FE mesh to those of the reset mesh. The analysis then continued until the convergence criteria were met or another rezoning was required. Strain values were computed following registration using standard FE techniques from the accumulated nodal displacements computed at each remesh point.

The rezoning procedures required interpolation of the template image data T and the accumulated nodal displacements $\boldsymbol{u}(\boldsymbol{X})$ from the deformed FE mesh to the nodes of the reset mesh. For each node N in the undeformed mesh, the element in deformed mesh that contains the node is located by comparing the natural coordinates (ξ_N, η_N, and ζ_N) of the node in each deformed element (successful location requires $-1 < \xi_N, \eta_N, \zeta_N < 1$). Once the natural coordinates of the node in the element local coordinate system were determined, the value of the quantity to be interpolated could be obtained for the node of the reset mesh by interpolation using the trilinear shape functions for the eight-noded hexahedral element [20].

The relationship between the global coordinates and the local element coordinates was required to perform the interpolation. For this, the local coordinates of the eight nodes of the element containing N were assembled into an 8x3 matrix $\boldsymbol{\phi}(\xi_i, \eta_i, \zeta_i)$, where ξ_i, η_i, and ζ_i are the local element coordinates of the nodes composing the element; for instance, node 1 has local coordinates (-1, -1, -1). An 8x8 matrix $\boldsymbol{G}$ was assembled to contain the global nodal coordinates and the products of

these coordinates as per the shape function definitions. The local coordinates were related to the global coordinates via the interpolating polynomial constants arising from the shape functions as follows:

$$[\phi]=[G][\alpha]\Leftrightarrow\begin{bmatrix}-1 & -1 & -1\\ . & . & .\\ . & . & .\\ 1 & 1 & 1\end{bmatrix}=\begin{bmatrix}1 & x_1 & y_1 & z_1 & x_1y_1 & y_1z_1 & x_1z_1 & x_1y_1z_1\\ . & . & . & . & . & . & . & .\\ . & . & . & . & . & . & . & .\\ 1 & x_8 & y_8 & z_8 & x_8y_8 & y_8z_8 & x_1z_8 & x_8y_8z_8\end{bmatrix}\begin{bmatrix}a_1 & b_1 & c_1\\ . & . & .\\ . & . & .\\ a_8 & b_8 & c_8\end{bmatrix}$$

(3.18)

Here, $\boldsymbol{\alpha}$ is an 8x3 matrix containing the polynomial coefficients and (x_i, y_i, z_i) are the coordinates of the corner nodes of the deformed element in the global coordinate system. The matrix $\boldsymbol{\alpha}$ was determined for each element in the reset mesh:

$$[\alpha]=[G]^{-1}[\phi]\ . \tag{3.19}$$

The local element coordinates (ξ_N, η_N, ζ_N) of node N follow from $\boldsymbol{\alpha}$ and the global coordinates (x_N, y_N, z_N):

$$[\xi_N \quad \eta_N \quad \zeta_N]=[1 \quad x_N \quad y_N \quad z_N \quad x_Ny_N \quad y_Nz_N \quad x_Nz_N \quad x_Ny_Nz_N]\begin{bmatrix}a_1 & b_1 & c_1\\ . & . & .\\ . & . & .\\ a_8 & b_8 & c_8\end{bmatrix}.$$

(3.20)

The interpolated values can then be computed from the local coordinates, the nodal values, and the trilinear shape functions. For example, the interpolated template intensity was computed using

$$T_N\left(\xi_{\mathrm{N}},\eta_{\mathrm{N}},\zeta_{\mathrm{N}}\right) = \sum_{i=1}^{8} T_i\, h_i\left(\xi_{\mathrm{N}},\eta_{\mathrm{N}},\zeta_{\mathrm{N}}\right), \tag{3.21}$$

where the T_{i} are intensity values at each node in the deformed element and h_{i} are the shape functions corresponding to each node evaluated at $\left(\xi_{\mathrm{N}},\eta_{\mathrm{N}},\zeta_{\mathrm{N}}\right)$ [20]:

$$h_i = \frac{1}{8}\left(1-\xi_N\xi_i\right)\left(1-\eta_N\eta_i\right)\left(1-\zeta_N\zeta_i\right). \tag{3.22}$$

As an example, for node 8 with local coordinates (1,1,1) the shape function would be

$$h_8 = \frac{1}{8}(1-\zeta_N)(1-\eta_N)(1-\xi_N). \tag{3.23}$$

The accumulated nodal displacements $\boldsymbol{u}(\boldsymbol{X})$ were interpolated using the same procedure. Note that this interpolation strategy is consistent with the shape functions used in the FE solution process. A graphic illustration of the technique is given in Figure 3.4. Panels A and B of the figure show the template and target images, respectively. The template evolution Results using the technique on mouse neuroanatomies have been reported in the literature [17].

Sequential Image Registration

In strain-tracking registration problems, it is often possible to avoid train wreck type local minima by using additional target images acquired at intermediate stress states during the deformation. Utilizing additional images also allows more accurate computation of developed stress for materials that have path dependent material characteristics (such as viscoelastic and elastic-plastic materials).

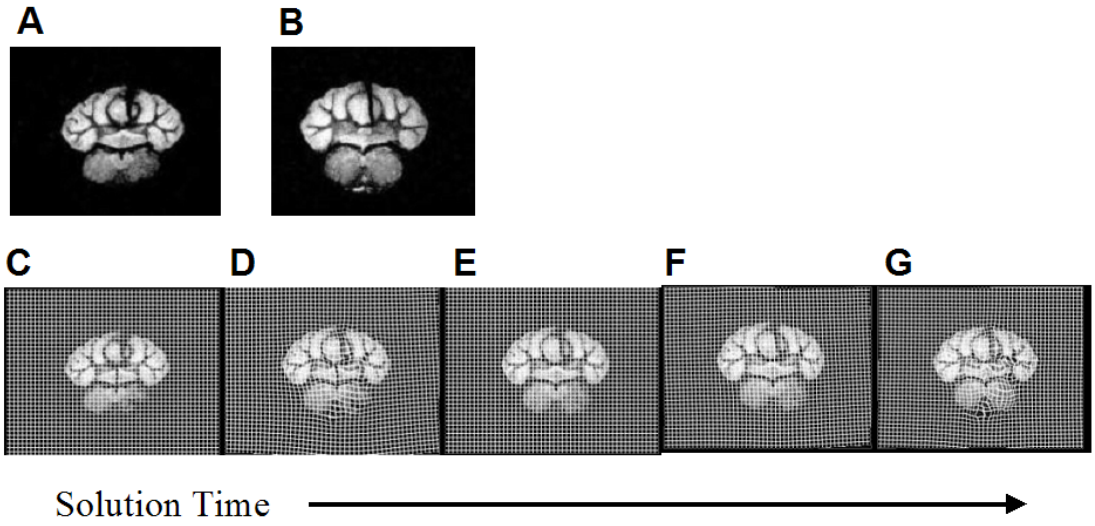

Figure 3.4 Rezoning during mouse neuroanatomy registration. Panels A and B show the Template and Target images, respectively. Panels C-G show the deforming FE mesh overlaid onto the deforming template image. At panel D, the mesh has almost become sufficiently distorted to start inverting elements. A rezoning operation is performed and the mesh reset to its initial configuration (Panel E). Registration then continues to completion.

This regularization technique has been implemented into the Warping code using the restart capabilities of NIKE3D [9]. Accumulated nodal displacements and element stresses (as well as template image information) are stored to disk following registration of the template image with the first sequential target image. The registration problem is then restarted from the previous termination point, but with the next sequential target image. The procedure continues until registration of the template with the final target image has been completed.

For accurate stress computation using rate-dependent material models, it is important to accurately specify the acquisition time of each sequential target image. This is in contrast to a typical quasi-static Warping problem, where time is irrelevant

and simply used for gradually increasing the penalty parameter λ (see Eq. A.6 in Appendix A).

Regularization Tools: Postprocessing

Postprocessing tools facilitate accurate visualization and evaluation of the computed registration solution. Additionally, because image registration is often an iterative process, postprocessing tools often guide variation in registration parameters during iterations, as well as providing stopping criteria.

Mapper3D

In most cases, the nodal points of the computational FE mesh used for image registration are not co-located with the image voxels. Following image registration, the computed registration map must be applied to the original template image in order to accurately view the results and compare the registered template image with the target image. For simple equi-spaced rectilinear meshes, tools such as the visualization toolkit (vtk) [21] are available. Many registration problems, however, are more suited to a FE mesh that conforms to specific areas of interest within the template image data. In some cases, a subject-specific mesh that excludes the spatial domain of irrelevant background image data, can avoid shoving match type local minima that occur using a rectilinear mesh. For these problems, custom software (Mapper3D) was written to map the computed deformations into the template image space.

Mapper3D uses an optimized version of the technique described for rezoning (Eq. 3.18 – 3.23) to locate the particular deformed finite element corresponding to the

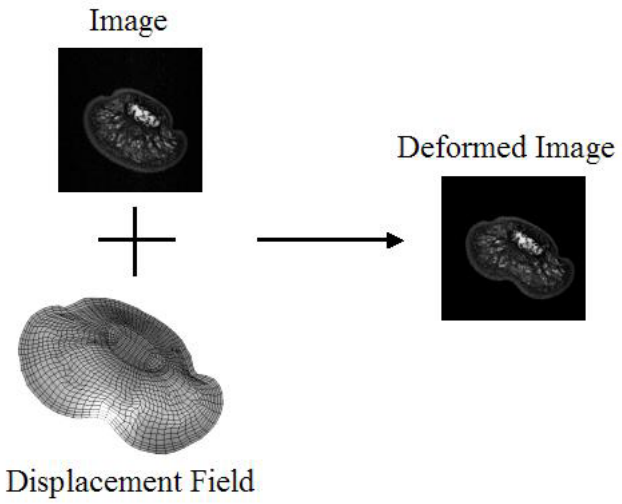

Figure 3.5. Mapper3D. Mapper3D uses the trilinear FE shape functions to apply a computed displacement field to an image.

location of each image voxel in the deformed template image. The standard tri-linear shape functions from isoparametric finite element analysis are then used to determine the original location of that voxel in the undeformed template image. The template image intensity from that voxel is then applied to the deformed template image voxel (see Figure 3.5).

A special case occurs for medical imaging sensors that compute image intensity based on the density of the biological tissue under consideration (CT, ultrasound, etc.). For these types of images, Mapper3D can adjust the intensity of the voxel in the deformed template image by utilizing the change in volume of the corresponding finite element in the deformed finite element mesh.

In addition to allowing direct visualization of the deformed template following registration, this custom software allows segmentation and classification of information computed on the template image to be accurately applied to the target image. Versions of this software have been utilized heavily in the Musculoskeletal

Research Labs at the University of Utah and were used to report results in several publications [4], [5], [11], [17], [19], [22-25].

Ports to Other Operating Systems

In order to take advantage of more efficient hardware solutions, the Warping code (and the tools described above) has been successfully ported to Compaq Alpha (Tru64 Unix) and x86 Linux (Redhat 8.0) platforms. The Compaq Alpha version of the code uses the PARDISO massively parallel, sparse matrix solver [26]. It was compiled using the native Fortran compilers for that system. SVD and FFT library functions are used from the Compaq extended math library (cmxl). The x86 Linux platform uses the PCSMS sparse matrix solvers developed by NASA [27]. It was compiled using the Portland Group compiler [28]. SVD and FFT library functions are used from the LAPACK library [29] and the GNU Scientific Library [30].

References

1. J. Hadamard, "Sur les problemes aux derivees partielles et leur signification physique," *Bull. Univ. Princeton*, vol. 13, 1902.

2. J. Hadamard, "Le probleme de cauchy et les equations aux derivees lineaires hyperboliques," *Hermann, Paris*, 1932.

3. G.E. Christensen and H.J. Johnson, "Consistent image registration," *IEEE Trans Med Imag*, vol. 20, no. 7, pp. 568-582, 2001.

4. A.E. Bowden, R.D. Rabbitt, and J.A. Weiss, "Stress and strain in the human distal phalanx under indentation," *Proc. BMES/EMBS Conf., Atlanta, GA*, 1999.

5. A.E. Bowden, R.D. Rabbitt, J.A. Weiss, and B.N. Maker, "Anatomical registration and segmentation by warping template finite element models," *Proc. SPIE*, vol. 3254, pp. 469-476, 1998.

6. A. Klemencic, S. Kovacic, and F. Pernus, "Automated segmentation of muscle fiber images using active contour models," *Cytometry*, vol. 32, pp. 317-326, 1998.

7. R.D. Rabbitt, J.A. Weiss, G.E. Christensen, and M.I. Miller, "Mapping of hyperelastic deformable templates," *Proc. SPIE*, vol. 252, pp. 252-265, 1995.

8. J.A. Weiss, R.D. Rabbitt, and B.N. Maker, "Use of image data to regularize ill-posed problems in solid mechanics " *Int. J. Numer. Methods Engng.*, submitted for publication.

9. B. Maker, R. Ferencz, and J. Hallquist, "NIKE3D a nonlinear implicit three-dimensional finite element code for solid and structural mechanics," *UC - Lawrence Livermore National Laboratory Report*, vol. UCRL-MA-105268 rev 1, 1995.

10. R. Dale-Jones and T. Tjahjadi, "Study and modification of the local histogram equalization algorithm," *Pattern Recognit.*, vol. 26, no. 9, pp. 1373-1381, 1993.

11. A.E. Bowden, R.D. Rabbitt, J.A. Weiss, and B.N. Maker, "Use of medical image data to compute strain fields in a spinal disc," *Proc. ASME Bioeng. Conf.*, vol. BED-35, pp. 191-192, 1997.

12. C. Jordan, "Mémoire sur les formes bilinéaires," *Journal de Mathématiques Pures et Appliquées, Deuxième Série*, vol. 19, pp. 35-54, 1874.

13. C. Jordan, "Sur la réduction des formes bilinéaires," *Comptes Rendus de l'Académie des Sciences, Paris*, vol. 78, pp. 614-617, 1874.

14. E. Beltrami, "Sulle funzioni bileari," *Giornale di Matematiche ad Uso degli Studenti Delle Universita*, vol. 11, pp. 98-106, 1873.

15. P.C. Hansen, "Rank-deficient and discrete ill-posed problems: Numerical aspects of linear inversion," Siam. 1997. 247.

16. "Cray-1 computer systems - library reference manual ": SR-0014. 4(51)-4(52)

17. A.I. Veress, J.A. Weiss, R.J. Gillies, A.E. Bowden, J.-P. Galons, and R.D. Rabbitt, "Quantification of changes in mouse brain morphology using MRI and hyperelastic warping," *IEEE Trans. Med. Imaging*, to be published.

18. J.A. Weiss, A.I. Veress, A.E. Bowden, R.D. Rabbitt, R.J. Gillies, J.-P. Galons, and J. Guo, "Local measurements of changes in shape and volume between serial volumetric medical images: Application to niemann-pick type c disease

progression.," *Center for High Performance Computing News, University of Utah*, vol. 12, no. 3, pp. 1-3, 2001.

19. A.E. Bowden, R.D. Rabbitt, and J.A. Weiss, "Warping template finite element models into alignment with subject specific image data," *BED*, vol. 39, pp. 289-290, 1998.

20. K.-J. Bathe, *Finite Element Procedures*, New Jersey: Prentice-Hall. 1996.

21. W. Schroeder, K. Martin, and B. Lorensen, *The Visualization Toolkit, an Object-Oriented Approach to 3D Graphics*, 2nd ed., Upper Saddle River, NJ: Prentice Hall. 1998. 645.

22. R.D. Rabbitt, A.E. Bowden, and J.A. Weiss, "Tracking nonlinear soft tissue strain using 3D medical image data and the finite element method," in *NIH Biomedical Imaging Symposium, "Visualizing the Future of Biology and Medicine" on the NIH campus*, June 25-26, 1999.

23. A. Veress, J. Weiss, G. Gullberg, G. Vince, and R. Rabbitt. "Validation for the determination of strain and displacement fields in coronary arteries imaged by intravascular ultrasound." in *ASME BED Conf.,* 2001, Snowbird, UT.

24. A.I. Veress, J.A. Weiss, G.J. Klein, and G.T. Gullberg. "Quantification of 3d left ventricular deformation using hyperelastic warping: Comparisons between MRI and pet imaging". in *Computers in Cardiology*, 2002, Memphis, TN.

25. J.A. Weiss, R.D. Rabbitt, and A.E. Bowden, "Incorporation of medical image data in finite element models to track strain in soft tissues," *SPIE Biomed. Optics Symp. BiOS98*, vol. 3254, pp. 477-484, 1998.

26. O. Schenk, K. Gartner, and W. Fichtner, "Efficient sparse LU factorization with left-looking strategy on shared memory multiprocessors," *BIT*, vol. 40, no. 1, pp. 158-176, 2000.

27. C.J. Reddy, *User's manual for PCSMS (parallel complex sparse matrix solver),* 2000, NASA: Hampton, VA, p. 17.

28. *Pgi Workstation User's Guide*, STMicroelectronics, Inc., T.P.G.C. Technology, 2001.

29. *Lapack users' Guide (Third Edition)*, SIAM. 1999.

30. M. Galassi, J. Davies, J. Theiler, B. Gough, G. Jungman, M. Booth, and F. Rossi, *Gnu scientific library reference manual*, 2002.

CHAPTER 4

A CONTINUUM MECHANICS BASED DEFORMABLE TEMPLATE REGISTRATION METHOD: WARPING

Introduction

In 1995, Rabbitt and Weiss first presented a method for using the fundamental principles of continuum mechanics to guide deformable template based image registration [1]. The method, known as Warping, possesses several desirable characteristics. The general approach does not require the definition of landmarks, fiducials or surfaces, although it can accommodate these if available. Perhaps most significantly, Warping is formulated to naturally accommodate accurate stress and strain field computation during nonlinear material deformations, which are typical of many registration problems. Additionally, the method is diffeomorphic, in that one-to-one correspondence of differential lines, areas, and volumes is guaranteed between the registered images.

During the course of the research described in this dissertation, considerable effort has been exerted to validate Warping and extend its application. To this end, several techniques have been developed for regularization and evaluation of practical image registration problems. The purpose of this chapter is to demonstrate the application of Warping to a series of both simulated and real image registration

problems. Solution of these problems has been facilitated by development of the regularization tools described in Chapter 3 of this work.

The Warping examples presented in this chapter can be classified into three general categories: strain tracking, image segmentation and registration, and semi-automatic hexahedral mesh generation. Strain tracking results are provided for tip deflection of a cantilever beam, compression of a circular billet, indentation of a human distal phalanx, compression of a human spinal disc, and deflection of a mouse tectorial membrane. Segmentation and registration results are provided for a macaque neuroanatomy. Warping was also used to automatically generate a subject-specific hexahedral FE mesh of the human femur.

Methods

Mathematical Basis

Only a descriptive outline of the mathematical basis of the method is presented here. For a more thorough treatment of the derivation, please refer to Appendix A (or reference [1-3]). Standard notation from finite deformation theory is employed [4], [5]. In general, lowercase letters refer to quantities associated with the spatial (current) configuration. Uppercase letters denote quantities associated with the material (reference) configuration. Vector and tensor fields are presented in boldface italic type.

A deformation map $\boldsymbol{\varphi}$ was defined that related a reference (template) configuration with material coordinates $\boldsymbol{X}$ to a target configuration with mapped material coordinates $\boldsymbol{x}$.

$$\boldsymbol{\varphi}(\boldsymbol{X}) = \boldsymbol{x} \tag{4.1}$$

A suitable large-deformation material model (e.g., hyperelastic) was used such that the strain energy density function $W(\boldsymbol{X}, \boldsymbol{C}(\boldsymbol{\varphi}))$ was defined, where $\boldsymbol{C}(\boldsymbol{\varphi})$ is the right Cauchy strain tensor [6]. In addition to the strain energy density function, an image-based energy density function $U(\boldsymbol{X}, \boldsymbol{\varphi})$ was used to relate spatial information from the template to the target data [1], [3], [7]. This spatial information was obtained by mathematically interrogating the template and target anatomies using medical imaging sensors. The image energy density function penalized all configurations of the template that were in conflict with the target image data. Both energy terms were incorporated into a combined energy density functional:

$$E(\boldsymbol{\varphi}) = \int_{\beta} W(\boldsymbol{X}, \boldsymbol{C}(\boldsymbol{\varphi}))d\boldsymbol{V} - \int_{\beta} U(\boldsymbol{X}, \boldsymbol{\varphi})d\boldsymbol{V}\,, \tag{4.2}$$

which was used to derive the weak form Euler-Lagrange equations. The domain of the template space was discretized; and the template image data was interpolated onto the corresponding discretized version of the template model. The FE method was used to iteratively deform the template model into alignment with the target image data, while simultaneously minimizing the internal strain energy of the model. When solved using the penalty method [8], this is equivalent to a Bayesian approach [9], where W defines the Gibbs form of the prior probability and U defines the likelihood.

Implementation

Solution of the problem was divided into three phases: preprocessing, processing, and postprocessing. In the preprocessing phase, a geometric model was

constructed, boundary conditions were specified, and material properties were assigned. If needed, preliminary image regularization was applied at this phase of the analysis.

First, a geometric model was constructed to span the region of interest (ROI) in the template image. For all of the example problems presented in this chapter, the geometric models were constructed using the commercial FE preprocessor TrueGrid (XYZ Software, Livermore CA). The software is an extremely robust interactive hexahedral mesh generator, and allows parametric definition of mesh characteristics and applied boundary conditions. TrueGrid uses a projection technique for aligning nodes of the FE mesh along imported curves and surfaces. The software also supports various methods of automatic mesh relaxation and evaluation.

In general, the template model was sampled more sparsely than the image data. In some cases, the model was constructed to directly correspond to individual anatomical structures represented in the image data; in others, the model covered the entire domain of the template image data. For registration problems where accurate stress calculations were required, it was important to use subject-specific meshes in order to apply appropriate material parameters to the relevant anatomical structures as represented in the template model. Image data were interpolated over the domain of each element to generate a continuum representation of the "image field" in the reference configuration. The evolution of the image field was a function of the deformation and the material mapping.

Due to differences in imaging scanner settings, intersubject anatomical variation, and other sources of error, it was sometimes necessary to perform various

image processing operations on the image data prior to registration. For instance, in some cases it was necessary to histogram equalize the template and target images to correct for differences between scanners and data collection techniques. This was done with either the histogram stretching technique or singular value replacement technique as described in Chapter 3. Because the image data were usually acquired at a finer resolution than that of the computational mesh, often the image data were downsampled. The downsampling was governed by the Nyquist frequency corresponding to the nodal spacing of the template mesh and was obtained by convolution of the image data with a Gaussian kernel of appropriate dimension (reference Chapter 3, Eqs. 3.13 - 3.15).

During the processing phase of registration, the combined energy functional (equation 4.2) was minimized using the nonlinear FE code NIKE3D [10]. NIKE3D is a large deformation, implicit FE solver developed and maintained by Lawrence Livermore National Lab. Implementation of the Warping algorithms into such a well-developed FE package allowed for broad variation in both applied boundary conditions and material constitutive parameters, which were used to guide the registration process. For example, in some subject-specific registration problems, contact conditions can be important. It also allowed independence of the computational mesh from the spatial discretization of the image data. This independence was important for reduction of the computational size of the geometrical model and in cases where the region of interest did not include the entire image data set.

Template and target images were interpolated from voxel coordinates to the FE model to define continuous mathematical representations of the data. The interpolated images were updated as the material deformed through the spatially fixed image coordinates. Differences between intensity of the target and template images, as well as their gradients, contributed a spatially dependent body force that drives the registration process. These differences also contributed to the tangent stiffness in the FE implementation (reference Appendix A, Eqs. A.15 – A.18). It was also during the processing stage of the registration that the regularization techniques discussed in Chapter 3 of this dissertation were used to avoid local minima in the combined energy functional. Some of the techniques used were: dynamic spatial filtering, rezoning, and sequential image registration.

After the processing phase of Warping, field variables, including displacement, relative volume, and strain, were viewed using the FE postprocessor GRIZ [11]. Additional custom postprocessing software was written to output the deformed template as an image data set (reference Chapter 3: Mapper3D). This required interpolation of Lagrangian nodal displacements in order to generate pixel locations and intensities within the Eulerian image-based coordinate frame. If the registration were perfect, the mapped template image would exactly align with the target image. Thus, visual inspection of the mapped template image provided a qualitative means to assess the registration. Global quantitative measures such as subtraction and sum of the squared difference (SSD) were also used to demonstrate image alignment [3]. Other quantitative means of assessing image registration are presented and discussed in Chapters 5 and 6 of this dissertation.

Illustrative Examples

Mechanics Validation Study: Compressed Circular Billet

The first example problem was a homogeneous circular billet compressed between two parallel plates. The problem was highly nonlinear in that it accounts for both large strain as well as contact between the billet and the parallel plates during the deformation. Hypoelastic material properties were assigned to the billet (E= 1MPa, ν=0.48). A FE mesh was constructed to model 1/4 of the billet in the reference configuration with symmetry boundary conditions applied to the appropriate surfaces. The objective of this analysis was to verify the ability of the Warping code to accurately predict stress and strain for a simulated example problem with well-defined material properties and known loading conditions.

For the forward simulation, a prescribed displacement condition was applied to the parallel plates so as to impose 50% axial compression on the billet. Simple black and white Template and target images were generated from the forward solution using images of the FE mesh in the reference and deformed configurations (without mesh lines).

To validate the warping algorithm, the boundary conditions and the applied loads were removed, and the image terms were added to the energy functional (Eq. 4.2). The problem was then re-run with the two images driving the process. An augmented Lagrangian approach was used to enforce correspondence between the template and target images. As with all problems presented in this chapter, this example problem was solved using a static analysis. For this simulated registration problem, no additional regularization techniques were needed.

Mechanics Validation Study: Large Deformation Cantilever Beam

A classic problem in solid mechanics is the cantilever beam. For this analysis, a three-material hypoelastic beam was used. The objective was to verify the ability of the Warping code to accurately predict stress and strain for a simulated example problem with well-defined material properties and known loading conditions. In contrast to the compressed billet problem described previously, the computed deformation was nonhomogenous in nature and interior stress and strain fields cannot easily be determined from border information alone. Young's Modulus values for the top, middle and bottom layers respectively were specified as: E = 20GPa, E = 20MPa, E = 2GPa. Poisson's ratio was set at 0.3 for all layers of the beam. The beam was modeled in a plane strain configuration with the left end of the beam constrained from motion. A FE mesh was constructed to directly correspond with the material layers of the beam.

First a forward mechanics problem was solved, with a prescribed loading applied to the top node on the right end of the beam (50kPa $\downarrow$). Unlike the compressed billet problem described previously, the nonhomogenous nature of the cantilever beam required adequate image textural content to effectively predict stress. To this end, arbitrary textured image data were generated to correspond with the undeformed configuration of the beam. This image data served as the template image for the image registration problem. The target image for the registration problem was generated using Mapper3D by applying the deformation field computed from the forward solution to the template image data.

Once the forward solution was complete, the prescribed loading conditions were removed and the problem was solved using Warping to drive the deformation. Additional regularization was not necessary for this simulated problem. Following registration of the image data, the stress fields from the forward and Warping problems were compared in order to validate the solution process.

Determining Strain Fields in a Human Spinal Disc during Compression

The human vertebral disc is a complex combination of materials including collagen, water, and a proteoglycan matrix. Material characterization and strain measurement are extremely difficult for the disc. Using a nonmagnetic compression frame and a MR scanner, MR images of a L2-L3 motion segment were obtained before (template) and after (target) application of a compressive load (image data supplied by Chiu et al. [12]). The objective of the analysis was to compute the strain field present in the spinal disc during the deformation from the supplied image data.

The template image was manually segmented to obtain contours corresponding to the bone and disc. These contours were used to generate a FE mesh corresponding to the specific anatomy of the subject. Image data were filtered at the spatial Nyquist frequency (6 pixels) of the FE mesh to avoid aliasing. Representative hypoelastic material properties were estimated from the literature [13]. Differences between the template and target images described the only input force driving the deformation of the disc and bone. A penalty method was used to apply the registration force. As the warping code registered the two images, strains developed in the spinal disc. Following registration, the computed deformation field was applied to the template

image using Mapper3D, in order to obtain the deformed template image following registration.

Determining Stress and Strain Fields in Human Distal Phalanx During Indentation

High-resolution MR data from the distal phalanx were collected in order to estimate material response of the human fingerpad to indentation. A 4.7 Tesla magnet and a RARE sequence were used to obtain high-resolution (125 x 125μm) MR images of the cross-section of a healthy human male fingerpad [14]. The nail of the distal phalanx of the subject was rigidly constrained using a specially constructed, non-magnetic frame. Mechanical indentation of 1-2 mm was applied to the fingerpad with a nonmagnetic, rectangular indenter. Constant indentation was maintained by mounting the indenter to the constraint frame. The target image was obtained during a maintained indentation of the fingerpad. The objective of the analysis was to examine stress and strain fields in the fingerpad under the described loading conditions.

In order to examine the stress developed in the fingerpad due to the applied indentation, it was necessary to develop a template model that reflected the specific anatomy underlying the images. A FE mesh was constructed based on a manual segmentation of the undeformed template image. This mesh was divided into three regions based on tissue type. Hypoelastic material properties were assigned from the literature [15] as follows: bone ($E = 15\times10^8$ Pa, $\nu = 0.48$), dermis ($E = 15\times10^4$ Pa, $\nu = 0.48$), other tissue ($E = 15\times10^3$ Pa, $\nu = 0.48$). No externally applied loads or boundary conditions were imposed on the model; thus deformation of the mesh was exclusively due to the image registration process. Dynamic spatial filtering was applied to both

the template and target images during registration. An augmented Lagrangian method was used to enforce correspondence between the template and target images. Following registration, the computed deformation field was interpolated from the template FE model to the original spatial grid of the template data using Mapper3D.

Determining Strain Fields in the Mouse Tectorial Membrane

Abnet and Freeman isolated tectorial membranes from the mouse cochlea and obtained a series of high-resolution video microscopy images [16]. The cochlea was isolated and placed in an artificial endolymph solution. An apical section of the membrane was affixed to the bottom of a cylindrical glass chamber using a tissue adhesive. A single magnetizable bead 20 μm in diameter was fixed to the free surface of the membrane with tissue adhesive. Polystyrene beads 1 to 2 μm in diameter were dispersed along the surface to serve as motion markers.

The preparation was placed in a magnetic field created by two electromagnets. A computer was used to control the waveform and the magnitude of the current applied to the magnets. The method produced up to 1 μN of force for frequencies from DC to more than 100Hz. The snapshot images were taken with a scientific grade CCD camera and light microscope with strobed illumination. The voxel size in the obtained images was about 0.2255 μm.

Tectorial membrane is composed of a mucopolysaccharide matrix with aligned collagen fibers. Hypoelastic property data were used in the problem ($E=1.2$ Pa, $\nu=0.2$). The testing situation seemed to warrant the use of a low Poisson's ratio to allow for water extrusion from the matrix. Because of the significant anisotropic impact of the collagen fibers in the membrane, the applied FE mesh was dense (one

element per pixel). This approach avoided aliasing while fully utilizing the texture of the membrane as reflected in the image data. At such a high mesh resolution, however, the computational cost was greatly increased. A subsection of the membrane was examined. The histogram of the target image was adjusted to match that of the template image using histogram stretching. During the registration process, the bottom surface of the 3D mesh was fixed in all direction. No other external boundary conditions were applied except the position dependent body force generated from the image data. Following registration, the computed deformation field was interpolated from the template FE model to the original spatial grid of the template data using Mapper3D. The objective of this problem was to examine fiber-matrix interaction in the membrane during the described deformation. The problem also demonstrated the ability of Warping to distinguish between rigid body motion and deformation in the membrane.

Intersubject Registration of Macaque Neuroanatomies

One of the most common applications of image registration techniques is neuroanatomical segmentation and registration. The complexity of brain structure presents numerous challenges for deformable template based registration techniques. Neuroanatomical structure varies widely between subjects; and as a consequence, most of these problems display numerous local minima during image registration.

The digital images of the macaque neuroanatomy were generated by block microtome cryosectioning and CCD digitization of 100-μm sections from two macaque monkeys (images from D. VanEssen, [17]). Results appearing previously in the literature for neuroanatomical registration often use rectilinear computational grids

associated with image voxels. The present FE method allows for both rectilinear and irregular mesh structure. Two different computation mesh configurations were used: a simple regular mesh, and a mesh conforming to a lobe of grey and white matter. In both cases, the material was modeled as an elastic-plastic solid with a low Poisson's ratio ($E = 15\times10^3$ Pa, $\nu = 0.1$, $\sigma_{yield} = 15\times10^3$ Pa), allowing for both large volume changes and large shear. Deformation of the template brain slice was constrained to the plane of the image data. Dynamic Gaussian spatial filtering with a spatial frequency that varied from 30 pixels initially, to 2 pixels at final registration was used to avoid local minima during the registration process. Following registration, the computed deformation field was interpolated from the template FE model to the original spatial grid of the template data using Mapper3D.

Semi-automatic Construction of a Subject-Specific Hexahedral Mesh of the Human Femur

The Warping method can also be applied to generate subject specific geometric models, which is a problem equivalent to tissue segmentation. Two knees from male cadavers were used in this study. The fresh-frozen specimens were thawed at room temperature overnight before dissection and were inspected for signs of previous injury or arthritis. All periarticular soft tissue was removed until only the medial collateral, lateral collateral, anterior cruciate, and posterior cruciate ligaments and medial and lateral menisci remained intact. During all dissection and testing, the tissue was kept continuously moist with 0.9% buffered saline. All testing was completed within 5 hours during which time no noticeable changes in the tissue were observed.

After dissection, a volumetric CT image dataset was obtained with the knee at 0° of flexion (SOMATOM Plus4; Siemens, Munich, Germany). The slices were collected with a 1.0 mm slice thickness (12 bit resolution, 512x512 image matrix, FOV=140x140 mm). The surface geometries of the femur of each knee were obtained from the CT data. Polygonal surfaces of the femur were extracted using marching cubes [18] with decimation [19]. Surfaces were imported into a FE pre-processing program (TrueGrid®, XYZ Scientific, Livermore, CA) and block-structured, hexahedral finite element meshes were constructed for each structure. During registration, no other external boundary conditions were applied, except the position dependent body force generated from the image data.

Results

Mechanics Validation Study: Compressed Circular Billet

Figure 4.1 shows the results from a mechanics validation study of a circular billet. Panel A shows the theoretical test setup. The symmetry planes of the problem are indicated with dotted lines. Panel B shows the discretized template FE model of the symmetric section. Panels C and D show the template and target images, respectively. The deformed template image following registration is shown in panel E. Global alignment of the registered template image with the target image is shown by subtraction (Panel F), and squared difference (Panel G) images. The corresponding numerical values for these measures have been normalized by the size of the images and the magnitude of the maximum possible intensity value: Subtraction (9.31×10^{-4}), SSD (5.18×10^{-1}). Panels H and I show isocontours of the predicted Von Mises stress field from the forward problem and the Warping problem, respectively. The displayed

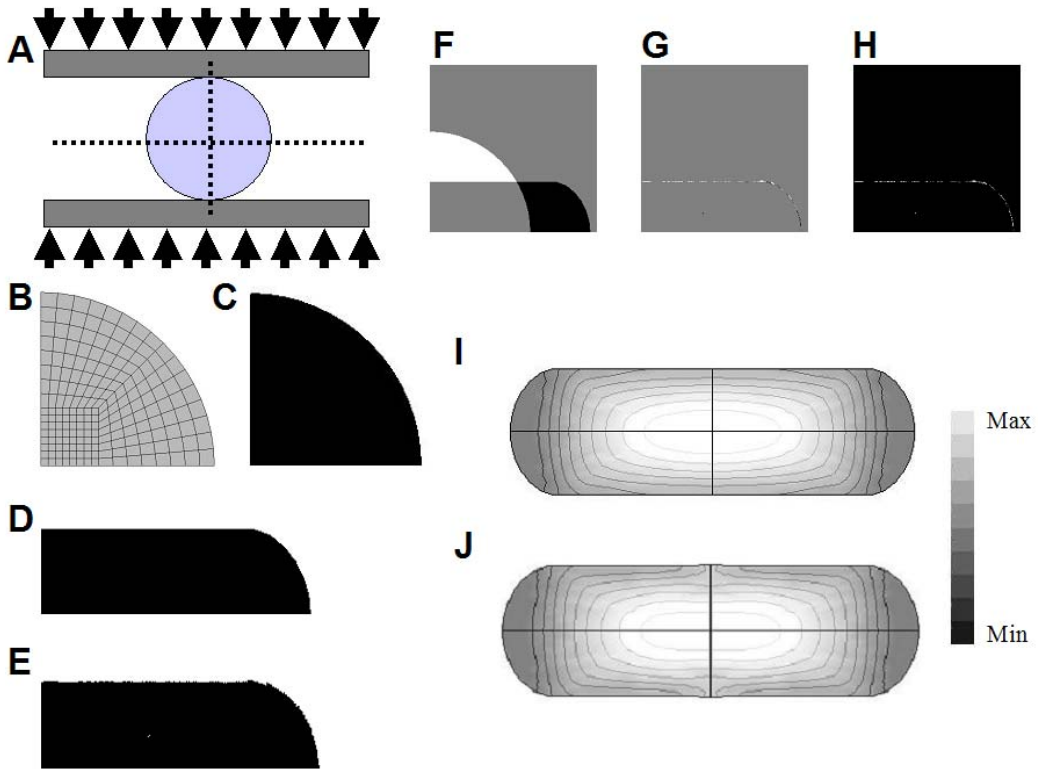

Figure 4.1. Compression of a circular billet. Panel A shows the theoretical test setup. Panel B shows the ¼ symmetry FE mesh. Panels C, D, and E show the template, target, and deformed template images, respectively. Accuracy of registration is shown by subtraction (Panel F) and squared difference (Panel G) images. Von Mises stress results from the forward (Panel H) and Warping (Panel I) problems are shown on the same scale.

results were mirrored about the symmetry planes. Results demonstrate excellent correspondence between the forward and Warping stress fields. From a computational standpoint, the problem is well-defined, since the interior stresses are completely defined by the boundary deformation.

Mechanics Validation Study: Large Deformation Cantilever Beam

Figure 4.2 shows results from another validation study, deformation of a non-homogenous cantilever beam. Panel A shows the theoretical test setup. A three layer

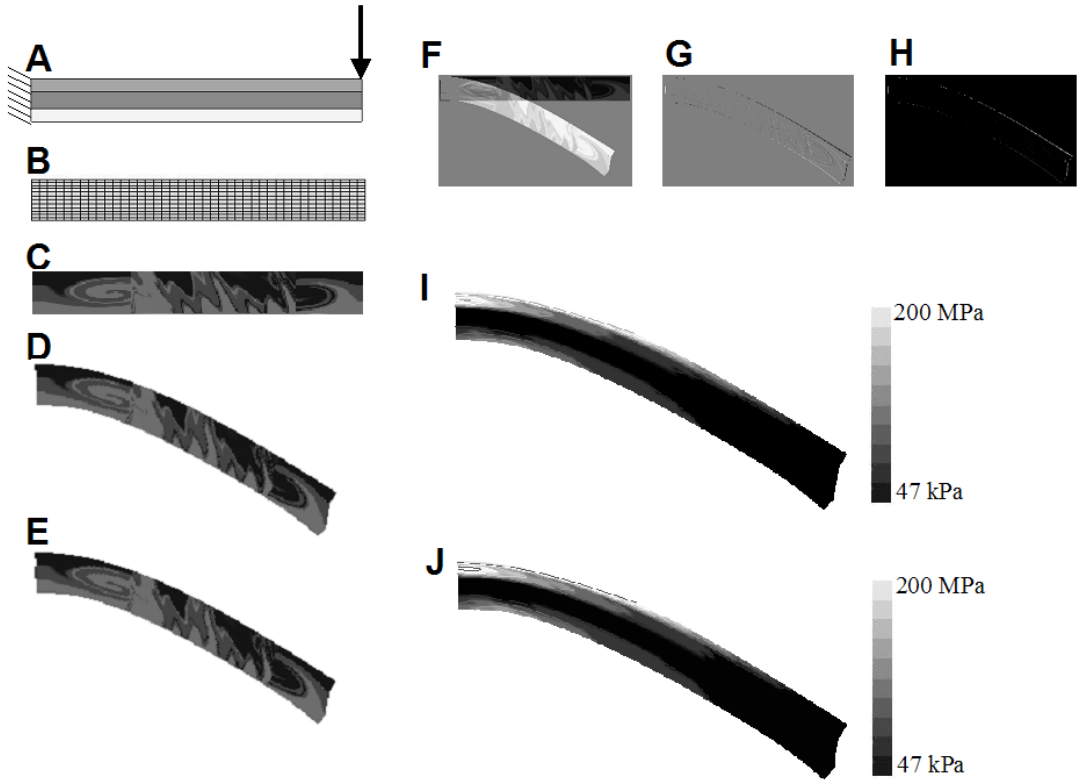

Figure 4.2. Mechanics validation of a nonhomogenous cantilever beam. Panel A shows the theoretical test setup. Panel B shows the discretized template model. Panels C, D, and E show the template, target, and deformed template images, respectively. Accuracy of registration is shown by subtraction (Panel F) and squared difference (Panel G) images. Panel H shows Von Mises stress results as predicted from the forward FE simulation. Panel I shows the Von Mises stress predictions from the Warping problem.

beam was built in on the left side. A large nodal load is applied at the top right of the beam. Panel B shows the discretized template model. Panels C and D show the template and target images, respectively. The deformed template image following registration is shown in panel E. Global alignment of the registered template image with the target image is shown by subtraction (Panel F), and squared difference (Panel G) images. The corresponding numerical values for these measures have been normalized by the size of the images and the magnitude of the maximum possible

intensity value: Subtraction (7.89×10^{-4}), SSD (4.66×10^{-1}). Panels H and I show isocontours of the predicted Von Mises stress field from the forward problem and the Warping problem, respectively. Unlike the homogenous circular billet problem described above, a homogenous image field did not provide sufficient constraint on the problem to achieve acceptable stress field results. Additional textural information was added to the problem in order to regularize the problem and achieve the excellent correspondence in stress results between the forward and Warping problems as shown in panels H and I of Figure 4.2.

Determining Strain Fields in a Human Spinal Disc in Compression

Figure 4.3 shows results from the registration of cross-sectional MR images of the human spinal disc. Panels A, B, and C show the template, target, and registered template images, respectively. Global image alignment is shown quantitatively by the normalized squared difference image in Panel D (normalized SSD = 6.08×10^{-1}). Panel E shows the discretized template model. Panels F, G, and H show pressure, Von Mises strain, and Von Mises stress fields (respectively), as predicted by Warping. Results show pressures of up to 1.7 MPa and Von Mises strain as high as 57% within the disc. Results indicate that the compressive load applied to the bone-disc-bone segment had a large shear component.

Determining Stress and Strain Fields in Human Distal Phalanx During Indentation

The top row of Figure 4.4 provides image alignment results. Panels A and B show the original MR images taken before and during deformation (respectively).

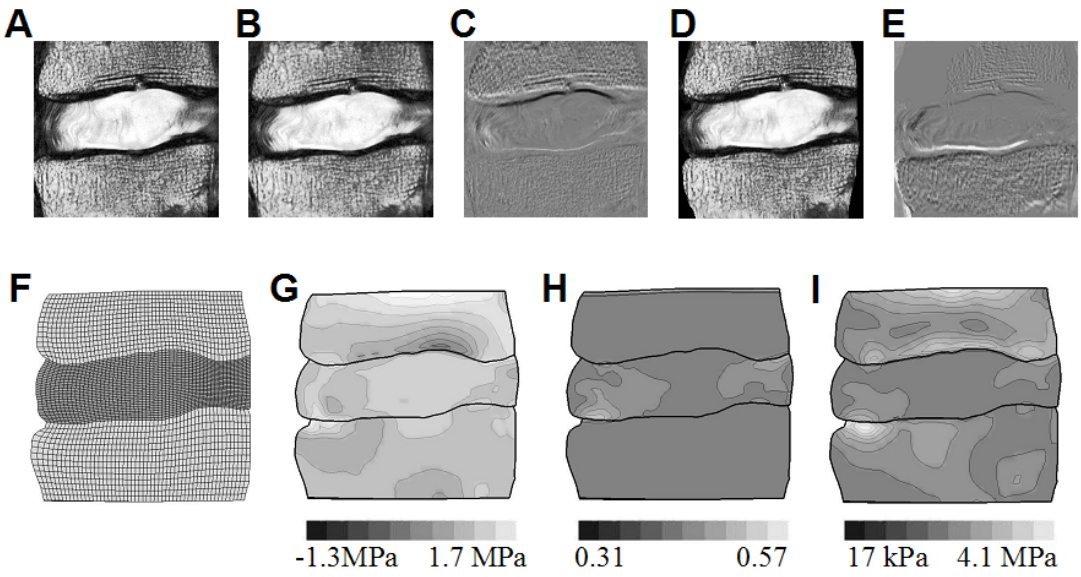

Figure 4.3. Compression of a human spinal disc. Panels A, B, and C show the template, target, and registered template images, respectively. Panel D shows SSD results for the registration. Panel E shows the discretized subject-specific template model. Panel F shows pressure results. Panels G and H show the Von Mises strain and stress fields predicted by the registration.

Panel C shows the deformed template image after alignment as obtained using Mapper3D. The normalized squared difference image from the registration is shown in Panel D (normalized SSD = 5.14×10^{-1}). Panel E shows the subject-specific FE template model used for the Warping analysis. Pressure, Von Mises strain, and Von Mises stress field results are provided in panels F, G, and H. It was apparent from the strain field results (panel G), that there was significant blood flow in the interior region of the finger during material deformation. Due to higher stiffness values however, the largest Von Mises stress values occurred in the bone and the dermal area immediately surrounding the indenter.

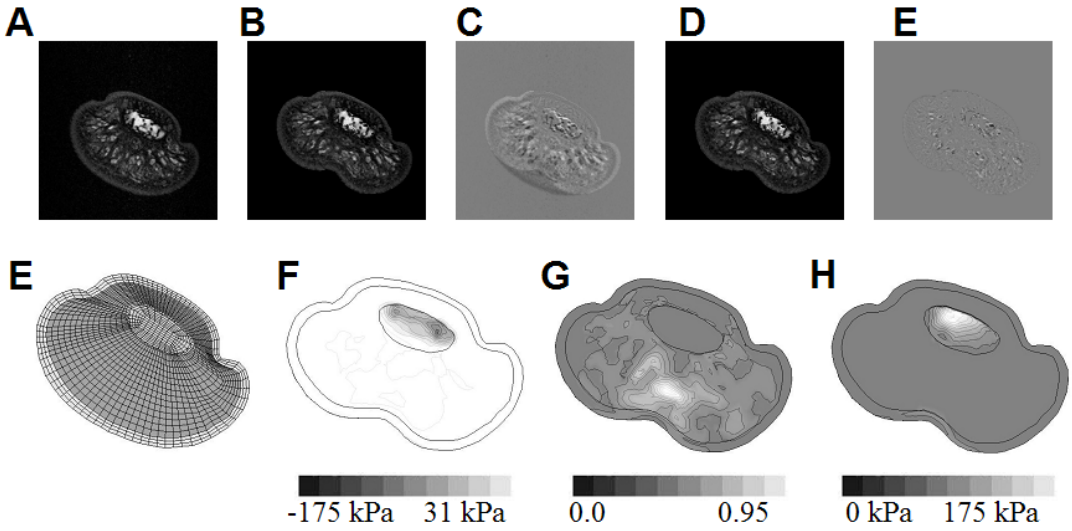

Figure 4.4. Indentation of a human fingerpad. Panels A, B, and C show the template, target, and registered template images, respectively. Panel D shows squared difference results for the registration. Panel E shows the subject-specific FE mesh used for the Warping analysis. Panels F, G, and H show pressure, Von Mises strain, and Von Mises stress fields (respectively), as predicted by Warping.

Determining Strain Fields in the Mouse Tectorial Membrane

Figure 4.5 shows registration results obtained using Warping to analyze the strain that developed in the tectorial membrane of a mouse cochlea when exposed to a sinusoidal force. Panel A shows a high-resolution image of the membrane. Only a portion of the image was analyzed as indicated by the template image in panel B. Panel C shows the corresponding portion of the target image used for the analysis. The registered template image shown in panel D was obtained using Mapper3D. The very finely discretized mesh shown in panel E was used to take advantage of the full image resolution within the analyzed section. Pressure, Von Mises strain, and Von Mises stress results are given in panels F-G, respectively. Results indicate that during results are not shown, because the differences in the final registered images were too small to view with the naked eye (SSD = 4.8×10^{-4}).

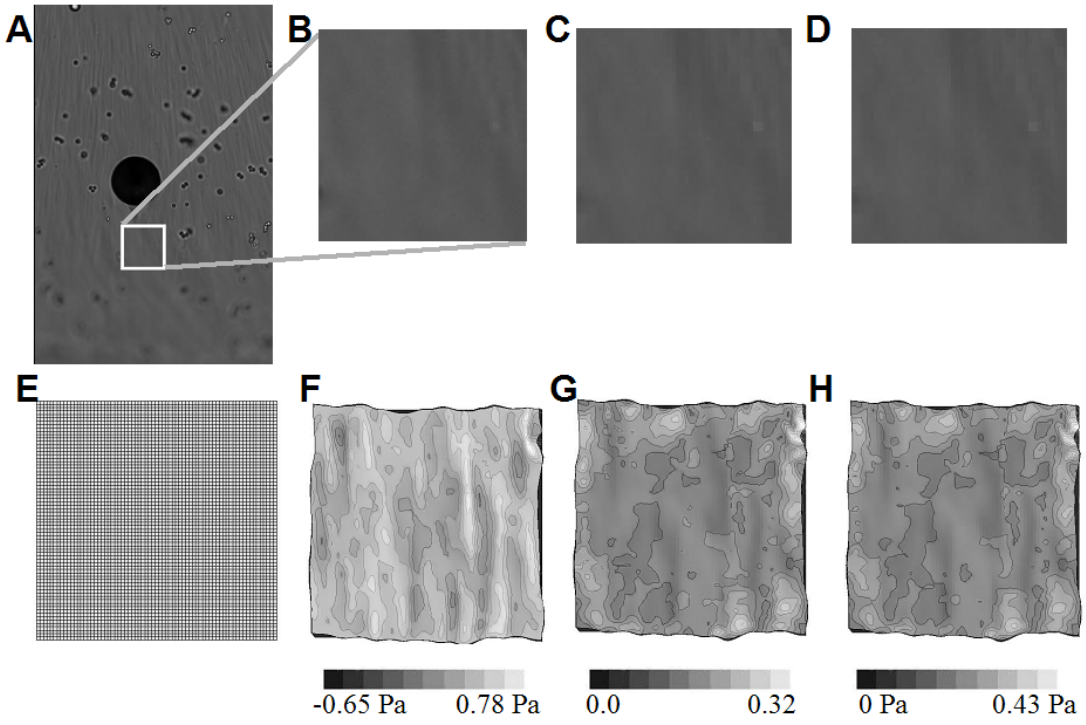

Figure 4.5. Strain prediction in the tectorial membrane of a mouse cochlea. Panel A shows the high-resolution template image used for the analysis. Panel B shows the area of the template image used for the registration problem. Panel C shows the corresponding area of the target image. Panel D shows the deformed template image following registration. The discretized template model is shown in panel E. Pressure, Von Mises strain, and Von Mises stress are shown in panels F, G, and H, respectively.

Intersubject Registration of Macaque Neuroanatomies

Figures 4.6 and 4.7 present Warping results that were obtained using the same template and target images, with different types of discretization used to generate the template model.

Rectangular Mesh

Figure 4.6 provides results for a simple rectangular mesh constructed to span the domain of the template image data shown in panel A. The target image is shown

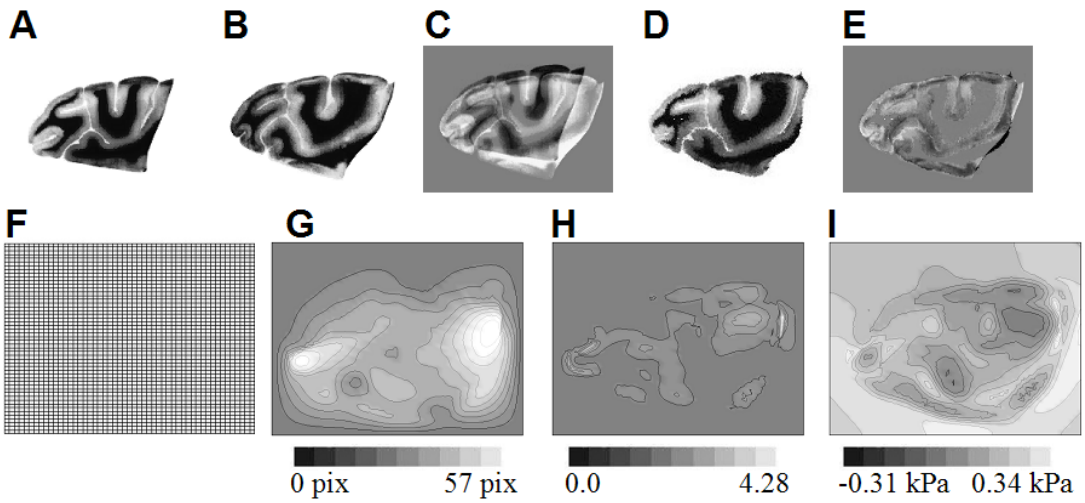

Figure 4.6. Intersubject registration of macaque neuroanatomies. Panels A, B, and C show the template, target, and registered template images, respectively. Squared difference results from the registration are shown in panel D. The discretized template model is shown in panel E. Panel F shows pressure results. Displacement magnitude, Von Mises strain, and pressure results are shown in panels G and H, respectively.

in panel B. The registered template image is shown in panel C, as obtained using Mapper3D. Registration results are quantified by the squared difference image in panel D (SSD = 6.83×10^{-1}). The discretized template model is shown in panel E. Pressure, Von Mises strain, and Von Mises stress fields are given in panels F - H, as predicted by Warping.

Lobe Mesh

Using a subject specific mesh allows a more direct automatic segmentation of the neuroanatomy. Figure 4.7 provides results for an irregular mesh constructed to span the white and grey matter between the central and rightmost sulci. The target image is shown in panel B. The registered template image is shown in panel C, as obtained using Mapper3D. Squared difference results from the registration are shown

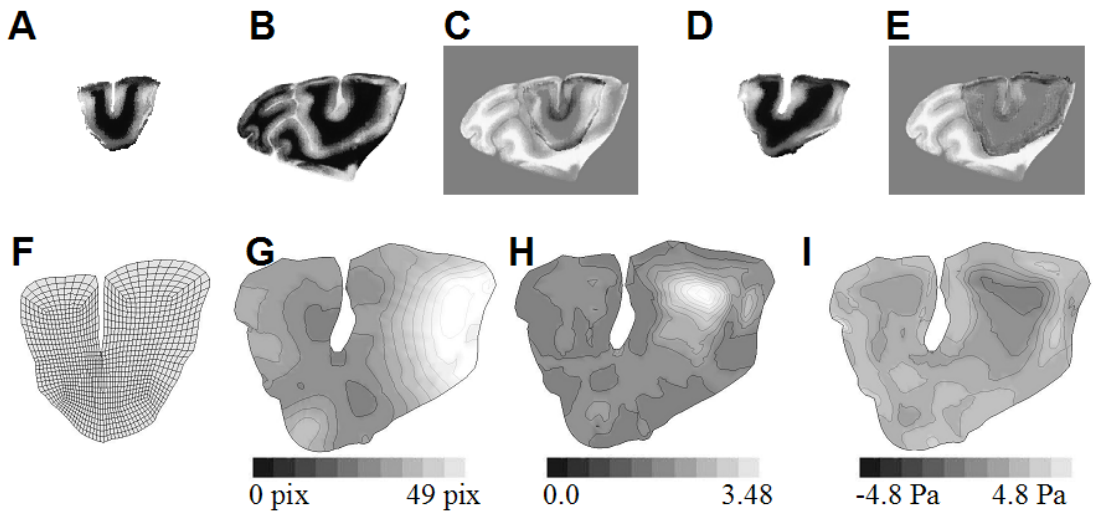

Figure 4.7. Intersubject registration of macaque brain section. Panels A, B, and C show the template, target, and registered template images, respectively. Squared difference results for the registration are shown in panel D. The discretized subject-specific template model is shown in panel E. Panel F shows pressure results. Displacement magnitude, Von Mises strain, and pressure results are shown in panels G and H, respectively.

in panel D, although the normalized SSD value (SSD = 24.21×10^{-1}) is not representative of the alignment due to relatively small domain covered by the template mesh. The discretized template model is shown in panel E. Pressure, Von Mises strain, and Von Mises stress are shown in panels F - H.

Results were computed on the geometrical model and thus are not available outside the spatial domain of the mesh. The deformed mesh aligns well with the same region of the brain in the target anatomy, illustrating automatic segmentation.

Semi-automatic Construction of a Subject-Specific Hexahedral Mesh of the Human Femur

Warping can also be applied to generate subject specific geometric models, which is a problem equivalent to tissue segmentation. This is illustrated in Figure 4.8

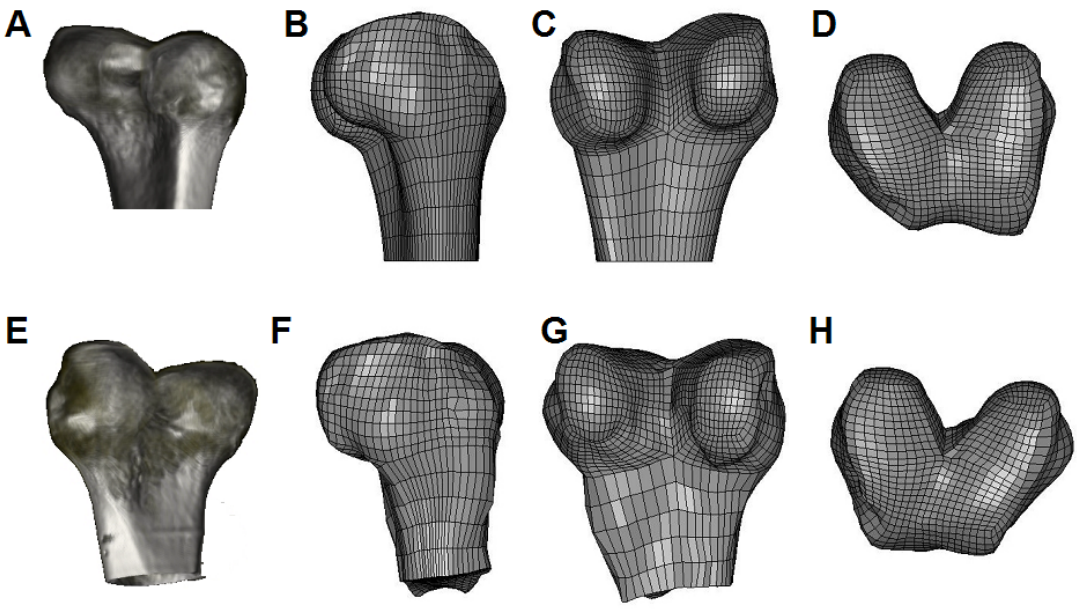

Figure 4.8. Intersubject registration of the human femur. Panels A and E show surface projections of the volumetric X-Ray CT data used as the template and target image, respectively. Panels B, C, and D, show orthogonal views of the discretized subject-specific template model before registration. Panels F, G, H, show corresponding orthogonal views of the deformed template model.

where a FE model, generated from the CT data of one human femur (template), is mapped to a second subject (target). Panels A and E show rendered views of the 3D CT data corresponding to the template and target respectively. Orthogonal views of the template FE mesh used for the registration are shown in panels B-D. Corresponding orthogonal views of the deformed template mesh are shown in panels F-H. Note the elongation and torsion induced on the mesh configuration. As a measure of mesh quality following the registration, the values of the relative Jacobians of the hexahedral elements are graphed in Table 4.1. Squared difference images are not shown due to the inadequacies of displaying 3D image data on paper, but the quantitative SSD was 0.277. As in the case of the macaque lobe mesh, the SSD

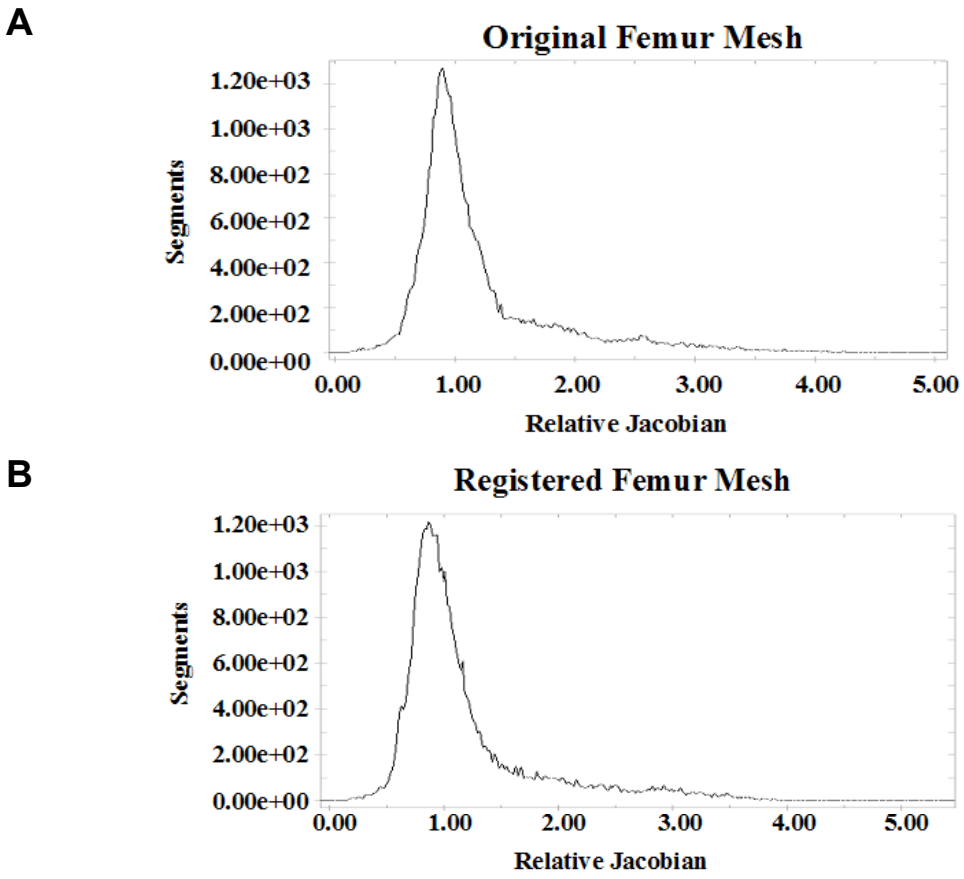

Figure 4.9. Relative Jacobian values of the femur FE mesh. Panel A shows the relative Jacobian of the original subject-specific femur mesh. Panel B shows the relative Jacobian values of the femur mesh following registration.

measure is not adequate to address the problem, due to the restricted domain of the template model.

Discussion

It should be noted that because Warping is diffeomorphic, registration can be difficult in cases where the template and target anatomies are fundamentally different. Implicit in equation 4.1 is the assumption that the target is a deformed configuration of the template. This is the case only when the template and target images are taken from the same physical material. For problems where images are taken from different

subjects, the mapping between them does not represent a physical deformation. Rather, the mapping represents the optimized configuration of the FE mesh that aligns the template and target data. Use of nonlinear continuum mechanics in the process guarantees a one-to-one mapping of differential lines, areas, and volumes between the template and its deformed configuration. This is required to ensure that anatomical structures in the template remain continuous after the deformation.

Because of the large role the image data play in the strain tracking process, we were interested in the extent to which the constitutive law actually changes the numerical results. Sensitivity of results to the material properties is dependent upon the specific problem under study. For registration problems that use images with high textural content, the image data will tend to dominate the solution. Problems with noisy or sparsely sampled images will be affected to a greater extent by the mechanics of the problem (reference Chapter 6 of the present work). In several of the presented example problems (the spinal disc, distal phalanx, tectorial membrane), we tested the sensitivity of results to variations in the material model parameters. For these problems, the computed deformation was largely insensitive to changes in the bulk moduli, due to the path independent nature of the elastic response. This insensitivity does not hold for the shear moduli, owing to the interplay between the volume ratio and strain. Due to the lack of volumetric information in two-dimensional (2D) problems, the computed strain field is sensitive to the compressibility of the material. The most physically consistent results for 2D data are therefore obtained when the material properties match actual tissue. Strain results for 3D data (such as the femur test problem) are more robust to changes in material compressibility.

Perhaps the most significant limitation to the technique is the need for an experienced FE analyst to perform the Warping analysis. With the large number of parameters that can be adjusted to guide the registration process, it is important to be able to anticipate the response of the registration process to changes in any of these parameters. Additionally, an experienced analyst can decide when it is appropriate to apply the regularization tools presented in Chapter 3 of this dissertation.

The neuroanatomical registration results illustrate the difference in segmentation results achieved by a rectangular mesh versus a mesh corresponding to the tissue geometry. The rectangular mesh achieved unacceptable results because of the presence of a local minimum in the combined energy functional (equation 4.1). Experience has shown [17], [20] that local minima are more likely to occur during 2D segmentations on rectangular grids due to competing regions in the image data. Meshing only the ROI using an irregular mesh not only avoids such phenomena, but also reduces the computational size of the problem. An additional advantage to the irregular FE mesh is the direct segmentation afforded by the deformed template image (Panel C in Figures 4.7 and 4.8).

The 3D capabilities of the present method are demonstrated in the distal femur registration. In 3D segmentations, the independence of the computational mesh from the voxel space of the image data is especially relevant. A small ROI in a data set can be extracted without the computational burden of bringing the whole image space into registration. This example further illustrates an important aspect of the present FE method. Considerable effort is required to construct structured computational meshes that accurately reflect the tissue geometry. The distal femur registration demonstrates

a convenient way to automatically generate complex computational meshes by mapping a canonical template model to conform to the anatomy of an individual subject.

The examples in this chapter also illustrate the inadequacies of the current standards in quantitative image analysis, subtraction and SSD, in dealing with subject-specific template models. When the domain of the template does not include the entire image domain, image information outside the domain cannot be interpolated to the deformed template image. More comprehensive measures of image correspondence are discussed in Chapters 5 and 6 of this dissertation.

In summary, we have shown that continuum mechanics provides an excellent constraint system for guiding anatomical warping. The registrations achieved through this technique are diffeomorphic and accommodate large changes in topology between template and target anatomies. Additionally, the technique allows proper computation of large deformation strain fields. This is especially important for biological problems where large strains are the norm, rather than the exception.

References

1. R.D. Rabbitt, J.A. Weiss, G.E. Christensen, and M.I. Miller, "Mapping of hyperelastic deformable templates," *Proc. SPIE*, vol. 252, pp. 252-265, 1995.

2. J.A. Weiss, R.D. Rabbitt, and A.E. Bowden, "Incorporation of medical image data in finite element models to track strain in soft tissues," *SPIE Biomed. Optics Symp. BiOS98*, vol. 3254, pp. 477-484, 1998.

3. A.I. Veress, J.A. Weiss, R.J. Gillies, A.E. Bowden, J.P. Galons, and R.D. Rabbitt, "Quantification of changes in mouse brain morphology using MRI and hyperelastic warping," *IEEE Trans. Med. Imaging*, to appear, 2003.

4. J.E. Marsden and T.J.R. Hughes, *Mathematical Foundations of Elasticity,* Minneola, NY: Dover,1994.

5. J.C. Simo, "A framework for finite strain elastoplasticity based on maximum dissipation and the multiplicative decomposition: Part I continuum formulation," *Comp. Meth. Appl. Mech. Engineering*, vol. 66, pp. 199-219, 1988.

6. A.J.M. Spencer, *Continuum Mechanics,* Essex England: Longman Scientific & Technical, 1980.

7. G.E. Christensen, R.D. Rabbitt, and M.I. Miller, "Deformable templates using large deformation kinematics," *IEEE Trans. Image Processing*, vol. 5, no. 10, pp. 1435-1447, 1996.

8. K.-J. Bathe, *Finite Element Procedures,* New Jersey: Prentice-Hall, 1996.

9. J.C. Gee and P.D. Peralta, "Continuum models for bayesian image matching," in *Maximum entropy and bayesian methods*, K.M. Hanson and R.N. Silver, ed. Kluwer Academic Publishers: Dordrecht, 1996, pp. 109-116.

10. B. Maker, R. Ferencz, and J. Hallquist, "NIKE3D a nonlinear implicit three-dimensional finite element code for solid and structural mechanics," UC - Lawrence Livermore National Laboratory Report, Livermore, CA, UCRL-MA-105268 rev 1, 1995.

11. D. Dovey and T.E. Spelce, "GRIZ finite element analysis results visualization for unstructured grids," UC - Lawrence Livermore National Laboratory Report, Livermore, CA, vol. UCRL-MA-115696, 1993.

12. E.J. Chiu, J.C. Lotz, and S. Majumdar, "High resolution magnetic resonance imaging of the human intervertebral disc with compression" *Trans. 41st Orthopaedic Res. Soc.,* vol. 20(2) p. 292, 1995.

13. Y.K. Liu, G. Ray, and C. Hirsch, "The resistance of the lumbar spine to direct shear" *Orthopadic Clin. North Am.,* vol. 16(1) pp. 33-47, 1975.

14. K.J. Voss and M.A. Srinivasan, "Investigation of the internal geometry and mechanics of the human fingertip, in vivo, using magnetic resonance imaging,″ Touch Lab Report, Cambridge, MA, MIT RLE TR-622, 1998.

15. R.J. Gulati and M.A. Srinivasan, "Determination of mechanical properties of the human fingerpad, in vivo, using a tactile stimulator,″ Touch Lab Report, Cambridge, MA, MIT RLE TR-605, 1996, p. 265.

16. C.C. Abnet and D.M. Freeman, "Deformations of the isolated mouse tectorial membrane produced by oscillatory forces," *Hearing Research*, vol. 144, no. 1-2, pp. 29-46, 2000.

17. A.E. Bowden, R.D. Rabbitt, J.A. Weiss, and B.N. Maker, "Anatomical registration and segmentation by warping template finite element models," *Proc. SPIE*, vol. 3254, pp. 469-476, 1998.

18. W.E. Lorensen and H.E. Cline, "Marching cubes: A high resolution 3d surface construction algorithm," *Comput. Graphics,* vol. 21 no. 4 pp. 163-169, 1987.

19. W. Schroeder, J. Zarge, and W.E. Lorensen, "Decimation of triangle meshes" *Comput. Graphics (ACM),* vol. 26, no. 2, pp. 65-70, 1992.

20. A.E. Bowden, R.D. Rabbitt, and J.A. Weiss, "Warping template finite element models into alignment with subject specific image data," *BED*, vol. 39, pp. 289-290, 1998.

CHAPTER 5

ASSESSMENT OF DEFORMABLE IMAGE REGISTRATION USING 3D SINGULAR VALUE DECOMPOSITION

Abstract

The primary goal of this work was to develop a quantitative technique to evaluate the success of 3D deformable image registration. The technique is based on singular value decomposition (SVD) and provides an objective method to compare the topology of a deformed Template image with that of a Target image. A 3D extension of the standard singular value decomposition was posed and applied. The technique provides: 1) A hierarchical method to quantify image registration, 2) a method to assess topological mismatch between image datasets, and 3) a means to rank image registration solutions to distinguish local from global minima. Results demonstrate application of the technique using magnetic resonance images of the heart and human distal phalanx, as well as optical images of primate brain cryosections. Results indicate the technique may also be appropriate for a priori identification of local minima.

Introduction

Over the last two decades, a substantial body of research has been dedicated to medical image registration -- the process of aligning anatomical features present in a

Template image data set (a.k.a. reference, textbook, atlas) with those present in a specific *Target* image data set (subject) [1-3]. This process is an essential step in many applications, including quantitative image comparison, segmentation, strain measurement, atlas construction, image fusion, motion correction, and image-guided surgery

Several techniques have been brought to bear on this problem including statistical pattern recognition [4-7], landmark/marker-based transformations [8], principal axis registration [9], [10], and high-dimensional deformable templates [11-18]. A common requirement for all of these techniques is the quantification of the quality of image registration. Previous efforts to quantify the success of image registration have focused on global comparisons of the mapped Template image following registration with the Target. Examples include image subtraction [16], misfit calculation (i.e., sum of the squared differences) [19], histogram comparisons [20], wavelet transform comparisons [21], and mutual information [22]. Recently, the Vista Project [23], the Retrospective Registration Evaluation Project [24], and the National Library of Medicine Image Registration Toolkit (ITK) have been established with the goal of quantifying the success of registration techniques.

Differences in the intensity histograms between Template and Target images further confound the problems of deformable image registration and subsequent quality assessment. In some common imaging modalities, signal intensity degrades non-uniformly over time and space, resulting in not only a general change in image intensity, but also a change in the intensity histogram. Additionally, and typical in the case of intersubject registrations, the Template and Target images originate from

completely different imaging sequences, hardware and/or even modalities. Because of these factors, the image histograms of the Template and Target may be significantly different – a fact that and can present a serious challenge in the process of deformable image registration.

The primary focus of the present work is to provide a nonbiased, hierarchical technique to quantify the quality of image registration with specific attention to the assessment of high-dimensional deformable image registrations. The technique is based on comparison of singular value decomposition (SVD) of the Template and Target images to decompose the image data into a hierarchical series of *singular modes*. As the deformable registration proceeds, the Template singular modes evolve and ultimately approach those of the Target. These modes provide a direct means to assess the quality of registration through comparison of inner products defined by the base vectors. The potential advantage of the technique comes largely because of the ability to separate a specific spatial distribution of image intensity (referred to herein as topology) from variations in intensity that are not associated with the topology of interest. The method allows the topology of the registered Template to be compared to the topology of the Target even in the presence of differences in image histograms. The technique is demonstrated using magnetic resonance (MR) images of the heart [25] and human distal phalanx [26], as well as optical images of primate brain cryosections [18].

Methods

In 1873-74 Eugenio Beltrami [27] and Camille Jordan [28], [29] independently demonstrated that any real *x*-by-*y* matrix $\boldsymbol{A}$ can be decomposed such that

$$\boldsymbol{A} = \boldsymbol{U}\boldsymbol{\Sigma}\boldsymbol{V}^{\mathrm{T}}. \tag{5.1}$$

Here, $\boldsymbol{U}$ and $\boldsymbol{V}$ are orthonormal matrices whose columns contain the singular *vectors* of the decomposition, and $\boldsymbol{\Sigma} = \mathrm{diag}(\sigma_1, \ldots, \sigma_r)$, $r = \min(x, y)$, with $\sigma_1 \geq \ldots \geq \sigma_r \geq 0$, contains the singular *values* of the decomposition (for clarity, a particular singular value is referenced as σ_i). This is commonly referred to as singular value decomposition (SVD). SVD has found application in image compression and for evaluating the "noise-level" of a matrix system or image based on the singular values [30].

To apply SVD to a 2D image, the intensity values of the pixels are placed into the corresponding locations in $\boldsymbol{A}$. Thus, if the image contains $(x \times y)$ pixels, the matrix $\boldsymbol{A}$ will have dimensions $(x \times y)$. The singular vectors then comprise a set of basis vectors that combine with the singular values to decompose the image into a set of modes. In the present work, the topology of the image is examined hierarchically by reconstructing the image one singular mode at a time. The matrix representation of the n$^{\mathrm{th}}$ singular mode ($\boldsymbol{A}_n$) is obtained by applying Eq. 5.1 to the n$^{\mathrm{th}}$ singular value, $\boldsymbol{A}_n = \boldsymbol{U}\boldsymbol{\Sigma}_n\boldsymbol{V}^T$, where the matrix $\boldsymbol{\Sigma}_n$ is formed by zeroing all elements in $\boldsymbol{\Sigma}$ with the exception of σ_n. In this manner, image data are represented as a series of decreasingly significant components. Figure 5.1 illustrates this concept for a MRI neuroanatomical slice.

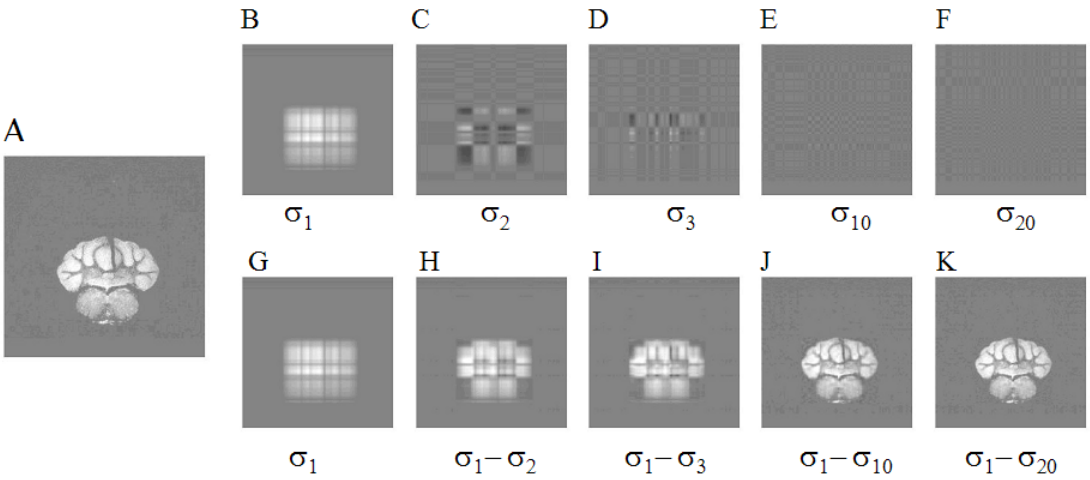

Figure 5.1. Singular value modes of a 2D image. Panel A shows a sagittal plane MR image of a mouse neuroanatomy. Panels B-F show individual modes of the image in panel A corresponding to 1, 2, 3, 10, and 20 singular values. Panels G-K show truncated reconstructions of the image in panel A corresponding to the indicated singular values.

3D Singular Value Decomposition

To apply SVD to 3D image data it was necessary to extend the concepts beyond the classical 2D matrix framework. There are several ways in which this could be done. In the present work the matrix containing the image intensity data $\boldsymbol{A}$ was arranged in a 3D rectangular format and decomposed separately for each image slice k (k=1…K),

$$\boldsymbol{A}^{(k)} = \boldsymbol{U}^{(k)}\boldsymbol{\Sigma}^{(k)}\boldsymbol{V}^{(k)^T} \tag{5.2}$$

to obtain a stacked set of 2D SVDs. The singular values from the stacked slices were then assembled as columns of a new matrix $\tilde{\boldsymbol{A}}$:

$$\tilde{\boldsymbol{A}} = \left[\boldsymbol{\Sigma}^{(1)} \quad \boldsymbol{\Sigma}^{(1)} \quad \ldots \quad \boldsymbol{\Sigma}^{(1)}\right] \tag{5.3}$$

This matrix, containing slice-by-slice singular values, was then subjected to a second SVD:

$$\widetilde{\boldsymbol{A}} = \widetilde{\boldsymbol{U}}\widetilde{\boldsymbol{\Sigma}}\widetilde{\boldsymbol{V}}^{T} \tag{5.4}$$

The nth 3D singular mode ($\tilde{\boldsymbol{A}}_n$) is obtained by applying Eqs. 5.2-5.4 to the nth singular value. For the kth slice this provides

$$\boldsymbol{A}_n^{(k)} = \boldsymbol{U}^{(k)}\boldsymbol{\Sigma}_n^{(k)}\boldsymbol{V}^{(k)^T} . \tag{5.5}$$

The matrix $\boldsymbol{\Sigma}_n^{(k)}$ is constructed in 3D for the kth slice of the nth singular mode using

$$\boldsymbol{\Sigma}_n^{(k)} = \left(\widetilde{\boldsymbol{U}}\,\widetilde{\boldsymbol{\Sigma}}_n\widetilde{\boldsymbol{V}}^{T}\right)_k^{T}\boldsymbol{I} \ , \tag{5.6}$$

where $\widetilde{\boldsymbol{\Sigma}}_n$ is obtained by zeroing all elements in $\widetilde{\boldsymbol{\Sigma}}$ with the exception of $\tilde{\sigma}_n$, the subscript k denotes the kth column, and $\boldsymbol{I}$ is the identity matrix. Note that this reduces to the 2D case described above if all slices are identical. Although this approach is not the only possible 3D decomposition, it preserves the hierarchical property and has well defined inner-products. Eqs. 5.2-5.6 will be referred to herein as 3D SVD.

Hierarchical Quantification of Image Registration

We now turn attention to application of 3D SVD to deformable Template registration. Our Lagrangian finite element (FE) based approach [16], [17] was used to generate specific example problems to demonstrate 3D SVD registration assessment and histogram normalization. In our method a one-to-one deformation map $\boldsymbol{\varphi}(\boldsymbol{X}) \in C^1(\Omega,\ \Re^3)$: $\det(\partial\boldsymbol{\varphi} / \partial\boldsymbol{X}) > 0$, is applied to the reference

configuration Ω. Material points with initial coordinates $\boldsymbol{X}$ in the undeformed Template are mapped to the coordinates $\boldsymbol{x}$ in the deformed configuration according to:

$$\boldsymbol{\varphi}(\boldsymbol{X}) = \boldsymbol{X} + \boldsymbol{u}(\boldsymbol{X}) = \boldsymbol{x}\,. \tag{5.7}$$

Here, $\boldsymbol{u}(\boldsymbol{X})$ is the displacement field. For simplicity, we assume in the present illustrative examples that the image data (intensity, spin, etc.) are convected with the material and that the deformation of the material does not change the image data. Upon completion of a perfect registration, the data attached to material in the undeformed Template (denoted $T(\boldsymbol{X})$) would be mapped to match the data in the Target (denoted $s(\boldsymbol{x})$) according to:

$$T(\boldsymbol{\varphi}^{-1}(\boldsymbol{X})) = T'(\boldsymbol{x}) \rightarrow s(\boldsymbol{x})\,, \tag{5.8}$$

where $\boldsymbol{T}'$ is the 3D scalar image intensity field of the deformed template. In the present examples the Target and the Template are 3D scalar image intensity fields but, in general, could be N-dimensional vector fields associated with multiple imaging sequences or modalities.

Measuring the extent to which the deformed Template $T'(\boldsymbol{x})$ matches the Target $s(\boldsymbol{x})$ using SVD is the principle aim of the present work. For this, the Target and the deformed Template fields are interrogated and interpolated to a discrete spatial lattice to form 3D image data. We define a set of *inner-products* of the deformed Template $\boldsymbol{T}'$ with the n$^{\text{th}}$ singular (column) vectors $\boldsymbol{u}_n$ and $\boldsymbol{v}_n$ of the Target $\boldsymbol{s}$. In 2D, the ratio of the scalar inner products $\alpha_n = \left(\boldsymbol{u}_n^{\mathrm{T}}\boldsymbol{T}'\boldsymbol{v}_n\right)\big/\left(\boldsymbol{u}_n^{\mathrm{T}}\boldsymbol{s}\boldsymbol{v}_n\right) = \left(\boldsymbol{u}_n^{\mathrm{T}}\boldsymbol{T}'\boldsymbol{v}_n\right)\big/\sigma_n$, for each

target mode, approaches a value of 1 as the deformed template approaches the target ($\alpha_n \to 1$ as $\boldsymbol{T}' \to \boldsymbol{s}$). In 3D, we define a single scalar for each 3D singular mode using Eq. 5.3:

$$\alpha_n = \frac{\tilde{\boldsymbol{u}}_n^T \tilde{\boldsymbol{T}}' \tilde{\boldsymbol{v}}_n}{\tilde{\boldsymbol{u}}_n^T \tilde{\boldsymbol{s}}\, \tilde{\boldsymbol{v}}_n} = \frac{\tilde{\boldsymbol{u}}_n^T \tilde{\boldsymbol{T}}' \tilde{\boldsymbol{v}}_n}{\tilde{\sigma}_n} \ , \tag{9}$$

where $\tilde{\boldsymbol{T}}'$ and $\tilde{\boldsymbol{s}}$ are obtained from the deformed Template and target images using Eq. 5.3. The lower case singular vectors are from Eq. 5.3 computed for the target matrix $\tilde{\boldsymbol{s}}$. Consistent with the 2D degenerate case, $\alpha_n \to 1$ as $\tilde{\boldsymbol{T}}' \to \tilde{\boldsymbol{s}}$. Numerical evaluation of this inner product in simulated test problems confirms the property of invariance under translation and rotation in the image space. This inner-product ratio provides a scalar measure of the projection, or correspondence, between the n^{th} singular mode of the Target and that of the deformed Template. Comparison of the inner-product ratios in ascending order provides a hierarchical method to quantify the quality of the registration.

Illustrative Examples

The illustrative examples presented in the results section were generated using our continuum mechanics based imaged registration technique (Warping). A brief description of the technique is given below, for additional details please reference Rabbitt et al. [17], or Veress et al. [31]. Registration was accomplished by minimization of a combined energy functional composed of both mechanical strain energy and image energy terms – a general formulation that degenerates to the Bayesian approach with appropriate assumptions on the likelihood of the data.

Template data used here were static sets of medical images acquired from a reference anatomical state. A FE model was then constructed to encompass the region of interest in the Template. The image data from the Template were interpolated to the nodes of the FE computational mesh. The geometry of the FE model was then deformed until the deformed version of the Template registered with the Target.

Two types of example problems are presented. In the first, the Target data were defined by a time sequence of images taken from a single subject – with the data prior to deformation defining the Template. This case typifies strain-tracking problems common in soft tissue biomechanics [16], [25], [26], [32]. In the second case, the Template and Target data were taken from entirely different subjects. This case typifies segmentation or registration problems frequently encountered in medical imaging [18], [31], [33]. One goal is common to these problems: determine the deformation map that aligns the deformed Template with the Target. Example results applying SVD to problems of both types are provided below.

Circular Inclusion

Images of a circular inclusion were generated to illustrate the evolution of the SVD inner products in a "perfectly" registered example problem. The images used for the circular inclusion were computer-generated 8 bit grayscale images with a 256x256 image matrix. A circular portion of the images (radius of 16 pixels) was white while the image background was black. The images were blurred by convolution with standard Gaussian spatial filter with a 32 pixel radius (see Figure 5.2).

A FE mesh consisting of two regions was constructed. The first region

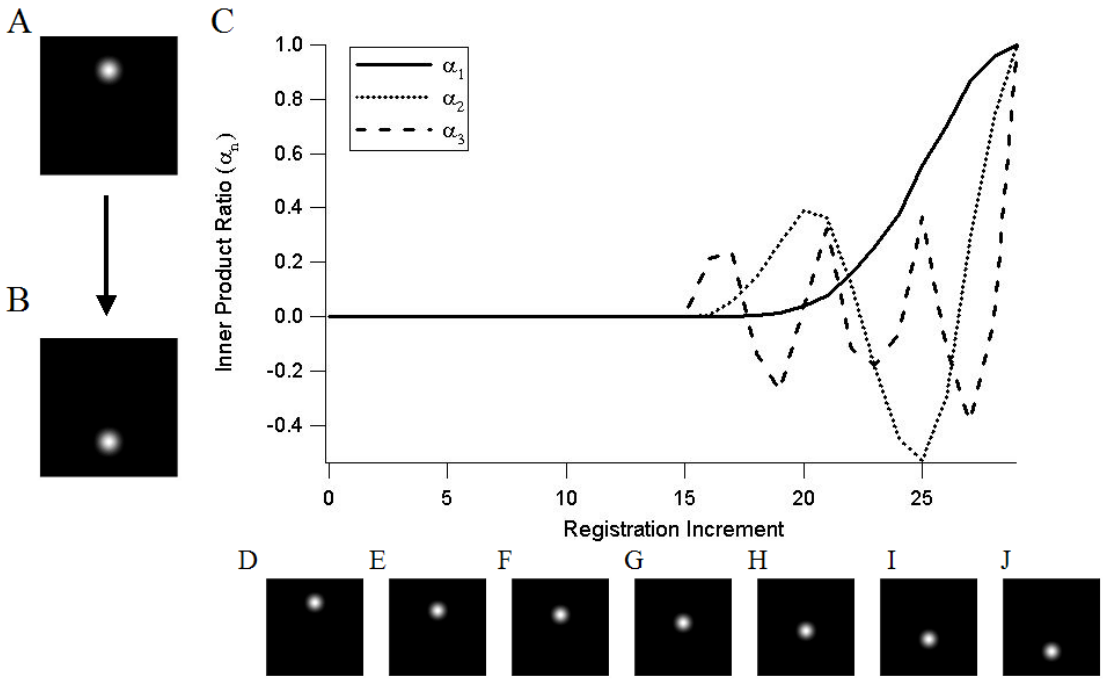

Figure 5.2. Inner product tracking of a circular occlusion undergoing vertical displacement. Panels A and B show the computer generated template and target images, respectively. Panel C shows the evolution of the deformed Template inner products (α_n) during the registration process. Panels D-J show the deforming Template at specific registration iterations corresponding to the graph in panel C (0,5,10,15,20,25,30 iterations).

corresponded to the circular inclusion while the second region consisted of the surrounding image data. The boundary edges of the second region were constrained from both vertical and horizontal motion. No other external boundary conditions were applied. An additional spatial filter was initially applied (192 pixel radius) to the image data so that gradient information from the Template and Target overlapped. Following registration of these filtered images, the filtering was gradually removed as the registration computations proceeded to completion (dynamic filtering) [31]. The final registered Template image was obtained by interpolating the deformation predicted by the FE model to the original spatial grid of the Template data (using tri-linear interpolation).

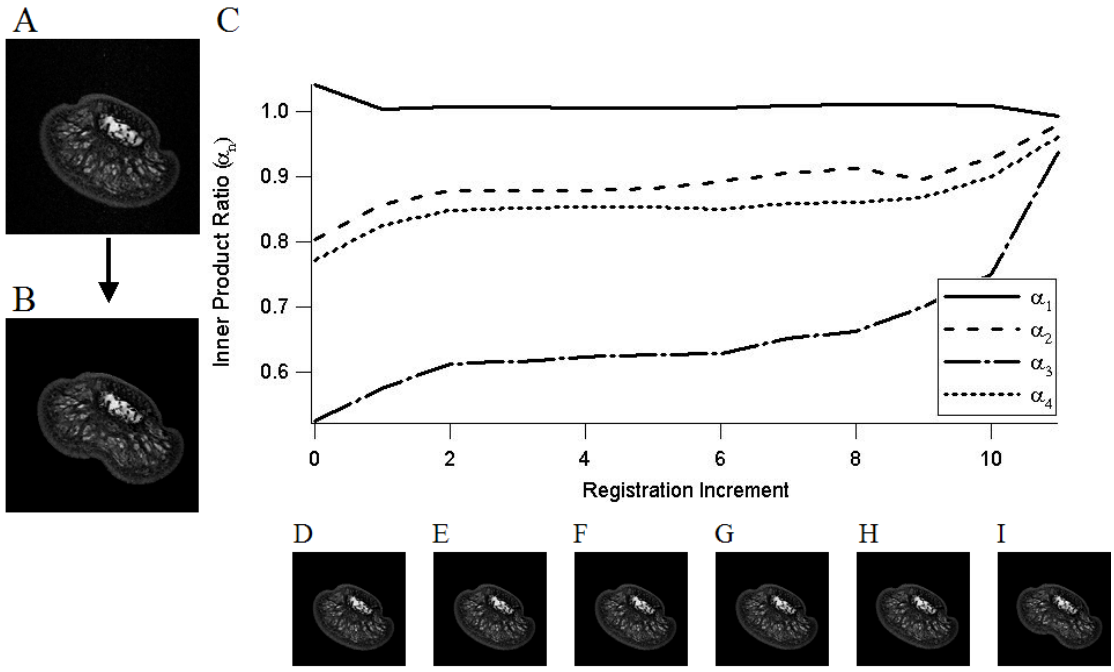

Figure 5.3. Inner product tracking of a distal phalanx under indentation. Panels A and B show the Template and Target MR images, respectively. Panel C shows the evolution of inner product ratios computed from the deformed template data using the target singular vectors. Panels D-I show intermediate registration results at each iteration of the registration process.

Distal Phalanx

High-resolution MR data from the distal phalanx were collected to demonstrate the evolution of inner products in an anatomical registration problem. A 4.7 Tesla magnet and a RARE sequence were used to obtain high-resolution (125 x 125μm) MR images of the healthy human male fingerpad [34]. The nail of the distal phalanx of the subject was rigidly constrained using a specially constructed, nonmagnetic frame. The Template image represented a cross-section of the finger (Figures 5.3A, 5.4A). Mechanical indentation of 1-2 mm was applied to the finger pad with a nonmagnetic,

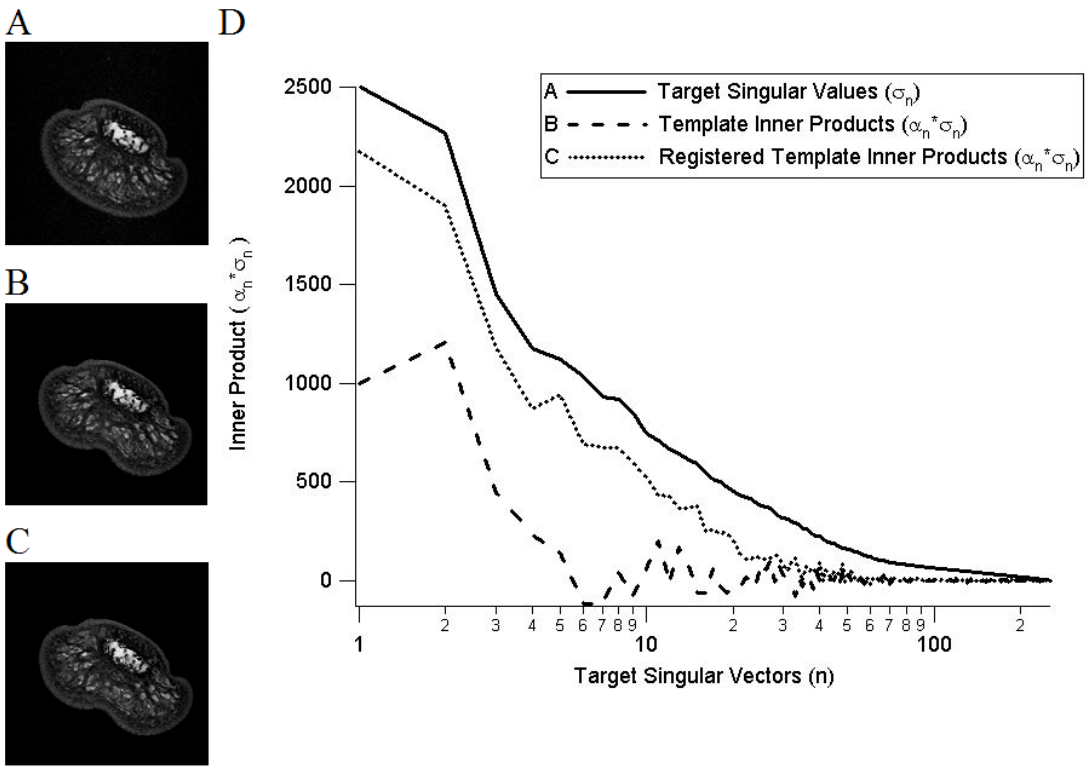

Figure 5.4. Singular values of the distal phalanx Template and Target. Panels A and B show the Template and Target MR images, respectively. Panel C shows the registered (deformed) Template. Panel D compares the inner product of the deformed Template with the singular vectors of the Target to the same inner product for the undeformed Template.

rectangular indenter. Constant indentation was maintained by mounting the indenter to the constraint frame. The Target image was obtained during a maintained indentation of the finger pad (Figures 5.3B, 5.4B).

A FE mesh was constructed based on a manual segmentation of the undeformed Template image. This mesh was divided into three regions based on tissue type. Hypoelastic material properties were assigned from the literature [35] as follows: bone ($E = 15\times10^8$ Pa, $\nu = 0.48$), dermis ($E = 15\times10^4$ Pa, $\nu = 0.48$), other tissue ($E = 15\times10^3$ Pa, $\nu = 0.48$). No externally applied loads or boundary conditions were imposed on the model, thus deformation of the mesh was exclusively due to the

image registration process. As described for the circular inclusion example, dynamic spatial filtering was applied to both the Template and Target images during registration. Following registration, the computed deformation field was interpolated from the FE model to the original spatial grid of the Template data.

Macaque Neuroanatomy

Optical data from a Macaque monkey brain were used to illustrate the utility of the present method to distinguish between local minima in the registration process. The digital images of the macaque neuroanatomy were generated by block microtome cryosectioning and CCD digitization of 100-μm sections from two macaque monkeys (images from D. VanEssen, [18]).

Registration of the macaque datasets was accomplished by first generating a rectangular FE mesh corresponding to the domain of the Template data. An elastic-plastic material model was applied to the FE mesh ($E = 15\times10^3$ Pa, $\nu = 0.1$, $\sigma_{yield} = 15\times10^3$ Pa). The outside edges of the mesh were constrained from both vertical and horizontal motion. No other external boundary conditions were applied. Dynamic spatial filtering was applied to the Template and Target image data during deformation. The different registrations examined in panels C and D of Figure 5.5 were obtained by varying the degree of spatial filtering applied to the image data, with all other parameters held constant. The registration shown in Figure 5.5C was generated using a constant radius filter of 3 pixels, while that in Figure 5.5D was generated using a dynamic filter, which evolved from 15 to 3 pixels during the registration process.

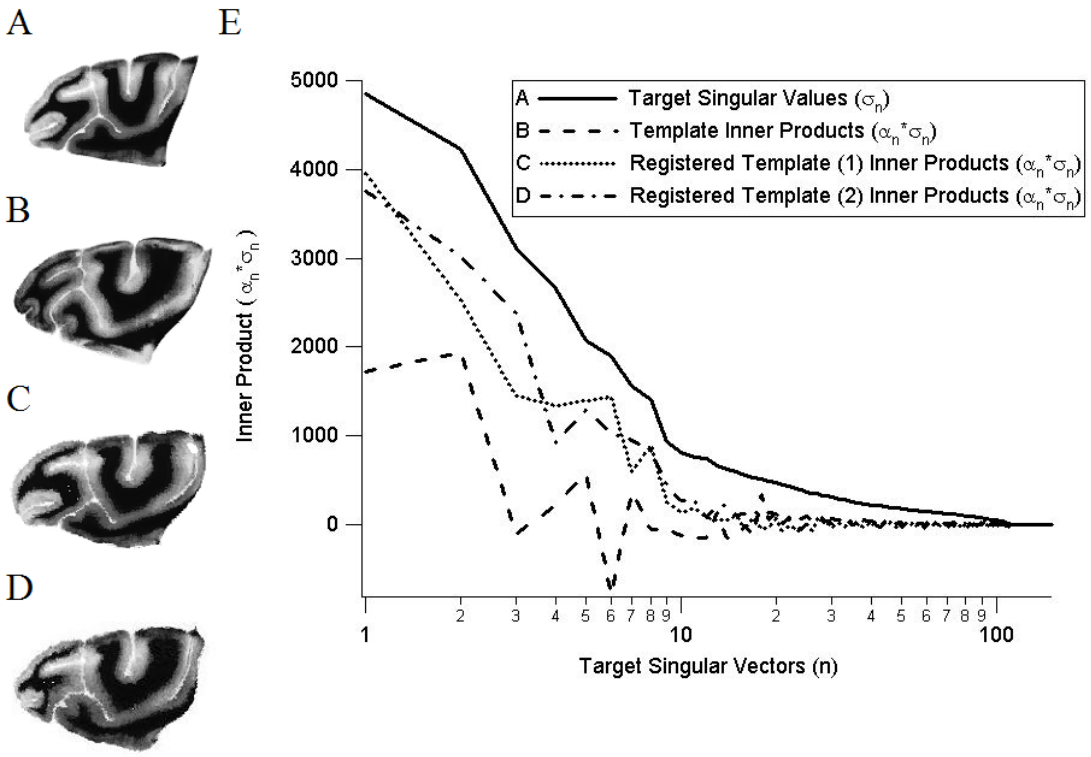

Figure 5.5. Singular values of the macaque neuroanatomy Template and Target. Panels A and B show the Template and Target images, respectively. Panels C and D show different registration solutions (local minima) of the same problem. Panel E compares the inner product of the deformed Template with the singular vectors of the Target to the same inner product for the undeformed Template.

Human Left Ventricle

Gated MR images of the left ventricle of a healthy human male subject [25] were used to illustrate application of the 3D SVD. Briefly, two volumetric MR image datasets were acquired using a 1.5T Siemens scanner (256x256 image matrix, 378 mm FOV, 10 mm slice thickness, 10 slices). The volumetric MR data corresponding to end-systole were designated as the Template and the data corresponding to end-diastole were designated the Target. (Figure 5.6A, 5.6B)

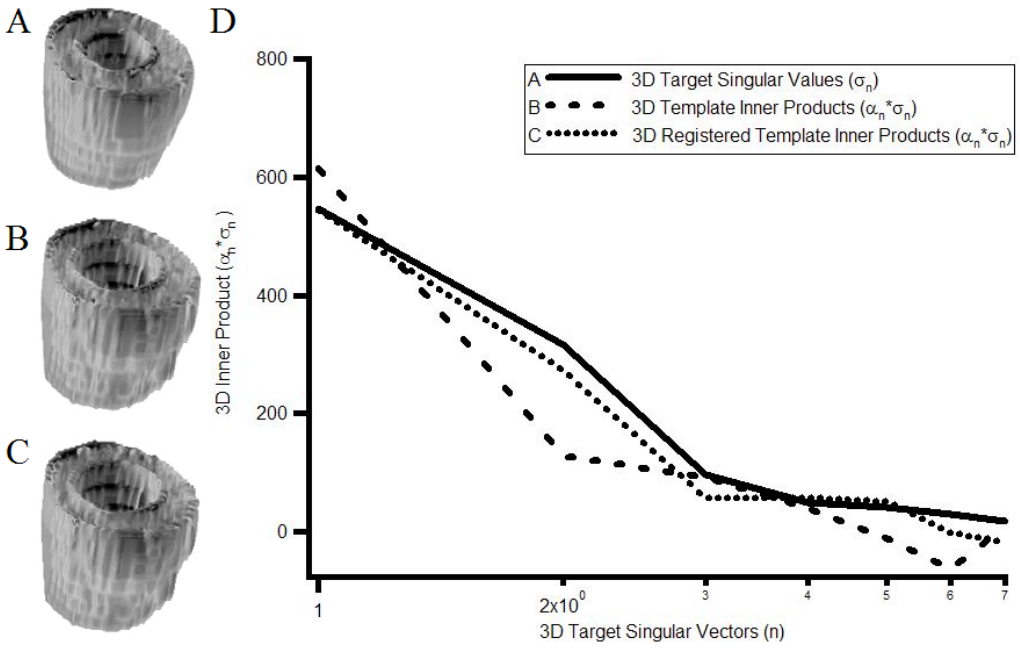

Figure 5.6. Singular values of the 3D human left ventricle Template and Target. Panels A and B show surface renderings of the Template and Target image data, respectively. Panels C shows a surface rendering of the registration solution. Panel D quantifies the image registration by projecting the 3D singular vectors of the Target image dataset onto the Template image dataset and the registered image dataset. The inner products of the registered solution show close correspondence with the singular values of the Target image dataset.

Contours of the left ventricular endocardial and epicardial surfaces were segmented manually from the end-systolic MR image dataset and then used to construct polygon surfaces via Delaunay triangulation [36]. A FE mesh was constructed based on the surfaces. A transversely isotropic hyperelastic material model was used to model the heart muscle tissue. The ventricle wall was divided radially into four regions, each with a distinct fiber angle as described by Veress et al. [25]. Fiber angle varied between 90 degrees on the endocardial surface to -90 degrees on the epicardial surface of the left ventricle. The material properties of the myocardial wall were determined from least squares curve fits of the biaxial test data

reported by Humphrey et al. [37], [38]. No external boundary conditions were applied during registration.

Results

Circular Inclusion

Figure 5.2 shows results for the computer generated example problem of a bright, circular inclusion that changes position vertically over time. Panels A and B show the Template and Target images, respectively. Panels D-J correspond to the deformed Template configuration at the registration iteration (computational timestep) indicated directly above on the horizontal axis and show intermediate positions of the inclusion during registration. The vertical axis of panel C shows the normalized inner products (α_i) during the registration process. The horizontal axis corresponds to computational iteration of the registration process. Results demonstrate that as the position of the inclusion in the registered Template approaches that of the Target, the values of α_i converge to unity. Oscillations in the values of the normalized inner products can be seen near the end of the registration process. The oscillations demonstrate one consequence of images with non-unique registration solutions – i.e. the lack of rotational orientation information present in this particular example problem.

Distal Phalanx

Figure 5.3 shows results from registration of micro-MRI of a human distal phalanx before and during indentation. A Template image was interrogated from a cross-section of the finger (panel A). Mechanical indentation was applied to the finger

pad and a Target image was interrogated (panel B). Panels D – I provide results at intermediate steps in the registration process. At each solution increment, the computed deformation field was applied to the Template image to produce a snapshot in computational time. If perfect registration were achieved, panel J would be identical to the Target image (panel B). The graph in panel C tracks the progression of the Template topology towards that of the Target. The horizontal axis of the graph shows the solution increment (directly corresponding to panels D-I), while the vertical axis shows the computed normalized inner products (α_i). The four most significant (lowest order) inner products are shown. Perfect agreement in singular vectors between the Template and Target would correspond to a value of unity of each inner product at the conclusion of the registration process. Note how the vectors uniformly move toward this value, measuring success of the registration process.

Figure 5.4 presents an alternate depiction of the same results. The Template (panel A), Target (panel B), and registered Template (panel C) are shown on the left. The horizontal axis of panel D defines the singular index, while the vertical axis is value of the inner product. The top solid curve shows the Target singular values. The bottom dashed curve shows the Template inner products (an inner product map) before registration. The dotted line shows the deformed Template inner products following registration. Results demonstrate the improved agreement in topology following registration. A logarithmic axis was used on the horizontal scale to emphasize the decreasing importance of the higher order singular vectors and values as the noise level of the images was approached.

Macaque Cryosections

Figure 5.5 show results for the intersubject registration of optical images of stained macaque brain cryosections [18]. Panels A and B show the Template and Target images respectively. Panels C and D show two registration solutions, neither exact, corresponding to local minima in the registration problem. Comparison of the two solutions by other common registration assessment techniques such as subtraction, SSD, and histogram comparison rank the registrations differently. The graph in Panel E shows the inner products of the Template, Target, and both registrations. The axes used are the same as in Figure 5.4D. Results demonstrate that the inner products can identify particular modes of the registered Template that are out of correspondence with the Target. Local minima in the energy functional are identified in the inner product map as sharp changes in the curvature.

Human Left Ventricle

Figure 5.6 illustrates application to 3D registration of MR images of a human left ventricle. Panels A and B show surface renderings of the 3D Template and Target data respectively. Panel C shows the registration solution. The 3D SVD algorithm was used to decompose the Target. The 3D singular vectors were projected onto the Template and registered Template image data sets. Panel D shows the inner products of the Template, Target, and deformed Template. The inner products of the deformed Template closely matched the Target and providing a quantitative measure of the quality of the 3D registration.

Discussion

The primary objective of this work was to develop an objective quantitative assessment technique for evaluating the success of deformable image registration. Specifically, the technique allows for hierarchical evaluation of the correspondence in image topology between a Target and the deformed Template. Hierarchical evaluation is important because many registration problems contain inadequate or conflicting image data, as well as a multitude of possible solutions (local minima in the functional). Although the examples in the present work use a mechanics-based deformable Template registration technique, the assessment methods could be applied to any image registration technique. Results demonstrate that inner products of the deformed Template with the Target singular vectors provide an effective method of quantifying registration quality.

The computer generated circular inclusion example presented in Figure 5.2 demonstrates several characteristics of the singular vector projection technique. The technique tracks the progress of each Template singular vector towards registration with the corresponding Target singular vector. Another notable characteristic of the technique is that although singular values are always positive, inner products (especially those corresponding to the higher order singular vectors), can be negative. Oscillations in the solution occur due to lack of orientation information present in the image data. Image data that contain a greater amount of texture data to orient the registration do not exhibit this phenomenon (reference the fingerpad indentation example in Figure 5.3).

Further application of the method can be seen as a nonbiased evaluation function to determine the degree of topological match between two images. In this case it is appropriate to evaluate the complete set of singular values and corresponding topology multipliers. In registration problems it is often insightful to compare the Target image topology with the topologies of both the original Template image and the registered Template image. The inner product map is a useful tool for graphically displaying this information. The maps presented in Figures 5.4 - 5.6 show the improvement in topological correspondence between the Template and Target images that was obtained through the registration process. Because the technique is based on the singular value decomposition, it is known that the highest order singular vectors correspond to the noise level of the images. Thus assessment of registration results can be based only on lower order singular vectors (i.e., where the information is above the background noise level of the image).

In many cases inner product maps can identify local minima in the registration process. Local minima are identified as sharp changes in the value of the inner products between adjacent singular vectors (a sawtooth pattern in the inner product map). For instance, in the macaque neuroanatomy registration example (Figure 5.5), there are several local minima, which can be observed from the inner product map of the Template. Local minima which correspond to lower order singular vectors are significantly more important than those corresponding to higher order singular vectors. The two quasi-registered solutions in panels C and D of Figure 5.5 show local minima in their inner product maps, indicating they are not fully registered with the Target image.

Acknowledgments

The MR images used for the fingerpad indentation analysis were provided by Mandayam Srinivasan, Kimberly Voss, and Josh Cysyk of the MIT Laboratory for Human and Machine Haptics. Macaque brain cryosection data was provided by D. C. Van Essen of Washington University. We thank Dr. Bradley N. Maker for his continued collaboration on code development in NIKE3D. Partial support was provided by the NIH DC01837 & MH/DA52158.

References

1. M.I. Miller, A. Trouvé, and L. Younes, "On the metrics and euler-lagrange equations of computational anatomy," *Annu. Rev. Biomed. Eng.*, vol. 4, pp. 375-405, 2002.

2. C.A. Glasbey and K.V. Mardia, "A review of image-warping methods," *J. Appl. Stat.*, vol. 25, no. 2, pp. 155-172, 1998.

3. T. McInerney and D. Terzopoulos, "Deformable models in medical image analysis: A survey," *Med. Image Anal.*, vol. 1, no. 2, pp. 91-108, 1996.

4. T.M. Cover and P.E. Hart, "Nearest neighbor pattern classification," *IEEE Trans. Information Theory*, vol. IT-13, no. 1, pp. 21-27, 1967.

5. B.S. Everitt, *Cluster Analysis,* 3rd ed*.,* London: Edward Arnold, 1993.

6. B.D. Ripley, *Pattern Recognition and Neural Networks*, Cambridge University Press, 1996.

7. C. Cortes and V. Vapnik, "Support vector networks," *Machine Learning*, vol. 20, 1995.

8. Y. Amit, "Graphical shape templates for automatic anatomy detection with applications to MRI brain scans," *IEEE Trans. Med. Imaging*, vol. 16, no. 1 (Feb), pp. 28-40, 1997.

9. L.K. Arata, A.P. Dhawan, J.P. Broderick, M.F. Gaskil-Shipley, A.V. Levy, N.D. Volkow, A.P. Dhawan, and J. Mantil, "Three-dimensional anatomical

model-based segmentation of MR brain images through principal axis registration," *IEEE Trans. Biomed. Engineering*, vol. 42, no. 11 (Nov), pp. 1069-1077, 1995.

10. A.P. Dhawan, L.K. Arata, A.V. Levy, and J. Mantil, "Iterative principal axis registration method for analysis of MR-pet brain images," *IEEE Trans. Biomed. Engineering*, vol. 42, no. 11 (Nov), pp. 1069-1077, 1995.

11. M. Kass, A. Witkin, and D. Terzopoulus, "Snakes: Active contour models" *Int. J. Comp. Vision*, vol. 1, pp. 321-331, 1988.

12. L. Cohen and R. Kimmel, "Global minimum for active contour models: A minimal path approach " *Int. J. Comp. Vision*, vol. 24, no. 1, pp. 57-78, 1997.

13. A. Klemencic, S. Kovacic, and F. Pernus, "Automated segmentation of muscle fiber images using active contour models," *Cytometry*, vol. 32, pp. 317-326, 1998.

14. R. Bajcsy and S. Kovacic, "Multiresolution elastic matching," *Comp. Vision Graph. Image Processing*, vol. 46, pp. 1-21, 1989.

15. G.E. Christensen, R.D. Rabbitt, and M.I. Miller, "Deformable templates using large deformation kinematics," *IEEE Trans. Image Processing*, vol. 5, no. 10, pp. 1435-1447, 1996.

16. J.A. Weiss, R.D. Rabbitt, and A.E. Bowden, "Incorporation of medical image data in finite element models to track strain in soft tissues," *SPIE Biomed. Optics Symp. BiOS98*, vol. 3254, pp. 477-484, 1998.

17. R.D. Rabbitt, J.A. Weiss, G.E. Christensen, and M.I. Miller, "Mapping of hyperelastic deformable templates," *Proc. SPIE*, vol. 252, pp. 252-265, 1995.

18. A.E. Bowden, R.D. Rabbitt, J.A. Weiss, and B.N. Maker, "Anatomical registration and segmentation by warping template finite element models," *Proc. SPIE*, vol. 3254, pp. 469-476, 1998.

19. C.A. Pelizzari, A.C. Evans, P. Neelin, C.-T. Chen, and S. Marrett, "Comparison of two methods for 3D registration of PET and MRI images," *Annual Conf. Engineering Med. Biology*, vol. 13, pp. 221-223, 1991.

20. H. Neemuchwala, A. Hero, and P. Carson, "Feature coincidence trees for registration of ultrasound breast images," *IEEE Int. Conf. Image Process.*, vol. 3, pp. 10-13, 2001.

21. I.D. Dinov and D.W.L. Sumners, "Applications of frequency dependent wavelet shrinkage to analyzing quality of image registration," *SIAM J. Appl. Math*, vol. 62, no. 2, pp. 367-384, 2001.

22. P. Viola and W.M. Wells III, "Alignment by maximization of mutual information," *Int. J. Comp. Vision*, vol. 24, no. 2, pp. 137-154, 1997.

23. P. Hellier, C. Barillot, I. Corouge, B. Gibaud, G.L. Goualher, L. Collins, A. Evans, G. Malandain, and N. Ayache. "Retrospective evaluation of inter-subject brain registration". in *Medical Image Computing and Computer Assisted Intervention*, Utrecht, The Netherlands: Springer-Verlag, 2001.

24. J. West, J.M. Fitzpatrick, M.Y. Wang, B.M. Dawant, J. C. R. Maurer, R.M. Kessler, R.J. Maciunas, and et. al., "Comparison and evaluation of retrospective intermodality image registration techniques," *J. Comp. Assist. Tomography*, vol. 21, pp. 554-566, 1997.

25. A.I. Veress, J.A. Weiss, G.J. Klein, and G.T. Gullberg. "Quantification of 3d left ventricular deformation using hyperelastic warping: Comparisons between MRI and PET imaging," in *Computers in Cardiology*, Memphis, TN, 2002.

26. A.E. Bowden, R.D. Rabbitt, and J.A. Weiss, "Stress and strain in the human distal phalanx under indentation," *Proc. BMES/EMBS Conf. in Atlanta GA*, 1999.

27. E. Beltrami, "Sulle funzioni bileari," *Giornale di Matematiche ad Uso degli Studenti Delle Universita*, vol. 11, pp. 98-106, 1873.

28. C. Jordan, "Sur la réduction des formes bilinéaires," *Comptes Rendus de l'Académie des Sciences, Paris*, vol. 78, pp. 614-617, 1874.

29. C. Jordan, "Mémoire sur les formes bilinéaires," *Journal de Mathématiques Pures et Appliquées, Deuxième Série*, vol. 19, pp. 35-54, 1874.

30. P.C. Hansen, "Rank-deficient and discrete ill-posed problems: Numerical aspects of linear inversion," Siam. 1997. 247.

31. A.I. Veress, J.A. Weiss, R.J. Gillies, A.E. Bowden, J.-P. Galons, and R.D. Rabbitt, "Quantification of changes in mouse brain morphology using MRI and hyperelastic warping," *IEEE Trans. Med. Imaging*, to be published.

32. A.E. Bowden, R.D. Rabbitt, J.A. Weiss, and B.N. Maker, "Use of medical image data to compute strain fields in a spinal disc," *Proc. ASME Bioeng. Conf.*, vol. BED-35, pp. 191-192, 1997.

33. J.A. Weiss, A.I. Veress, A.E. Bowden, R.D. Rabbitt, R.J. Gillies, J.-P. Galons, and J. Guo, "Local measurements of changes in shape and volume between serial volumetric medical images: Application to niemann-pick type c disease progression," *Center for High Performance Computing News, University of Utah*, vol. 12, no. 3, pp. 1-3, 2001.

34. K.J. Voss and M.A. Srinivasan, "Investigation of the internal geometry and mechanics of the human fingertip, in vivo, using magnetic resonance imaging," Touch Lab Report, Cambridge, MA, MIT RLE TR-622, 1998.

35. R.J. Gulati and M.A. Srinivasan, "Determination of mechanical properties of the human fingerpad, in vivo, using a tactile stimulator," Touch Lab Report, Cambridge, MA, MIT RLE TR-605, 1996, p. 265.

36. B. Geiger, "Three-dimensional modeling of human organs and its application to diagnosis and surgical planning," INRIA Report, INRIA-2105, 1993.

37. J.D. Humphrey, R.K. Strumpf, and F.C. Yin, "Determination of a constitutive relation for passive myocardium: I. A new functional form," *J. Biomech. Eng.*, vol. 112, pp. 333-339, 1990.

38. J.D. Humphrey, R.K. Strumpf, and F.C. Yin, "Determination of a constitutive relation for passive myocardium: II. Parameter estimation," *J. Biomech. Eng.*, vol. 112, pp. 340-346, 1990.

CHAPTER 6

INFLUENCE OF LOCAL DATA ON DEFORMABLE IMAGE REGISTRATION

Abstract

The primary goal of this work was to evaluate the local influence of image data and registration parameters on deformable image registration results. To this end, several quantitative measures of influence have been developed and evaluated. The measures were derived from the variances of the terms and parameters of the registration potential function. These measures were used to evaluate registration results obtained using a continuum mechanics based image registration method. Illustrative examples include registration of a Gaussian blur, a human fingerpad, and a human spinal disc. Results demonstrated that a ratio of the individual variances of the image potential and the deformation potential with respect to the template configuration provided insight into the relative local influence of registration data on registration solutions.

Introduction

The goal in deformable image registration methods is to find a transformation of the template image that best aligns the features of the image with those of a target image. In the ideal case, the quantity and quality of the image texture present in the

template and target images, as well as the similarity in underlying anatomical structure, would yield a unique "best" transformation. In real problems, however, this is not the case. Image registration is most often ill-posed in the sense of Hadamard [1], [2]. No perfect transformation exists, and the solution depends on the choice of registration method. The dependence is most significant in regions of the template model where image texture is sparse or conflicting. In these regions, the registration solution is computed based on minimizing the deformation potential (Bayesian prior probability) portion of the particular registration cost functional [3]. Other investigators have recognized this type of ambiguity. The Retrospective Registration Evaluation Project [4], the Vista Project [5], and the National Library of Medicine Image Registration Toolkit (ITK) have been established with the goal of quantifying the success of image registration techniques. These projects have focused on ranking the performance of image registration techniques using a set of predefined registration problems. Many deformable image registration methods utilize a dual term potential energy function (cost function) to guide registration [3], [6-15]. In these methods, one term is associated with a measure of image alignment between the template and target images (the image potential), while the other term is specific to the particular registration method and defines the energy associated with deformation (the deformation potential). Registration is accomplished by finding the configuration of the template model that minimizes both energy terms simultaneously. The deformation potential is formulated to regularize the registration problem and is often based on a physical analog to a particular type of material behavior (e.g., a viscous fluid or hyperelastic solid) [6], [7], [16-19]. This type of constraint ensures a one-to-

one mapping between the template and target based on the principles of continuum mechanics [20]. The particular type of regularization will influence the registration results in local regions where the image-based energy does not result in significant forces to drive the registration.

The objective of this study was to evaluate the relative local influence of the image functional and the deformation functional on the results of deformable image registration. The variances of the individual terms of the combined potential energy function with respect to the final template configuration were used to construct scalar measures that provided this information locally. For finite element based deformable image methods, the variances are related to the tangent stiffness matrix.

Methods

Implementation

The present work was implemented into the continuum mechanics based image registration method termed hyperelastic Warping, originally developed by Rabbitt and Weiss [13], [15], [21], [22]. Only a brief review of the salient points is described in the present work. Full implementation details for the method are given elsewhere [13], [21]. The standard notation and symbols of modern continuum mechanics are employed in the following presentation [23], [24]. In particular, direct notation is used with boldface italics for vector and tensor fields. Index notation is incorporated for quantities that cannot be readily written in direct notation. Where applicable, the condensed Voigt notation typically employed in finite element analysis is utilized [25].

The objective is to deform a representation of a template image into alignment with a target image. The formulation is Lagrangian and thus the deformation of the template particles is tracked. Assume that the scalar intensity fields of the template and target, T and S, are not changed by the deformation. T is defined in the reference configuration and thus we write $T(\boldsymbol{X})$. Since the values of S at points associated with the deforming template change as the template mesh deforms, we write $S(\boldsymbol{\varphi})$, where $\boldsymbol{\varphi}(\boldsymbol{X}) = \boldsymbol{X} + \boldsymbol{u}(\boldsymbol{X})$ is the deformation map from template to target, and $\boldsymbol{u}(\boldsymbol{X})$ is the displacement field. A finite element (FE) mesh is constructed to correspond to all or part of the template image (either rectilinear, or a "conforming" mesh that represents a particular structure of interest in the Template image). The template intensity field T is interpolated to the nodes of the FE mesh. The intensity data for the template are convected with the FE mesh and thus the nodal values do not change. As the FE mesh deforms, we query the values of the target intensity S at the template nodes.

A combined potential energy functional is constructed that consists of two potential energy terms:

$$E = \int_{\beta_0} W\left(\boldsymbol{X}, \boldsymbol{\varphi}\right) dV - \int_{\beta_0} U\left(\boldsymbol{X}, \boldsymbol{\varphi}\right) dV \,. \tag{6.1}$$

W is the standard strain energy density function from continuum mechanics that defines the material constitutive behavior, while U represents an image energy density functional. β_0 represents the volume of integration of the template model in the reference configuration. The present work uses a Gaussian sensor model to describe the image energy density functional as:

$$U(\boldsymbol{X},\boldsymbol{\varphi}) = \frac{\lambda}{2}\left(T(\boldsymbol{X}) - S(\boldsymbol{\varphi})\right)^2. \tag{6.2}$$

λ is a Lagrange multiplier [26], which enforces the alignment of the template model with the target image data.

The weak form of the momentum equations (Euler-Lagrange equations) is obtained by taking the first variation of $E(\boldsymbol{\varphi})$ with respect to the deformation $\boldsymbol{\varphi}$. This can be though of as a "virtual displacement" – a small variation in the current coordinates $\boldsymbol{x}$, denoted $\varepsilon\boldsymbol{\eta}$. Here ε is an infinitesimal scalar. The variation of the first term in (1) yields the standard weak from of the momentum equations for nonlinear solid mechanics (see, e.g., [23]). The functional in (2) gives rise to an image-based force term. The first variation of (2) with respect to the deformation $\boldsymbol{\varphi}(\boldsymbol{X})$ in direction $\boldsymbol{\eta}$ is denoted:

$$DU(\boldsymbol{\varphi})\cdot\boldsymbol{\eta} = D\left[\frac{\lambda}{2}\left(T(\boldsymbol{X}) - S(\boldsymbol{\varphi})\right)^2\right]\cdot\boldsymbol{\eta}. \tag{6.3}$$

This is calculated using the Gateaux derivative [23] by taking the derivative of the functional U evaluated at $\boldsymbol{\varphi} + \varepsilon\boldsymbol{\eta}$ with respect to ε and then letting $\varepsilon \to 0$:

$$DU(\boldsymbol{\varphi})\cdot\boldsymbol{\eta} = \lambda\left[\left(T(\boldsymbol{X}) - S(\boldsymbol{\varphi}+\varepsilon\boldsymbol{\eta})\right)\frac{\partial}{\partial\varepsilon}\left(T(\boldsymbol{X}) - S(\boldsymbol{\varphi}+\varepsilon\boldsymbol{\eta})\right)\right]_{\varepsilon\to 0}. \tag{6.4}$$

Noting that

$$\left[\frac{\partial}{\partial\varepsilon}\left(T(\boldsymbol{X}) - S(\boldsymbol{\varphi}+\varepsilon\boldsymbol{\eta})\right)\right]_{\varepsilon\to 0} = \left[-\frac{\partial S(\boldsymbol{\varphi}+\varepsilon\boldsymbol{\eta})}{\partial(\boldsymbol{\varphi}+\varepsilon\boldsymbol{\eta})}\cdot\frac{\partial(\boldsymbol{\varphi}+\varepsilon\boldsymbol{\eta})}{\partial\varepsilon}\right]_{\varepsilon\to 0} = -\frac{\partial S(\boldsymbol{\varphi})}{\partial\boldsymbol{\varphi}}\cdot\boldsymbol{\eta}, \tag{6.5}$$

we can combine (3) and (4) to get:

$$DU(\boldsymbol{\varphi})\cdot\boldsymbol{\eta} = -\lambda\left[\left(T(\boldsymbol{X}) - S(\boldsymbol{\varphi})\right)\frac{\partial S(\boldsymbol{\varphi})}{\partial \boldsymbol{\varphi}}\cdot\boldsymbol{\eta}\right]. \tag{6.6}$$

This term gives rise to the image-based body force that drives the deformation.

A similar computation for the term W leads to the Euler-Lagrange equations. After tranformation to the current (deformed) configuration,

$$G(\boldsymbol{\varphi},\boldsymbol{\eta}) := DE(\boldsymbol{\varphi})\cdot\boldsymbol{\eta} = \int_{\beta}\frac{1}{2}\boldsymbol{\sigma}\left(\frac{\partial\boldsymbol{\eta}}{\partial\boldsymbol{\varphi}} + \frac{\partial\boldsymbol{\eta}}{\partial\boldsymbol{\varphi}}\right)dv - \int_{\beta}\left[\lambda(T-S)\left(-\frac{\partial S}{\partial\boldsymbol{\varphi}}\right)\cdot\boldsymbol{\eta}\right]\frac{dv}{J} = 0. \tag{6.7}$$

Here, $\boldsymbol{\sigma}$ is the 2nd order symmetric Cauchy stress tensor. Thus, the forces due to the image data balance with the forces derived from the deformation of the material through the constitutive model.

An incremental-iterative solution method is used to obtain the configuration $\boldsymbol{\varphi}$ that satisfies equation (6.7) [27]. Assuming that the solution at a configuration $\boldsymbol{\varphi}^*$ is known, we seek the solution at some increment $\boldsymbol{\varphi}^* + \Delta\boldsymbol{u}$. To achieve this, we require the linearization of (7) at $\boldsymbol{\varphi}^*$ to get an initial estimate for $\Delta\boldsymbol{u}$:

$$L_{\boldsymbol{\varphi}^*}\, G(\boldsymbol{\varphi},\boldsymbol{\eta}) = G\left(\boldsymbol{\varphi}^*,\boldsymbol{\eta}\right) + DG\left(\boldsymbol{\varphi}^*,\boldsymbol{\eta}\right)\cdot\Delta\boldsymbol{u}\,. \tag{6.8}$$

In the finite element method, shape functions are used to describe the element shape and variation in displacements over the element domain. After FE discretization, the linearization on the element level yields a system of linear algebraic equations:

$$\sum_{i=1}^{N_{\text{nodes}}}\sum_{j=1}^{N_{\text{nodes}}}\left(\boldsymbol{K}^{M+G}\left(\boldsymbol{\varphi}^{*}\right)+\boldsymbol{K}^{I}\left(\boldsymbol{\varphi}^{*}\right)\right)_{ij}\cdot\Delta\boldsymbol{u}=\sum_{i=1}^{N_{\text{nodes}}}\left(F^{\text{ext}}\left(\boldsymbol{\varphi}^{*}\right)+F^{\text{int}}\left(\boldsymbol{\varphi}^{*}\right)\right)_{i} \tag{6.9}$$

The term in parentheses on the left-hand side of (9) is the tangent stiffness matrix, the vector $\Delta\boldsymbol{u}$ is the vector of unknown incremental nodal displacements, $\boldsymbol{F}_{\text{ext}}$ is the vector of external forces arising from the differences in the image intensities and gradients as per equation (6.6), and $\boldsymbol{F}_{\text{int}}$ is the vector of internal forces resulting from the stress divergence. The contribution of the strain energy density to the tangent stiffness (in terms of the FE nodal coordinate system) may be expressed as:

$$\boldsymbol{K}^{(M+G)}=\int_{\beta}\left(\boldsymbol{B}^{NL}\right)^{T}\boldsymbol{\sigma}\boldsymbol{B}^{NL}dv+\int_{\beta}\left(\boldsymbol{B}^{L}\right)^{T}\mathbf{c}\boldsymbol{B}^{L}dv\,, \tag{6.10}$$

where $\boldsymbol{B}^{L}$ and $\boldsymbol{B}^{NL}$ represent the FE linear and nonlinear strain-displacement matrices, and $\mathbf{c}$ is the spatial elasticity tensor [25]:

$$\mathsf{c}_{ijkl}=\frac{4}{J}F_{iI}F_{jJ}F_{kK}F_{lL}\frac{\partial^{2}W}{\partial C_{IJ}\partial C_{KL}}\,. \tag{6.11}$$

In computational solid mechanics, the two terms on the right-hand side of (10) are referred to as the *material and geometric stiffness matrices*, respectively [25]. The contribution of the image energy to the tangent stiffness is given as

$${}^{I}\boldsymbol{K}=-\int_{\beta}\boldsymbol{N}^{T}\mathbf{k}\boldsymbol{N}\frac{dv}{\mathrm{J}}\,, \tag{6.12}$$

where $\boldsymbol{N}$ is the matrix representation of the FE shape functions and $\mathbf{k}$ is the 2nd spatial variation of the image energy density :

$$\mathbf{k} := \frac{\partial^2 U}{\partial \boldsymbol{\varphi} \partial \boldsymbol{\varphi}} = \lambda \left[\left(\frac{\partial S}{\partial \boldsymbol{\varphi}} \right) \left(\frac{\partial S}{\partial \boldsymbol{\varphi}} \right) - (T - S) \left(\frac{\partial^2 S}{\partial \boldsymbol{\varphi} \partial \boldsymbol{\varphi}} \right) \right]. \tag{6.13}$$

as computed at each node in the discretized template model. The term ${}^{I}\boldsymbol{K}$ defined in (9) is referred to as the *image stiffness*. Together, the terms in (10) and (12) form the tangent stiffness matrix. The variance terms are readily available at each degree of freedom in the template model through the diagonal terms of the tangent stiffness matrix [25]. Equation (6.9) is solved for an initial estimate of the unknown incremental nodal displacements $\Delta \boldsymbol{u}$ and this solution is then iteratively improved using a Newton (or quasi-Newton) method [27].

The tangent stiffness matrix contains detailed information about how the nodal forces would vary in response to a small variation in the template model configuration. The inverse of the tangent stiffness matrix is an approximation to the covariance matrix, and defines the stability of the configuration to changes in applied loads (or changes in image data) [28].

The values of the tangent stiffness matrix (and the residual array) depend on the current configuration of the deforming template model, and thus vary throughout the nonlinear solution process. At the end of the solution process, the norm of the right-hand side of equation (6.9) is minimized. The values of the image stiffness and material and geometric stiffness matrices can then used to evaluate the variance of the template configuration with respect to the image data and the deformation potential.

Image Influence Measures

The present work examined four influence measures: image force multiplier, image data variance, template model variance, and a ratio of image data variance to total variance. The *image force multiplier* reflects the spatial distribution of the weighting given to the image force as shown by the Lagrange multipliers λ_i at each node (N). The *image data variance*, ${}^{I}\alpha_i$, shows the variance of the final template configuration with respect to the image data as obtained through the main diagonal entries of the image stiffness matrix.

$$ {}^{I}\alpha_i = \frac{\partial^2 U}{\partial \varphi_i \partial \varphi_i} \tag{6.14} $$

The *template model variance*, ${}^{MG}\alpha_i$, shows the variance of the final template configuration with respect to the template model parameters (i.e., material properties, boundary conditions) as obtained through the main diagonal entries of the material and geometric stiffness matrix.

$$ {}^{MG}\alpha_i = \frac{\partial^2 W}{\partial \varphi_i \partial \varphi_i} \tag{6.15} $$

The final measure is a ratio of the image data variance to the combined image data and template model variances and will be referred to in the present work as the *image influence*, ${}^{ratio}\alpha_i$.

$$ {}^{ratio}\alpha_i = \frac{{}^{I}\alpha_i}{{}^{MG}\alpha_i + {}^{I}\alpha_i} \tag{6.16} $$

Illustrative Examples

The illustrative examples selected for the present work were chosen for their ability to demonstrate typical characteristics of registration problems. The examples include both homogeneous and inhomogeneous template models, variations in image texture quantity and quality and different imaging modalities.

Gaussian Blur

A simple problem in deformable image registration involves registration of 2D Gaussian blurs (point spread functions) with distinct variance values. For the present work, a template image (256x256) was constructed using a Gaussian with unequal variances in the two principal directions (54x12). The target was similarly constructed with a distinct center point, but with a symmetric variance (32x32). The problem was selected to provide an intuitive example for exploring the various influence measures described above.

The entire template image domain was discretized using a rectilinear FE mesh. Arbitrary homogeneous hypoelastic material properties were selected to constrain the field of possible deformations. Deformation was limited to the plane of the image data and the edges of the image space were fixed.

Human Distal Phalanx

The second example examined deformable registration of sequential high-resolution MR images taken during indentation of the human fingerpad. The problem demonstrates the effect of an inhomogeneous template model on the described influence measures.

A 4.7 Tesla magnet and a RARE sequence were used to obtain high-resolution (125 x 125 μm) MR images of the cross-section of a healthy human male fingerpad [29]. The nail of the distal phalanx of the subject was rigidly constrained using a nonmagnetic frame. Mechanical indentation of 1-2 mm was applied to the fingerpad with a non-magnetic, rectangular indenter. Constant indentation was achieved by mounting the indenter to the constraint frame. The target image was acquired during a maintained indentation of the finger pad.

A FE mesh was constructed based on a manual segmentation of the undeformed template image. This mesh was divided into three regions based on tissue type. Hypoelastic material properties were assigned from the literature [30] as follows: bone ($E = 15\times10^8$ Pa, $\nu = 0.48$), dermis ($E = 15\times10^4$ Pa, $\nu = 0.48$), other tissue ($E = 15\times10^3$ Pa, $\nu = 0.48$). No externally applied loads or boundary conditions were imposed on the model; thus deformation of the mesh was exclusively due to the image registration process.

Human Spinal Disc

The final example problem examines registration of sequential images of the human spinal disc taken before and during compression. Similar to the distal phalanx problem, the template model was inhomogeneous, with the additional complication of using an orthotropic material to describe the complex character of the spinal disc.

Using a nonmagnetic compression frame and a MR scanner, MR images of a L2-L3 motion segment were obtained before (Template) and after (Target) application of a compressive load (image data supplied by Chiu et al. [31]). The Template image was manually segmented to obtain contours corresponding to the bone and disc.

These contours were used to generate a FE mesh corresponding to the specific anatomy of the subject. Image data were spatially filtered at the spatial Nyquist frequency of the FE mesh to avoid aliasing. Representative hypoelastic material properties were estimated from the literature [32]. Similar to the previous problems, no externally applied loads or boundary conditions were imposed on the model.

Results

Quantitative results from the Gaussian blur example problem are shown in Figure 6.1. The top row shows the standard reported image registration results, from left to right: template (T), target (S), initial difference image (T-S), registered template (T*), final difference image (T*-S). The homogenous template model spanning the entire template image domain is shown in panel F. The rest of the bottom row (panels G-J) shows the various influence measures for the computed registration. The image force multiplier results (panel G) indicate inconsistencies in the magnitude of the registration force generated by the image data. For this problem, the magnitude was largest in the areas of the template model that were not completely aligned with the target image (compare to panel E). For this homogenous problem, the magnitude of the template model variance (panel H) closely corresponds to template deformation field. The magnitude of the image data variance (panel I) is indicative of the correspondence between the template and target image data, with their corresponding gradients and Laplacians. For this particular problem, the image influence results mirror the image data variance due to the homogeneity of the underlying template model.

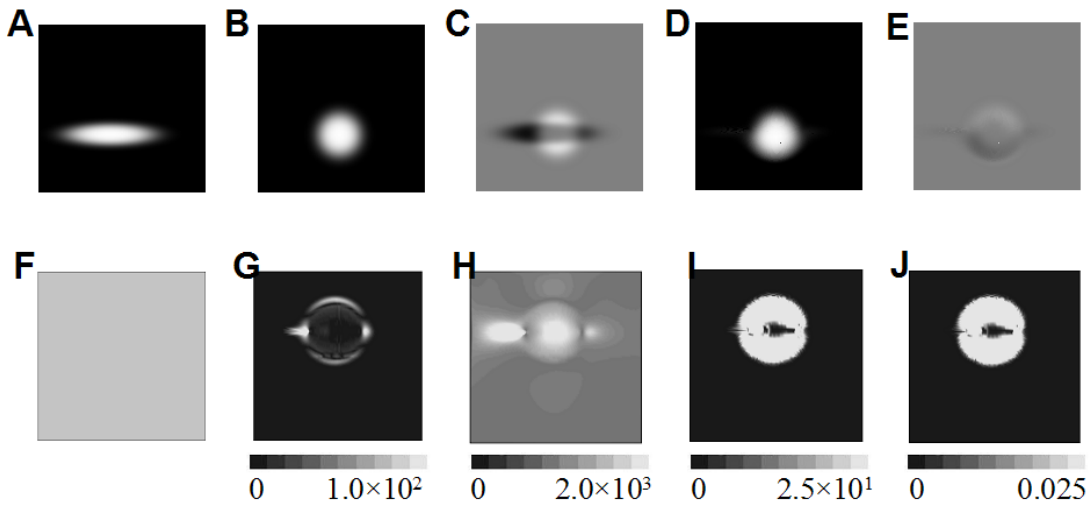

Figure 6.1. Influence measures for registration of a Gaussian blur. Panels A and B show the template (T) and target (S) images, respectively. Panel C shows initial subtraction results (T-S). Panel D shows the registered template image (T*). Panel E shows final subtraction results (T*-S). The homogeneous template model covering the entire span of the template image is shown in panel F. Different measures of image influence are demonstrated in panels G-J: image force multiplier, template model variance, image data variance, and image influence, respectively.

Results from the distal phalanx registration are shown in Figure 6.2. Consistent with all the figures, standard registration results are shown along the top row. The inhomogeneous template model is shown in panel F, with different grayscale values corresponding to the regions of defined material properties. Image force multiplier results in panel G emphasize inconsistencies in the registration force. In this particular case, the magnitude of the image force multiplier may represent an inability of the chosen material model to accurately represent the complex deformation in the pulp portion of the finger. The bright portions of the multiplier in the central portion of the model could also indicate that the elastic modulus selected for the bone was probably too low. The template model variance results in panel H directly

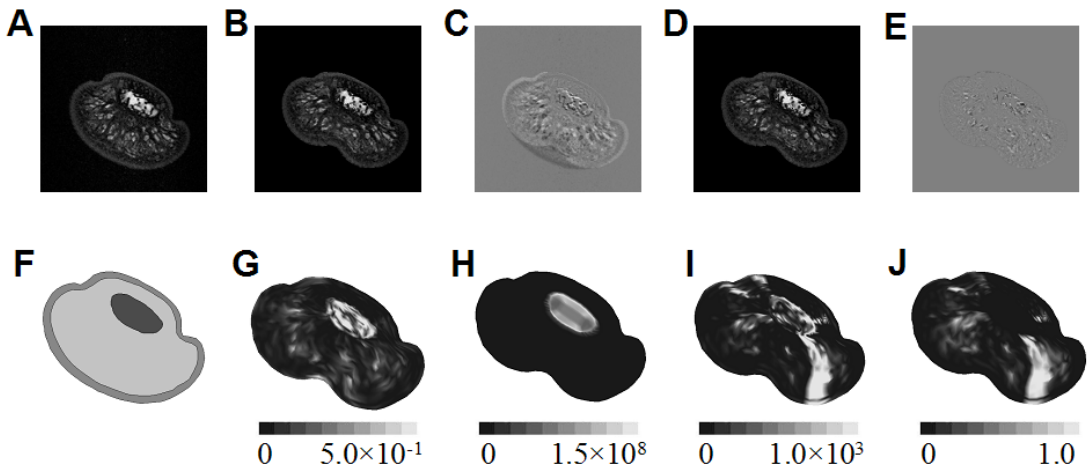

Figure 6.2. Influence measures for registration of the human distal phalanx. Panels A and B show the template (T) and target (S) images, respectively. Panel C shows initial subtraction results (T-S). Panel D shows the registered template image (T*). Panel E shows final subtraction results (T*-S). The homogeneous template model covering the entire span of the template image is shown in panel F. Different measures of image influence are demonstrated in panels G-J: image force multiplier, template model variance, image data variance, and image influence, respectively.

correspond to the relative stiffness of the different portions of the template model. The image data variance (panel I) is indicative of the correspondence in image intensity, gradient, and Laplacian between the registered template and target images. It is especially valuable to notice the brightest areas of the panel, since these areas have the highest correspondence. The image influence results in panel J reflect the image data variance results as scaled by the total variance to give insight into the relative importance of the image correspondence to the final registration result.

Figure 6.3 gives quantitative results from the spinal disc registration example. The standard registration results are again presented along the top row of the figure. The different grayscale values in panel F correspond to the regions of different material parameters. Image force multiplier results given in panel G show inconsistencies in registration force along the cortex areas of the spinal bones, an

indication that the material stiffness in these regions is significantly higher than was assigned to the template model. The template model variance results (panel H) correspond closely with the relative stiffness values assigned to the template model. Image data variance results in panel I indicate regions of the registered template model where differences in image intensity, gradient, and Laplacian values between the template and target images were smallest. Image influence results (panel J) demonstrate the image data surrounding the disc played the most significant role in the computed registration.

Discussion

In many image segmentation and intersubject registration problems (e.g., the Gaussian blur example), it is desirable to maximize the influence of the image data on the registration. For these types of problems, there is usually no known physical correspondence between the template and target images. The registration constraints, such as the material model parameters, serve only to regularize the problem. In this case, a high image influence with a relatively uniform value across the domain of the template model may be an indicator of good image alignment.

In strain tracking and tissue growth problems however, there are known physical relationships between the template and target material configurations. In general, less image texture is required to accurately compute stress and strain fields for problems with well-defined material characteristics. For example, the image influence results for the spinal disc registration in Figure 6.3J show that the image texture in the bone portions of the template model was largely superfluous. Registration was

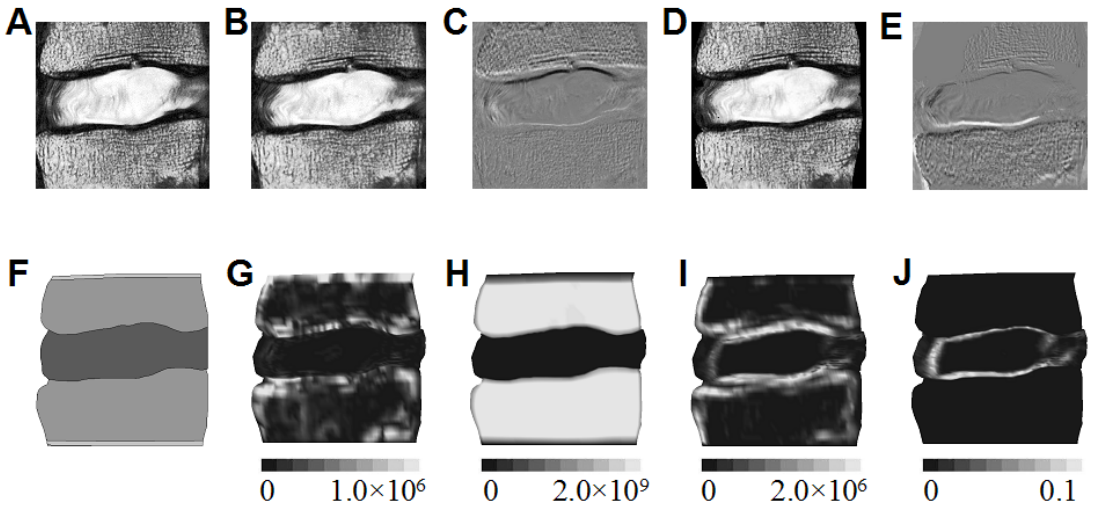

Figure 6.3. Influence measures for registration of the human spinal disc. Panels A and B show the template (T) and target (S) images, respectively. Panel C shows initial subtraction results (T-S). Panel D shows the registered template image (T*). Panel E shows final subtraction results (T*-S). The homogeneous template model covering the entire span of the template image is shown in panel F. Different measures of image influence are demonstrated in panels G-J: image force multiplier, template model variance, image data variance, and image influence, respectively.

controlled predominantly by the image data on the interior border of the disc, while the bone portions were pulled into position by the strength of the disc deformation. For problems such as these, the image influence can indicate which areas of the solution are most reliant upon the chosen registration parameters.

Another interesting observation from the two physically based registration examples (the distal phalanx and spinal disc), is that the image force multiplier λ, seems to be indicative of local variation from the chosen material parameter values. This could potentially allow future work in estimating unknown material parameters for problems with known boundary conditions.

It is valuable to discuss the importance of using the full tangent stiffness matrix (true Hessian) to calculate the image influence. It is common in many FE methods to

use an approximated, or incomplete version of the tangent stiffness matrix during the nonlinear solution process. Often a modified Newton, or quasi-Newton (i.e., DFP, BFGS), solution strategy will be used [27]. These solution strategies use approximate versions of the tangent stiffness matrix or the inverse tangent stiffness matrix. For example, many of the examples in the present work were solved using a BFGS solution strategy. BFGS updates have a much lower computational cost than full Newton stiffness reformations, and demonstrate a super-linear convergence rate. The approximate stiffness matrix does not, however, contain the same information about the relationship between the residual forces and the incremental nodal displacements. Prior to computation of the image influence field, it was necessary to reconstruct the true tangent stiffness matrix, with and without the image stiffness terms.

The previous paradigm in evaluating image registration algorithms has been focused upon determining *if* a method is able to achieve acceptable registration results. The growth in the maturity of image registration methods indicates that the time has come to change the paradigm. Most modern registration methods can achieve registration of most image problems. The paradigm shift is to understand which registration method is most appropriate for dealing with inadequacies in image data for particular registration problems. Understanding the nature of the transformations that are common to a particular class of registration problems, can naturally lead to an appropriate choice of method.

Acknowledgments

The MR images used for the fingerpad indentation analysis were provided by Mandayam Srinivasan, Kimberly Voss, and Josh Cysyk of the MIT Laboratory for

Human and Machine Haptics. We thank Dr. Bradley N. Maker for his continued collaboration on code development

References

1. J. Hadamard, "Sur les problemes aux derivees partielles et leur signification physique," *Bull. Univ. Princeton*, vol. 13, 1902.

2. J. Hadamard, "Le probleme de cauchy et les equations aux derivees lineaires hyperboliques," *Hermann, Paris*, 1932.

3. J.C. Gee and P.D. Peralta, "Continuum models for bayesian image matching," in *Maximum entropy and bayesian methods*, K.M. Hanson and R.N. Silver, Ed. Kluwer Academic Publishers: Dordrecht. 1996, p. 109-116.

4. J. West, J.M. Fitzpatrick, M.Y. Wang, B.M. Dawant, J. C. R. Maurer, R.M. Kessler, R.J. Maciunas, and et. al., "Comparison and evaluation of retrospective intermodality image registration techniques," *J. Comp. Assist. Tomography*, vol. 21, pp. 554-566, 1997.

5. P. Hellier, C. Barillot, I. Corouge, B. Gibaud, G.L. Goualher, L. Collins, A. Evans, G. Malandain, and N. Ayache. "Retrospective evaluation of inter-subject brain registration," in *Medical Image Computing and Computer Assisted Intervention,* Utrecht, The Netherlands: Springer-Verlag, 2001.

6. R. Bajcsy and S. Kovacic, "Multiresolution elastic matching," *Computer Vision Graphics and Image Processing*, vol. 46, pp. 1-21, 1989.

7. G.E. Christensen, R.D. Rabbitt, and M.I. Miller, "Deformable templates using large deformation kinematics," *IEEE Trans. Image Processing*, vol. 5, no. 10, pp. 1435-1447, 1996.

8. C.A. Glasbey and K.V. Mardia, "A review of image-warping methods," *J. Appl. Stat.*, vol. 25, no. 2, pp. 155-172, 1998.

9. A.K. Jain, Y. Zhong, and D.-J. M.P., "Deformable template models: A review," *Signal Processing*, vol. 71, no. 2, pp. 109-129, 1998.

10. M. Kass, A. Witkin, and D. Terzopoulus, "Snakes: Active contour models" *Int. J. Comp. Vision* vol. 1, pp. 321-331, 1988.

11. T. McInerney and D. Terzopoulos, "Deformable models in medical image analysis: A survey," *Med. Image Analysis*, vol. 1, no. 2, pp. 91-108, 1996.

12. M. Moshfeghi, "Elastic matching of multimodality medical images," *CVGIP: Graphical Models and Image Processing*, vol. 53, pp. 271-282, 1991.

13. R.D. Rabbitt, J.A. Weiss, G.E. Christensen, and M.I. Miller, "Mapping of hyperelastic deformable templates," *Proc. SPIE*, vol. 252, pp. 252-265, 1995.

14. A. Veress, J. Weiss, G. Gullberg, G. Vince, and R. Rabbitt, "Validation for the determination of strain and displacement fields in coronary arteries imaged by intravascular ultrasound," *Proc. ASME BED* in Snowbird, UT ASME, 2001.

15. J.A. Weiss, R.D. Rabbitt, and A.E. Bowden, "Incorporation of medical image data in finite element models to track strain in soft tissues," *SPIE Biomed. Optics Symp. BiOS98*, vol. 3254, pp. 477-484, 1998.

16. J. Gee, M. Reivich, and R. Bajcsy, "Elastically deforming 3d atlas to match anatomical brain images," *J. Comp. Assist. Tomography*, vol. 17, no. 2, pp. 225-236, 1993.

17. M. Moshfeghi, "Three-dimensional elastic matching of volumes," *IEEE Trans. Image Processing*, vol. 3, no. 128-138, 1994.

18. T. McInerney and D. Terzopoulos, "A finite element model for 3D shape reconstruction and nonrigid motion tracking," Proc. *IEEE,* vol. 2, pp. 518-533, 1993.

19. P.A. Freeborough and N.C. Fox, "Modeling brain deformations in alzheimer's disease by fluid registration of serial MR images," *J. Comp. Assist. Tomography*, vol. 22, pp. 838-843, 1998.

20. A.J.M. Spencer, *Continuum mechanics*, Essex England: Longman Scientific & Technical, 1980.

21. A.I. Veress, J.A. Weiss, R.J. Gillies, A.E. Bowden, J.-P. Galons, and R.D. Rabbitt, "Quantification of changes in mouse brain morphology using MRI and hyperelastic warping," *IEEE Trans. Medical Imaging*, to be published.

22. A.E. Bowden, R.D. Rabbitt, J.A. Weiss, and B.N. Maker, "Anatomical registration and segmentation by warping template finite element models," *Proc. SPIE*, vol. 3254, pp. 469-476, 1998.

23. J.E. Marsden and T.J.R. Hughes, *Mathematical Foundations of Elasticity*, Minneola, NY: Dover, 1994.

24. J.C. Simo, "A framework for finite strain elastoplasticity based on maximum dissipation and the multiplicative decomposition: Part I continuum

formulation," *Comp. Meth. Appl. Mech. Engineering*, vol. 66, pp. 199-219, 1988.

25. K.-J. Bathe, *Finite Element Procedures*, New Jersey: Prentice-Hall, 1996.

26. J.N. Reddy, *Energy and Variational Methods in Applied Mechanics*, New York: Wiley, 1984.

27. H. Matthies and G. Strang, "The solution of nonlinear finite element equations," *Int. J. Numer. Methods Eng.*, vol. 14, pp. 1613-1626, 1979.

28. R. Davidson and J.G. MacKinnon, *Estimation and Inference in Econometrics*, New York: Oxford University Press, 1993.

29. K.J. Voss and M.A. Srinivasan, " Investigation of the internal geometry and mechanics of the human fingertip, in vivo, using magnetic resonance imaging," Touch Lab Report, Cambridge, MA, MIT RLE TR-622, 1996.

30. R.J. Gulati and M.A. Srinivasan, "Determination of mechanical properties of the human fingerpad, in vivo, using a tactile stimulator," Touch Lab Report, Cambridge, MA, MIT RLE TR-605, 1996, p. 265.

31. E.J. Chiu, J.C. Lotz, and S. Majumdar, "High resolution magnetic resonance imaging of the human intervertebral disc with compression" *Trans. 41st Orthopaedic Res. Soc.* vol. 20(2) pp. 292, 1995.

32. Y.K. Liu, G. Ray, and C. Hirsch, "The resistance of the lumbar spine to direct shear " *Orthopadic Clin. North Am.* vol. 16(1) pp. 33-47, 1975.

CHAPTER 7

DISCUSSION

The research described in this dissertation has investigated deformable template based image registration methods in general, and Warping in specific. A series of regularization tools were developed which have application to practical image registration problems. These tools were incorporated into the continuum mechanics based deformable template registration method known as Warping. Warping was then used to solve a variety of typical registration problems, utilizing regularization tools when needed.

Two novel techniques were developed for examining and evaluating registration results. The singular value decomposition (SVD) was used to quantify the success of image registration through hierarchical evaluation of the topological correlation between the target and registered template images. The second technique used the Hessian of the registration potential energy to evaluate the relative influence of the image data versus registration constraints on deformable template based image registration solutions.

The purpose of this chapter is to briefly discuss the application, limitations, and future directions of the work described in this dissertation. The chapter is

organized to address these items with respect to each topic of research, followed by a few concluding remarks.

Regularization of Image Registration Problems

In contrast to simple registration methods such as landmark and principal axis, solution of image registration problems using deformable template methods is largely the purview of the specialist. These methods have enormous potential, and can achieve accurate registration results for a wide variety of difficult problems. Unfortunately, they are also susceptible to local minima, and registration must be monitored and evaluated by an expert in order to achieve complete registration.

The regularization tools presented in Chapter 3 of the present work provide a step towards the automation of deformable template methods. Different classes of registration problems present different types of difficulties during registration. For example, many of the strain tracking registration results presented in this work were obtained using a similar pattern of regularization: 1) match image histograms, 2) apply dynamic spatial filtering through the solution process, 3) evaluate solution results using Mapper3D and repeat, while adjusting the degree of spatial filtering and the value of the penalty parameter. Intersubject registration problems often required an additional rezoning step in the problem iteration process. As the difficulties associated with each class of registration problem become more thoroughly characterized, it will be possible to anticipate the types of regularization (and the appropriate parameters), needed in order to solve the problems automatically.

Automatic identification and solution of regularization difficulties is critical to the future of deformable template based image registration. The problem is largely

ignored in the literature, but is a matter of great practical concern. For example, it is not atypical for a registration problem to require ten or more iterations to achieve an acceptable registration solution. For small, 2D problems, this iteration process can be an annoyance. For large, 3D problems, this can mean days or weeks of solution time. Solution times reported in the literature are often deceptive, in that only the time required for the final iteration of the problem is reported, after the registration parameters have been optimized and any needed regularization tools have been applied. There is a need for future work in characterization and optimization of registration and regularization parameters.

Evaluation of Image Registration Results Using SVD

Global measures of accuracy have become the de facto standard for evaluating image registration results. They are easy to compute, and intuitive to understand. Although these measures are adept at showing differences in image data, they do little to help the researcher identify causes of misregistration, and ranking of solution results based on these measures can be inconsistent with expert evaluation.

The SVD topology tracking technique presented in Chapter 5 presents an alternative means of evaluating the accuracy of image registration results. The individual elements of the topology of the deformed template image are compared hierarchically with the corresponding elements of the target image topology. This approach can allow the researcher to identify the relative spatial frequency of elements of the topology that are out of correspondence. With this information, registration and regularization parameters can be adjusted to improve registration results.

The primary limitation of the technique is that it is difficult to establish that a particular registration solution is the best possible. Because the technique uses the registered template image, the accuracy in correspondence between the inner products of the registered template with the target singular values is limited by the effectiveness of the software used to apply the computed template deformation field to the image data (e.g., Mapper3D).

Current implementation of the technique is limited, in that it is used as a post-processing evaluation tool. It is anticipated that future work could incorporate the technique into the solution process, perhaps for use as a stopping criterion, or to allow automatic adjustment of regularization and registration parameters.

Determining the Relative Influence of Image Registration Constraints

There are a multitude of available image registration methods, each with different strengths and weaknesses. Each of these methods affects the computed solutions in a different manner. In Chapter 6, a novel technique for determining the relative contributions of image data and registration method to the registration solution was presented. The technique utilizes the terms of the registration potential energy in order to evaluate the relative importance of the terms to the registration solution. Using this information, it is possible to identify regions of the template model that were heavily influenced by the image data, as well as regions where the registration constraints dominated the solution.

Application of the technique may be limited by the particular registration method, because the Hessian is expensive computationally to calculate. For FE based techniques, this is not a concern, since the terms of the Hessian are used in the tangent

stiffness matrix. It is possible however, that other useful information in the stiffness matrix is being ignored by the technique, and that future modifications may utilize the individual terms of this matrix more completely.

Future extension of the technique may take advantage of the fact that the inverse of the Hessian is directly related to the covariance matrix. The covariance matrix contains information about the response of the deformed configuration to variation in the image data. This information could be used to estimate the mean error associated with the deformed template configuration.

In the future, the technique may play a role in characterizing unknown material parameters. The hypothesis would be that image data could be combined with known boundary conditions and an assumed material model to predict unknown material parameters. The general procedure would involve: 1) approximation of the unknown material parameters, 2) solution of a Warping image registration problem, with the known boundary conditions applied, 3) an iterative optimization procedure that strives to minimize the scalar stiffness ratio by adjusting the material parameters, while simultaneously examining the Lagrangian multipliers λ, associated with the image potential.

Concluding Remarks

I suppose that it is common for most graduating PhDs to pause and reflect on the nature and size of the task that has been completed. Reality harshly decrees that very few theses have ever made the best-seller lists, and most gather dust on forgotten shelves in university libraries. Occasionally, however, an enterprising reader stumbles upon something that can enlighten or inspire. At the end of this work, it is my

romantic notion that the work contained in this dissertation might be a stepping-stone for those who wish to utilize the tools and techniques that have proven valuable to me in deformable template based image analysis. It is to you that I address my concluding remarks. To paraphrase a statement that has become part of the vernacular (and was my credo during this journey known as graduate school):

… to boldly Warp what no one has Warped before